All-inorganic heterostructure light-emitting devices based on ZnO nanoparticles

Von der Fakultät für Ingenieurwissenschaften

Abteilung Elektrotechnik und Informationstechnik

der Universität Duisburg-Essen

zur Erlangung des akademischen Grades

Doktor der Ingenieurwissenschaften

genehmigte Dissertation

von

Patrick Felbier

aus

Dortmund

1. Gutachter: Prof. Dr. Gerd Bacher
2. Gutachter: Prof. Dr. Roland Schmechel

Tag der mündlichen Prüfung: 23.06.2015

Dedicated to my grandfather Werner, who laid the foundation for my technical education in preschool-age and ignited my intrinsic motivation to grow with his positive encouragement.

Acknowledgments

A lot of people have contributed to this work, and it is a pleasure for me to use this opportunity to thank them. Such a complex research project would never have been successful without their support. Everyone of them is very special and has been able to teach me something. I am really thankful for the time we have worked together!

First of all, I would like to express my deep gratitude to my advisor, Prof. **Gerd Bacher** for his guidance and for the productive discussions we had during my time at the WET. His support, especially in the final phase of writing this thesis, has been invaluable.

I thank Prof. **Roland Schmechel** for accepting the task of being my second examiner.

I acknowledge the Deutsche Forschungsgemeinschaft (DFG) and Evonik Industries for founding through supporting the Research Training Group GRK 1240 "Nanotronics". I thank Prof. **Markus Winterer** for the effort he has put into organizing the GRK. I would also like to express my gratitude to Evonik Industries for providing me with ZnO nanoparticles and Philips for supply of ITO substrates.

I thank Dr. **Tilmar Kümmell** for his advice, especially during the early phase of my research.

I acknowledge **Michael Schmitz** for his efforts to investigate and improve the WO_3/ZnO devices during research for his Bachelor thesis. I thank Dr. **Robert Köster**, who contributed his knowledge about growth of p-GaN and spent several days making the p-GaN templates, Dr. **Ingo Regolin** for providing me with the initial p-GaN templates, and **Dennis Albrecht** and **Tobias Litwin** for developing ohmic p-contacts to p-GaN. I would like to thank **Ekaterina Nannen** and **Svenja**

Wolff who shared their ideas about experimental techniques with me. I would also like to acknowledge **Adrian Münzer**, **Rene Albert**, **Jumen Rest**, **Florian May**, and **Krishan Lambach**, who contributed to this work during their student projects. I thank **Alexander Kompch** for XRD and XANES measurements and discussing them with me.

I greatly acknowledge Prof. **Uwe Kortshagen** for welcoming me at his group in Minnesota. He gave me the permission to change one of his setups completely and without his support, developing highly luminescent ZnO quantum dots from a nonthermal plasma would not have been possible. I acknowledge **Jens Theis** who shared my enthusiasm for developing a nonthermal plasma reactor capable of producing ZnO, **Jihua Yang** for his support on handling the experimental setups in Minnesota, and **Andrew Wagner** for taking HRTEM pictures. I thank **Rebecca Anthony** who answered all my questions about nonthermal plasma reactors and thereby enabled me to design the ZnO reactor, and **Richard Liptak** for his suggestions on reactor components.

I am grateful to **Helmut Lebeau**, who has spent his free time to make sample holders and **Horst Watzel** for his support in the clean room. I would like to thank **Franziska Muckel** (photoluminescence quantum yield measurements) and **Sven Eliasson** (atomic force microscopy) for their experimental support.

Contents

List of figures

List of tables

List of abbreviations and symbols

Abbreviations

ac	Alternating current
AFM	Atomic force microscopy
CCD	Charge-coupled device
dc	Direct current
DI	De-ionized
DRIFTS	Diffuse reflectance infrared fourier transform spectroscopy
EL	Electroluminescence
EML	Emitting layer
ETL	Electron transport layer
EPR	Electron paramagnetic resonance
EQE	External quantum efficiency
Gen	Generation
HOMO	Highest occupied molecular orbital
HTL	Hole transport layer
HRTEM	High-resolution transmission electron microscopy
IR	Infrared
LED	Light-emitting diode
LUMO	Lowest unoccupied molecular orbital
MOVPE	Metal-organic vapor phase epitaxy
NBE	Near band edge
NIST	National Institute of Standards and Technology
OLED	Organic light-emitting diode
PL	Photoluminescence
PLE	Photoluminescence excitation
PLQY	Photoluminescence quantum yield
rf	Radio frequency
rpm	Rounds per minute
TCO	Transparent conductive oxide
TEM	Transmission electron microscopy
UV	Ultraviolet
Vis	Visible
XANES	X-ray absorption near

	edge structure
XRD	X-ray diffraction

Materials

Al	Aluminum
Al_2O_3	Aluminum oxide
AlGaN	Aluminum gallium nitride
AlN	Aluminum nitride
Ar	Argon
Au	Gold
BN	Boron nitride
CdS	Cadmium sulfide
CdSe	Cadmium selenide
CH_4	Methane
C_2O_5OH	Ethanol
CH_3CHO	Acetaldehyde
Cp_2Mg	Bis(cyclopentadienyl) magnesium
Cu	Copper
$CuAlO_2$	Copper aluminum oxide
DEZ	Diethylzinc
FTO	Fluorine-doped tin oxide
GaAs	Gallium arsenide
$Ga(CH_3)_3$	Trimethylgallium
GaN	Gallium nitride
Ga_2O_3	Gallium oxide
Ge	Germanium
H	Hydrogen
H_2O_2	Hydrogen peroxide
HeCd	Helium/cadmium vapor
In	Indium
InP	Indium phosphide
ITO	Indium tin oxide
LiOH	Lithium hydroxide
Mg	Magnesium
MgO	Magnesium oxide
$Mg_{1-x}Zn_xO$	Magnesium zinc oxide
N	Nitrogen
NH_3	Ammonia
Ni	Nickel
NiO	Nickel oxide
NPB	N,N'-Di(1-naphthyl)-N,N'-diphenyl-(1,1'-biphenyl)-4,4'-diamine
O	Oxygen
PAMAM	Poly(amidoamine)
PTFE	Polytetrafluoroethylene
Si	Silicon
SiO_2	Silicon dioxide
$SrCu_2O_2$	Strontium copper oxide
TiB_2	Titanium diboride
TPM	3-(trimethoxysilyl)propyl methacrylate
W	Tungsten
WO_2	Tungsten dioxide
WO_3	Tungsten trioxide
Zn	Zinc

ZnO	Zinc oxide
ZnS	Zinc sulfide
ZnSe	Zinc selenide

Symbols

a	Slope
B	Bimolecular recombination coefficient
CB	Conduction band level
c	Velocity of light
d	Thickness
$\dot{d}$	Deposition rate
D_n	Electron diffusion constant
D_p	Hole diffusion constant
DA	Deep acceptor level
$\mathcal{E}$	Electrical field strength
E_{Gap}	Band gap
E_F	Fermi level
E_x	Kinetic energy component of the velocity perpendicular to the semiconductor interface
e	Electron charge
e^-_{CB}	Electron from the conduction band
F	Coefficient of finesse
G_n	Electron generation rate
G_p	Hole generation rate
h	Planck's constant
I	Device current
I_d	Dark current
I_{EL}	Electroluminescence intensity
I_{ph}	Photocurrent
J	Total current density
J_n	Electron current density
J_p	Hole current density
J_0	Saturation current density
j	Index of coordinate in x-direction
$j_{dif,n}$	Electron diffusion current density
$j_{dif,p}$	Hole diffusion current density
$j_{dr,n}$	Electron drift current density
$j_{dr,p}$	Hole drift current density
k	Boltzmann constant
L	Barrier width
l	Index of coordinate in y-direction
M	Number of coordinates measured in x-direction
m_e	Electron mass
m_e^*	Effective electron mass
m_h^*	Effective hole mass
$\dot{m}$	Mass flow

N	Number of coordinates measured in y-direction
N_A	Acceptor concentration
N_D	Donor concentration
n	Free electron density
n_c	Number of charge carriers
n_i	Intrinsic carrier concentration
n_{ph}	Number of photons
n_0	Free electron density in equilibrium
$\tilde{n}$	Refractive index
O_i	Oxygen interstitial
P	Intensity
P_f	Forward power
P_r	Reflected power
p	Free hole density
p_O	Partial pressure of oxygen
p_w	Working pressure
p_0	Free hole density in equilibrium
q	Electrical charge
QY	Quantum yield
R_F	Fresnel reflection coefficient
R_{Total}	Total reflection coefficient
S_a	Surface roughness
T	Temperature
T_{opt}	Optical transmission
$\tilde{T}$	Charge carrier transmission coefficient
t	Time
t_{pre}	Pre-sputtering duration
U	Recombination rate
U_n	Electron recombination rate
U_p	Hole recombination rate
V	Voltage
V_O^x	Neutral oxygen vacancy
$V_O^\bullet$	Singly-ionized oxygen vacancy
$V_O^{\bullet\bullet}$	Doubly ionized oxygen vacancy
v_{dr}	Charge carrier drift velocity
$v_{dr,n}$	Electron drift velocity
$v_{dr,h}$	Hole drift velocity
VB	Valence band level
x, y, z	Cartesian coordinates
Zn_s	Zinc atom at the surface
Φ	Work function
Ψ	Built-in potential
α	Share of detected photons per emitted photons
χ	Electron affinity
δ	Phase difference
$\epsilon_r(0)$	Static relative permittivity
ϕ_B	Barrier height
γ_{EL}	Spectral sensitivity
η	Ideality factor
η_{ext}	External quantum efficiency

η_{inj}	Injection efficiency	λ	Wavelength
η_{int}	Internal quantum efficiency	μ_n	Electron mobility
		μ_p	Hole mobility
η_{out}	Out-coupling efficiency	π	Pi
η_{QY}	Quantum yield of the active material	θ	Angle

1. Introduction

LEDs (light-emitting diodes) have started a revolution in lighting. They are found in almost all every day lighting applications, from ambient room lighting and street illumination,[1] display back lighting,[2] signal lamps,[3] to automotive head and rear lamps,[3] e.g., just to name some of the most important ones. UV emitting LEDs are used for example for disinfection of arbitrary fluids and gases,[4] or for hardening of industry resins.[5] Advantages over traditional light sources include long-term stability,[6] high efficiency and low heat emission,[7] while both, narrow emission spectra,[8] and white light are achievable.[1] A newer LED type, OLEDs (organic light-emitting diodes), added wide-area emission, flexible substrates,[2, 9] and low-cost production to the possibilities of LED design.[10] While LEDs incorporating organic layers face certain issues with long-term stability,[6, 11] some progress has been made in improving this typical weakness of OLEDs.[12, 13]

A good compromise between the strengths and weaknesses of epitaxial and organic concepts can be made by all inorganic nanoparticle emitters. While inorganic materials provide the potential for the devices to be robust,[14] the replacement of rigid layers with nanoparticle ones provides a perspective for cost effective production methods like ink-jet printing and for realizing LEDs based on flexible substrates, e.g. for flexible displays.[15] Another important advantage of nanoparticles is the fact that they are produced separately from the device, which provides two advantages. First, independent production allows dedicated pre- and post-growth treatments like annealing, and second, nanoparticles of different color can be produced in mass production and then be printed on demand increasing the cost advantage. Like for OLEDs, wide-area emission is regularly reported.[14, 16, 17] The most efficient nanoparticle emitters so far have been chalcogenides based devices using organic support layers.[18] Nevertheless, the long-term stability of these devices is still limited by the organic layers. In the quest for omitting this challenge, promising, all-inorganic concepts have been presented that replaced organic injection layers by transition metal

oxide ones.[14, 19] Unfortunately, these still include Cd which is carcinogenic.[20]

ZnO is a less toxic material that has attracted a lot of attention in the last decade due to the materials superior optical properties. It exhibits a direct band gap at room temperature with large exciton binding energy of 60 meV.[21] ZnO shows band gap related emission in the near UV spectral range, and the material provides the possibility of light emission in the visible spectral range originating from defect and surface states, as well.[22–24] Because reliable p-doping of ZnO, which is needed for application in homojunction LEDs, still remains challenging, different hole injection layers have been investigated, among them AlGaN,[25] $CuAlO_2$,[26] GaN,[27–85] NiO,[86–90] Si,[91–93] and $SrCu_2O_2$.[94]

A sufficient measure to judge how well a device concept works is the external quantum efficiency, which is determined by the luminescent quantum yield of the active material, the charge injection efficiency of the support layers and the out-coupling efficiency of the device.[1] While out-coupling can be optimized by transferring concepts from other LED types,[95] attaining a sufficient injection efficiency is a material specific challenge. Therefore, it has to be optimized along the quantum yield for every active material individually. Most often, no absolute values are reported for the EQE of ZnO devices, making it very difficult to evaluate the feasibility of the presented concepts and to compare one to the other. One exception is the report from Yang et al., who presented blue and green luminescence from a single ZnO nanowire demonstrating an EQE of 7.8 %,[96] but this emission neither has been wide-area nor has been purely from ZnO. A novel concept of a wide-area, white WO_3/ZnO nanoparticle LED has been reported with a maximum EQE of 2×10^{-6}.[97]

The main reason behind the difficulty to attain efficient large area emission from devices with ZnO as active material is the very low valence band level of ZnO, which makes it difficult to inject holes into the material. This characteristic is so strong that it has been commonly utilized for application of ZnO as dedicated hole blocking layer in solar cells.[98–100] The choice of hole conducting materials with sufficiently low work function is very limited.[101] Therefore, until now no ideal complementing material has been identified and some compromises will have to be made when choosing a suitable hole injection layer. The goal of this work is to provide a comprehensive study on hole injection layers in order to identify which properties of the hole injection materials are more important and which are less. Therefore, a set of three very different support layer materials will be studied.

The other important factor determining the EQE of an LED is the quantum yield of the active material. Traditionally, high efficiency nanoparticles have been made from chemical sol-gel methods. In 2010, Tang and coworkers reported ZnO quantum dots with a quantum efficiency of 26 %.[24] Two years later, Matsuyama et al. were able to increase this value to 61 % by LiOH-mediated growth and post growth surface capping.[23] They also were able to tune the emission color from yellow to blue by increasing the LiOH concentration. A very high efficiency of 76 % has been reported for blue emission of ZnO quantum dots by applying surface complexes to the nanoparticles using oleic acid,[102] but this has been unstable as the quantum yield decreases over the course of a few days. While these results show the great potential of ZnO nanoparticles for efficient emission, the sol-gel method has two important disadvantages for producing particles for LED applications. First, as the particles are made in solvents, ligands are used which are insulating. Second, the production volume of sol-gel processes is rather low, limiting its feasibility for industrial mass production. Both challenges might be solved by ligand-free synthesis from the gas phase, which obviates the need for ligand removal or replacement schemes typically required to achieve good electronic transport in nanocrystal films. Different gas phase routes for easily up-scalable production of ZnO nanoparticles have been reported: flame pyrolysis,[103, 104] hot-wall reactors,[105, 106] microwave plasmas[104] or a combination of the latter two.[106] However, so far there has been no report of ZnO nanoparticles from the gas phase which have been optimized for lighting applications, and no determination of the quantum yield resulting from the presented techniques has been made. Therefore, the second goal of this work will be to develop a method for industrial scalable, ligand-free, and highly luminescent ZnO nanoparticle production from the gas phase and investigating the luminescence mechanism leading to their efficient emission. The purpose of this is to enable further increases of the EQE of ZnO nanoparticle LEDs by an improved quantum yield of the active material, aside from optimized charge carrier injection. The proceeding of this thesis will be as follows:

Chapter 2 will provide the necessary background for understanding the operating principles of the LED. Current transport across semiconductor layers will be discussed followed by the mechanisms for luminescence of unipolar and bi-polar heterojunction devices. A detailed introduction of the external quantum efficiency will be given including important factors influencing its three components quantum yield, injection

efficiency and out-coupling efficiency.

In **chapter 3**, information on basic electrical and optical properties of ZnO will be given. Important information on the materials characteristics for application in LEDs will be presented, such as current transport in a ZnO nanoparticle layer or light-emitting transitions in ZnO, including band gap and defect related luminescence.

Chapter 4 presents the experimental methods used, beginning with a description of the production of transition metal oxide layers by radio-frequency sputtering, growth of epitaxial GaN by MOVPE (metal-organic vapor phase epitaxy) and the processing of the nanoparticle LEDs.

Chapter 5 will provide photoluminescence spectra of the ZnO nanoparticles used to make the LEDs presented within this thesis. After that, a simple ZnO nanoparticle LED without additional support layers will be investigated.

Chapter 6 will present n-WO_3/ZnO LEDs using a novel concept transferred from OLED technology which is based on electron extraction: The very low work function of n-conducting WO_3 allows tunneling of electrons out of deep levels, thereby creating holes which then recombine radiatively.

Chapter 7 will discuss a more traditional concept with hole injection by p-conductive NiO. The very low work function of NiO provides an electron barrier preventing leaking currents.

Chapter 8 will capture a concept using GaN with an almost perfect fit of valence band levels with ZnO.

Chapter 9 presents a newly designed nonthermal plasma reactor operated with a high frequency source that produces highly luminescent ZnO quantum dots.Further optical investigation allows a detailed analysis of the mechanism for the dominating green–yellow emission with a special focus on the role of oxygen species in the recombination process.

Finally, the results will be summarized in **chapter 10**, LED concepts will be compared and conclusions will be drawn.

2. Fundamentals of light-emitting devices based on nanoparticles

2.1. Charge transport in semiconductors

Following reference [107], an overview on the charge carrier transport in semiconductors shall be given in this section. From conservation of charge, the continuity relations can be deducted:

$$\frac{\partial n}{\partial t} = G_n - U_n + \frac{1}{q}\nabla \vec{J}_n, \tag{2.1}$$

$$\frac{\partial p}{\partial t} = G_p - U_p - \frac{1}{q}\nabla \vec{J}_p, \tag{2.2}$$

where n and p are the free electron and free hole densities, t refers to time, G_n and G_p are the electron and hole generation rates, U_n and U_p are the electron and hole recombination rates, q is the electrical charge, and $\vec{J}_n$ and $\vec{J}_p$ are the electron and hole current densities, respectively. If carrier generation is negligible, it can be concluded from these equations that electron-hole pairs that recombine radiatively in a LED have to be injected by a current. A current in bulk semiconductors can be described by two mechanisms: carrier drift and carrier diffusion.

The carrier drift is caused by an electric field. In case of a weak electric field, the charge carrier drift velocity v_{dr}, which is the absolute value of the average velocity vector of the continuum of charge carriers, is observed to be proportional to the electric field strength $\mathcal{E}$:

$$\vec{v}_{dr,n} = \mu_n \vec{\mathcal{E}}, \tag{2.3}$$

$$\vec{v}_{dr,p} = \mu_p \vec{\mathcal{E}}, \tag{2.4}$$

with the constant of proportionality μ called mobility. The current density can be obtained by taking the free charge carrier densities n and p, and their respective charges q into account:

$$\vec{j}_{dr,n} = qn\vec{v}_{dr,n} = qn\mu_n\vec{\mathcal{E}}, \tag{2.5}$$
$$\vec{j}_{dr,p} = qp\vec{v}_{dr,p} = qp\mu_p\vec{\mathcal{E}}, \tag{2.6}$$

The other component of the current in a semiconductor, the diffusion current $\vec{j}_{dif}$, is related to a gradient of charge carrier concentration

$$\vec{j}_{dif,n} = qD_n\nabla n, \tag{2.7}$$
$$\vec{j}_{dif,p} = -qD_p\nabla p, \tag{2.8}$$

where D is the diffusion constant for the respective charge carrier in the semiconductor. The current densities for each type of carrier are given by the sum of drift and diffusion currents

$$\vec{J}_n = \vec{j}_{dr,n} + \vec{j}_{dif,n} = qn\mu_n\vec{\mathcal{E}} + qD_n\nabla n, \tag{2.9}$$
$$\vec{J}_p = \vec{j}_{dr,p} + \vec{j}_{dif,p} = qp\mu_p\vec{\mathcal{E}} - qD_p\nabla p. \tag{2.10}$$

The total current density $\vec{J}$ can be calculated by summing up the current densities of electrons and holes:

$$\vec{J} = \vec{J}_n + \vec{J}_p, \tag{2.11}$$
$$= qn\mu_n\vec{\mathcal{E}} + qp\mu_p\vec{\mathcal{E}} + qD_n\nabla n - qD_p\nabla p. \tag{2.12}$$

2.2. Semiconductor heterojunctions

A semiconductor heterojunction consists of two different semiconductor materials of the same or a different type of doping (i-, n- or p-type), as opposed to a homojunction, where the material does not change. Because every LED presented here will be made of a heterojunction, it is important to get familiar with their characteristics.

2.2.1. Built-in potential, barrier height and band bending

An example of such a heterojunction is presented in Fig. 2.1. It consists of p-Si and n-Ge, which are very common semiconductors and have a large offset of their valence band levels. Fig. 2.1a shows the vacuum band level diagram after the Anderson Model,[108] which arranges the conduction band, valence band and Fermi level of both semiconductors by the quantities electron affinity χ, band gap E_{Gap} and work function Φ. Fig. 2.1b shows a simulation of the band diagram with the materials being in contact with each other. Usually, there is an offset between the Fermi levels of two different materials. If brought into contact, electrons will move from the material with higher Fermi level to the one with lower Fermi level and holes will move in the opposite direction, until the Fermi level offset is reduced to zero. The charge transfer leads to establishing a so called built-in potential Ψ. The built-in potential is visualized by an offset in the vacuum level of both materials, equal to the difference of their work functions:

$$\Psi = \Phi_2 - \Phi_1. \tag{2.13}$$

The conduction band levels CB are then given by simply subtracting the specific materials electron affinity from the vacuum level. The valence band levels VB can be calculated by subtracting the band gap energy from the conduction band levels. Band discontinuities result at the interface from the change of the crystal background field between the two materials, which is very abrupt if compared to the built-in potential caused by a usual charge-distribution. The discontinuity heights ΔCB and ΔVB can be predicted very well by the Anderson Model, unless band gap or electron affinity are a function of doping concentration:

$$\Delta CB = \chi_1 - \chi_2, \tag{2.14}$$

$$\Delta VB = \chi_1 - E_{Gap,1} - \chi_2 + E_{Gap,2}. \tag{2.15}$$

If an external bias is applied in forward direction, the built-in potential is decreased. Fig. 2.1c shows the calculated current-voltage-characteristic. More details about the current across a heterojunction will be given in section 2.2.2. Fig. 2.1d shows the band diagram of the junction in this case. The reduction of the built-in potential leads to a flattening of the bands. Simultaneously, a separation of quasi Fermi levels

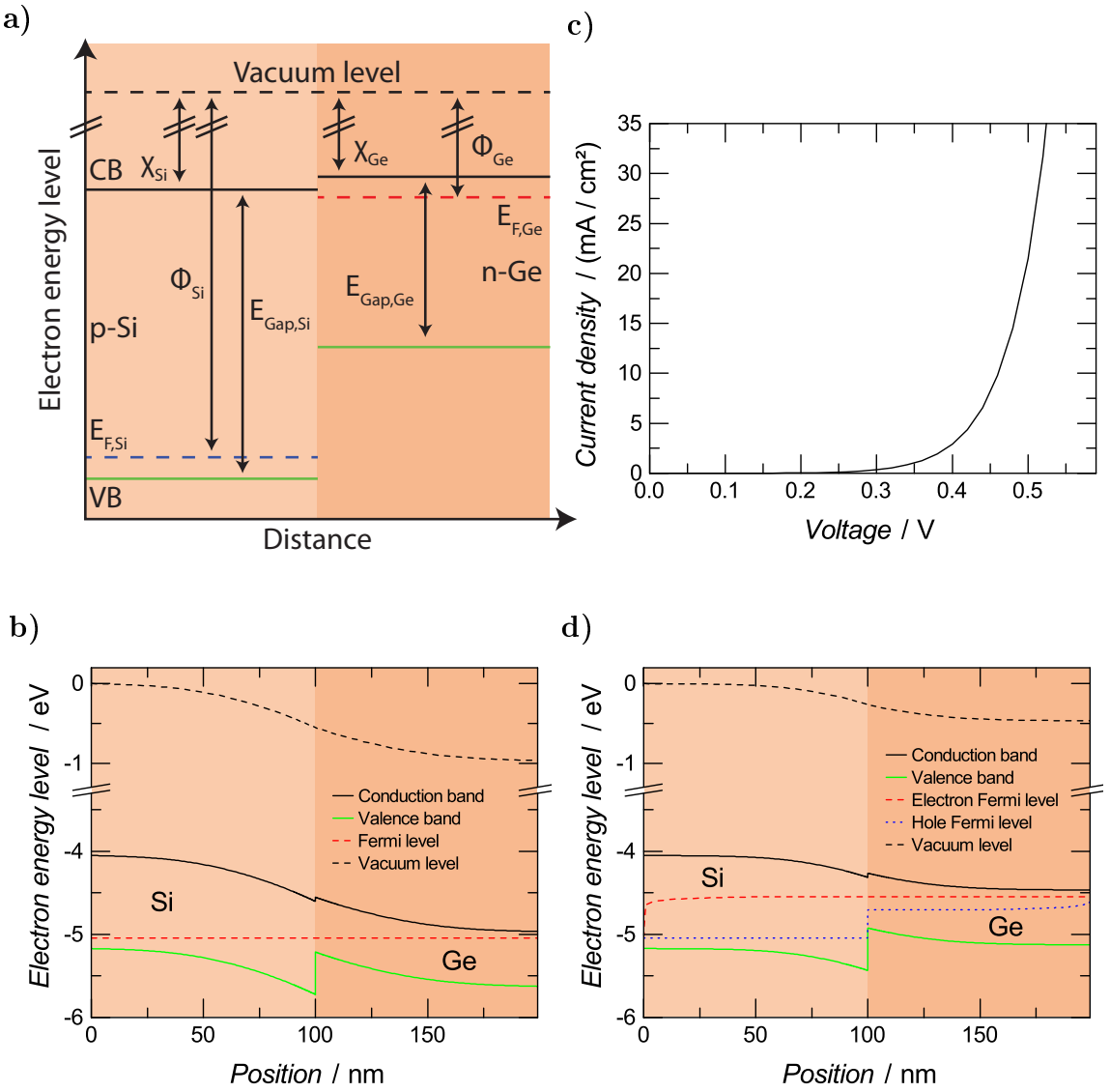

Figure 2.1. – Example heterojunction consisting of p-Si and n-Ge. (a) Vacuum level band diagram of the isolated semiconductors after Anderson.[108] E_{Gap}: band gap, E_F: Fermi level, χ: electron affinity, Φ: work function. (b) Simulation of conduction band level, valence band level, and Fermi level without external bias, (c) current-voltage-characteristic, and (d) band levels, quasi electron and quasi hole Fermi levels at external bias of 0.5 V and current density of 21 mA/cm^2. Si layer has been filled with light orange, Ge layer with orange in both figures allowing for quick comparison. Simulation has been done using SimWindows. For more details regarding the simulation cf. Appendix A.2.

is observed, because charge carrier concentrations above their equilibrium values are built up by injection.

The shape of the band bending is determined by the charge distribution of the diffused charge carriers. In a usual pn-junction, where the Fermi level of the p-type semiconductor is below the Fermi level of the n-type semiconductor, a charge carrier depletion region is created. The free charge carrier densities at the interface are reduced by out-diffusing of free charge carriers into the opposite layer. In case of a nn- (pp-) isotype heterojunction, only the interface region of the semiconductor with the higher (lower) Fermi level will get depleted by out-diffusion, while an accumulation layer is created by in-diffusion at the other side of the interface.[109] An example of an isotype nn-heterojunction is shown in Fig. 6.2.

2.2.2. Current transport across semiconductor heterojunctions

While the drift-diffusion charge carrier transport (Eq. 2.12) is the dominant one in bulk semiconductors, homojunctions and smoothly graded heterojunctions, two fundamental mechanisms exist that describe charge carrier transport across steep barriers at abrupt heterojunction interfaces: thermionic emission and tunneling.[107, 110–112] The Bethe criterion has been proposed to decide whether a barrier is regarded steep in this purpose.[112] It is fulfilled, if the barrier potential increases by much more than kT over the mean free carrier path, with k being the Boltzmann constant and T the temperature.

A charge carrier moving over a potential barrier by thermionic emission can be regarded in a classic way: The charge carrier has acquired an energy which is equal or higher than the barrier to overcome, and the transmission coefficient of thermionic emission becomes

$$\tilde{T_{th}} = \begin{cases} 0 & \text{for } E_x < q\phi_B, \\ 1 & \text{for } E_x \geq q\phi_B, \end{cases} \qquad [107] \tag{2.16}$$

with E_x being the kinetic energy of the velocity component perpendicular to the interface, q the carrier charge, and ϕ_B the interface barrier height. Because the thermionic model describes the case when $q\phi_B \gg kT$, only a small amount of charge carriers with high energy at the far upper end of the distribution is transmitted by

spending a share of their energy equal to the height of the potential step. The amount of transmitted charge carriers might be increased, e.g., by applying an external voltage and accelerating charge carriers. Arbitrarily large barriers, however, cannot be compensated unlimitedly without increasing the temperature of the device above its tolerance range, because the scattering cross section for inelastic processes increases rapidly, and the whole lattice heats up. Simultaneously, a saturation of charge carrier kinetic energy is observed.[113]

Tunneling is a quantum mechanical effect that allows charge carriers to leak through a finite zone with a potential higher than the carriers total energy. It becomes dominant over thermionic emission at very high barriers.[107] The charge carrier transmission coefficient of tunneling at abrupt barriers can be estimated by the WKB approximation (Eq. 2.17)

$$\tilde{T}_{tun}(E_x) = \exp\left(-\frac{2\pi}{h}\int_0^L \sqrt{2m_e^*(\phi_B(x) - E_x)}dx\right), [110] \tag{2.17}$$

with h being Planck's constant and L the width of the barrier. Current density-voltage characteristics of heterojunctions cannot be described by an analytical relationship that is generally valid, and have been calculated throughout this publication by a numerical method described in [110] (cf. Appendix A.2).

Nevertheless, an analytical solution for the special cases of a smoothly graded pn-heterojunction and an abrupt nn-heterojunction shall be discussed here. The current-voltage characteristic of a smoothly graded pn-heterojunction has been described analytically under the following assumptions[107]:

- The junction is considered to be smoothly graded according to the Bethe criterion.
- The built-in potential and the applied voltage are supported by a dipole layer with abrupt boundaries. Outside these boundaries, the semiconductors are assumed to be neutral.
- The Boltzmann statistic is valid.
- The minority carrier density is much smaller than the majority carrier density in each semiconductor.

- No charge carrier recombination takes place inside the depletion region, and the current is constant throughout the depletion region.

Similar to homojunctions, the current-voltage relationship of pn-heterojunctions can then be described by the Shockley equation,

$$J = J_0 \left[\exp\left(\frac{qV}{kT}\right) \right], \tag{2.18}$$

with T being the temperature, V the voltage drop across the junction, and J_0 the generalized saturation current

$$J_0 = \frac{qD_{n2}n_{i2}^2}{L_{n2}N_{A2}} + \frac{qD_{p1}n_{i1}^2}{L_{p1}N_{D1}}, \tag{2.19}$$

where D_n and D_p are the electron and the hole diffusion constants, L_n and L_p are the electron and hole diffusion lengths, N_A and N_D are the acceptor and donor concentrations, and n_i is the intrinsic carrier concentration. Here, the index 1 denotes a property of the n-semiconductor and the index 2 a property of the p-semiconductor. Under these conditions, the injection ratio depends linearly on the doping ratio and exponentially on the band gap difference:

$$\frac{J_n}{J_p} \propto \frac{N_{D1}}{N_{A2}} \exp\left(\frac{E_{Gap1} - E_{Gap2}}{kT}\right). \tag{2.20}$$

For abrupt nn-heterojunctions and under the assumption of a junction current that is completely thermionic emission related, the analytic current density-voltage relation (Eq. 2.21)

$$J = \frac{q^2 N_{D2}\phi_B}{\sqrt{2\pi m_2^* kT}} \exp\left(-\frac{q\phi_B}{kT}\right)\left(1 - \frac{V}{\phi_B}\right)\left[\exp\left(-\frac{qV}{kT}\right) - 1\right], [107] \tag{2.21}$$

$$\phi_B \approx \Psi(0V) = \Delta CB = \chi_1 - \chi_2, \tag{2.22}$$

has been derived, where N_{D2} and m_2^* are the donor concentration and effective electron mass of the n-semiconductor that the electrons are injected into. Note that the current in reverse direction never saturates, but increases linearly with voltage at $V \ll 0$.[107] In forward direction, Eq. 2.21 can be approximated by the exponential

relationship

$$J \propto \exp\left(\frac{qV}{\eta kT}\right), [107] \tag{2.23}$$

with ideality factor η. The dependence of J on the barrier height ϕ_B for a given voltage is much more complex, even in the special case discussed here where an analytical relationship could be evaluated.

2.3. Mechanisms for light generation

2.3.1. pn-junction

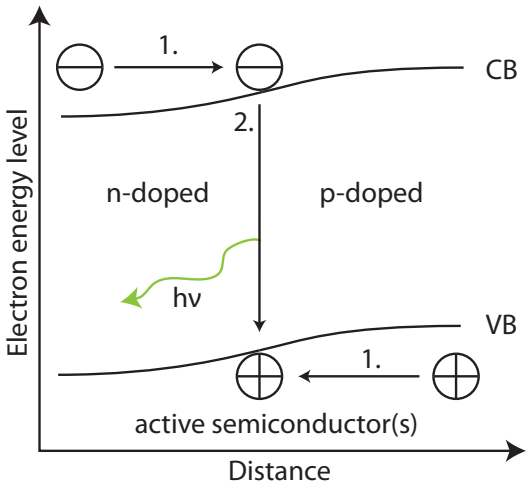

Figure 2.2. – Mechanism of electron-hole-pair generation in a bipolar device.[107]

The widely known radiative recombination mechanism describing the working principle of LEDs in the narrower sense is depicted in Fig. 2.2. The simplest form of these devices is based on a pn-junction. Experimental results show that the current density through a smoothly graded pn-junction with charge carrier recombination is increased exponentially with increasing voltage applied in forward direction according to Eq. 2.23, as well. Typically, η varies continuously between 1 when the diffusion current dominates and 2 when the recombination current dominates.[107] For some material systems, however, anomalous high ideality factors have been ob-

served, e.g. GaN.[114] Electrons are injected from the n-doped layer into the p-doped layer. Within the p-doped layer, these electrons are minority carriers among holes as the majority carriers. In case of holes, which are injected into the opposite direction, the inverse is true. Thereby, the electron/hole concentrations n/p are increased above the equilibrium concentrations n_0/p_0, respectively,

$$n = n_0 + \Delta n, \tag{2.24}$$

$$p = p_0 + \Delta p, \tag{2.25}$$

$$n_0 p_0 = n_i^2, \tag{2.26}$$

with n_i being the intrinsic carrier concentration.[107, 115] Consecutively, the minority carriers recombine radiatively with the majority ones in the respective area, emitting a photon. The recombination rate is proportional to both, n and p, and can be written using a proportionality constant B:

$$R = Bnp.[115] \tag{2.27}$$

Eq. 2.27 is called bimolecular rate equation, with B being named bimolecular recombination coefficient. Typical values of B are between $10^{-11}\,\mathrm{cm}^3/\mathrm{s}$ and $10^{-9}\,\mathrm{cm}^3/\mathrm{s}$ for III-V semiconductors and ZnO.[115, 116] Among commonly used material systems for making a LED based on a pn junction are, e.g., GaAs, GaN, and their ternary alloys with In or Al.[115] With regard to performance, such devices have been shown to exhibit superior properties: in case of GaN, LEDs have been developed that exceed a quantum efficiency of 70 %.[117] Possible emission wavelengths span from the UV, over the visible, and into the infrared spectral range.[115]

2.3.2. Unipolar nanoparticle semiconductor structures

Aside from pn-junctions, electron-hole pairs can also be created in unipolar device structures by exciting an electron, which leaves behind a hole in the valence band. They might recombine with each other or with another electron/hole being created at the same or another excitation event. Two mechanisms to excite an exciton in unipolar semiconductor structures are impact[118–124] and field-driven ionization[16, 17, 125–129]. For both types of ionization, the voltage drop per length is a crucial

number determining their possibility. Both ionization processes are shown schematically in Fig. 2.3 and will be discussed in more detail in the following paragraphs.

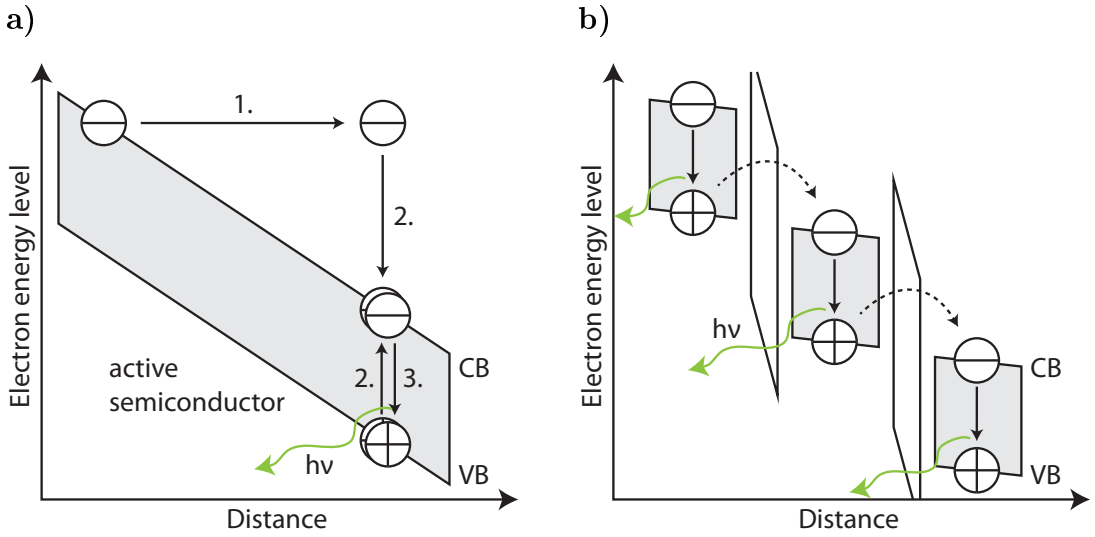

Figure 2.3. – Mechanism of electron-hole pair generation in a unipolar device. (a) Excitation by impact ionization. (b) Excitation by field-ionization: In this example, an extract of a multilayer structure with three identical layers of the same semiconductor is shown that are separated by insulating surface layers, where the major voltage drops occur. This results in a large offset between neighboring layers, so that electron from the previous layers valence band may tunnel into the conduction band of the next layer.[16]

Impact ionization

The process of impact ionization is shown in Fig. 2.3a. It is initiated by a charge carrier being accelerated by an electric field to kinetic energies above the band gap energy and far out of thermal equilibrium. Therefore, the mean free wavelength has to be long enough to allow the charge carrier to reach this very high velocity, because every early scattering event will make the charge carrier lose the majority of its attained energy. But if the kinetic energy of the charge carrier exceeds the band gap energy upon collision with an electron in the valence band, this electron might be excited to the conduction band while a hole is left behind. But as usually many other excitation processes are possible including the creation of phonons (heat), devices based on impact ionization are much less efficient compared to LEDs based

on direct injection.

Several ZnO light-emitting devices have been presented that rely on this mechanism,[118, 120, 122] supposedly because of the difficulties for direct injection. However, while there have been single reports on LEDs based on CdS[123] and ZnS[124] nanoparticles showing impact ionization, it has not been observed in a ZnO nanoparticle device. This is supposedly due to reports on ZnO nanoparticle LEDs being scarce in general and because the situation for this mechanism is unfavorable in a nanoparticle layer. As the mean free path is strongly restricted by interparticle boundaries in nanoparticle structures, the efficiency might even be further reduced compared to bulk devices, depending on the voltage drop per length and the nanoparticles size.

Field-driven ionization

While the field-driven ionization process is also possible across a single interface, it will be described here for a multiple-interface structure which is the usual case in nanoparticle devices. Field-driven ionization processes in a layer of nanoparticles are based on the fact that the major share of the voltage drop across the layer is located at the interparticle boundaries. If the interface voltage drop is strong enough, the situation depicted in Fig. 2.3b might occur, where the conduction band of one particle is at the same level as the valence band of the previous one and so forth. In this situation, surface isolating barriers are assumed that originate from poor particle-to-particle contact and/or low charge carrier densities at the nanoparticles surfaces. Then, an electron from the valence band might tunnel through this barrier to the conduction band of the next particle, leaving behind a hole and recombining with a hole in the next particle that has been created there in the same way. To make this mechanism work, a voltage per particle between the contacts is needed that exceeds the voltage corresponding to the band gap of the nanoparticles. Therefore, the voltage threshold for luminescence is higher for this mechanism, but power efficiency might still be able to reach one because a single charge carrier is able to recombine in every nanoparticles layers which leads to the unusual case of a maximum injection efficiency greater than one and equal to the number of nanoparticle layers.

Usually, the high field necessary for field-driven ionization is greatly supported by a gate structure in light-emitting field-effect based transistors.[125–129] Among them, light-emitting field effect transistors showing electroluminescence from ZnO

nanoparticles have also been reported.[125, 126] Unipolar quantum dot LEDs without gate electrode have been presented exhibiting an external quantum yield of 0.15 %.[16, 17]

2.4. External quantum efficiency

The external quantum efficiency is a frequently used measure to determine how well a device concept is working. It is defined as the ratio of emitted photons into the surrounding to the charge carriers moved through the device with the exciting current. Commonly, the total external quantum efficiency is being divided into three parts, which allows a more detailed analysis where efficiency losses are caused:

1. the luminescent quantum yield η_{QY},
2. the injection efficiency η_{inj},
3. and the out-coupling efficiency η_{out}.

These three factors result in the following relation for the total external quantum efficiency η_{ext}:

$$\eta_{ext} = \eta_{QY} * \eta_{inj} * \eta_{out}.[1] \tag{2.28}$$

The luminescent quantum yield is determined by the active material and can be used to compare the performance of different nanoparticle samples, while the injection efficiency depends strongly on the architecture of the device and will be used to compare the performance of different hole injection layers with each other. In literature, luminescent quantum yield and injection efficiency are often reported combined as internal quantum efficiency, which concludes both, quantum yield and injection efficiency ($\eta_{int} = \eta_{QY} * \eta_{inj}$). The out-coupling efficiency, which will not be optimized in this work, has also being separated by Eq. 2.28. The individual characteristics of all three components of the external quantum efficiency are discussed in the following sections.

2.4.1. Luminescent quantum yield of the active nanoparticles

The luminescent quantum yield η_{QY} is defined as follows: The share of electron-hole pairs inside the active material that recombine radiatively. In nanoparticles,

energy from an excited electronic state can be consumed in several ways. First, an electron-hole pair may recombine radiatively as mentioned. This is obviously the goal in a light-emitting device. Second, it can recombine producing heat by emission of phonons by recombination at volume defects and surface states. Third, the energy can be transferred to another electron by the Auger effect. Forth, because of the very high surface-to-volume ratio of nanoparticles, another recombination mechanism has to be taken into account for this type of material: oxidation/reduction processes that convert the energy into chemical energy. At the surface of the nanoparticles, defect and trap states are not avoidable, but they can be reduced by a core/shell structure.[130–132] The active material is the core, which is covered by a so called shell. A confinement of charge carriers to the core can be realized, if a material with higher conduction band level and lower valence band level is chosen as shell material. The surface defects of the core are passivated by the shell and the energetic confinement keeps them away from the surface defects of the shell and (re-)oxidants in the surrounding.

2.4.2. Injection efficiency

For achieving radiative recombination from electron-hole pairs in the active material, they have to be created first. The injection efficiency η_{inj} is defined as the share of charge carriers flowing through the device that form such an electron-hole pair inside the active material. This chance is determined by the following properties of the device:

1. In a LED, electrons and holes are both created in adjacent charge transport layers and have to be transferred to the active material. The chance of a charge carrier to be transmitted unscattered from one semiconductor into another one depends on the mobility of the charge carrier inside the injection layer, and the height and width of the energetic barrier at the interface for the respective band, valence band in case of holes and conduction band in case of electrons (cf. chapter 2.2.2). Scattering at the interface may lead to non-radiative recombination at interface states.

2. For an optimized injection efficiency, charge balance is mandatory.[14, 133] If there exists a majority carrier, be it holes or electrons, some of them will not

meet a partner to form an electron-hole pair on their way through the active layer unavoidably and leak through to the opposite charge injection layer.

3. A fraction of the carriers may leak into the opposite injection layer, even though there would have been a carrier of opposing charge because of the finite scattering cross section for forming an electron-hole pair. Leaking may be reduced by a band offset between active and opposite charge injection layer for the charge carriers respective band, which leads to reflection of charge carriers and increased residence time inside the active layer. In advanced devices, additional dedicated blocking layers are introduced for this purpose.

Regarding band alignment, an optimized device structure is presented in Fig. 2.4. In Fig. 2.4a, a scheme of the device showing the electron vacuum levels of conduction and valence bands throughout the device is presented, including hole transport layer (HTL), emitting layer (EML) and electron transport layer (ETL). 2.4b and 2.4c show the calculated band gap levels unbiased and with an external bias applied, respectively. The valence band of the HTL is assumed to fit exactly to the valence band of the EML, and the same is true for the conduction band of EML and ETL. The reason for this becomes clear, when the band diagram at operating voltage is consulted: no abrupt energy barrier is observed at the heterojunction in either case for the respective charge carriers, which results in less charge carrier reflection. While this would also be achieved, if the injecting band would be at higher energy for the respective charge carrier, the corresponding potential drop at the interface would result in producing heat and reducing the power efficiency of the device. On the other hand, there is a large offset between the HTL conduction band and the EML, and the valence band of EML and ETL, which leads to a high energy barrier for electrons at the interface from EML to HTL and for holes at the interface from EML to ETL, preventing charge carriers from leaking through and confining them inside the active zone. Therefore, this device architecture strongly increases the chance of charge carriers to form an electron-hole pair. The contacting materials, such as metals or transparent conductive oxides (which are degenerate semiconductors) are appreciated to have a work function similar to the respective charge transport layer, which facilitates formation of ohmic contacts. An exception is a metal/degenerate semiconductor junction, where this is not mandatory. It has been shown that barriers related to an energy offset are commonly less important because of the high number of

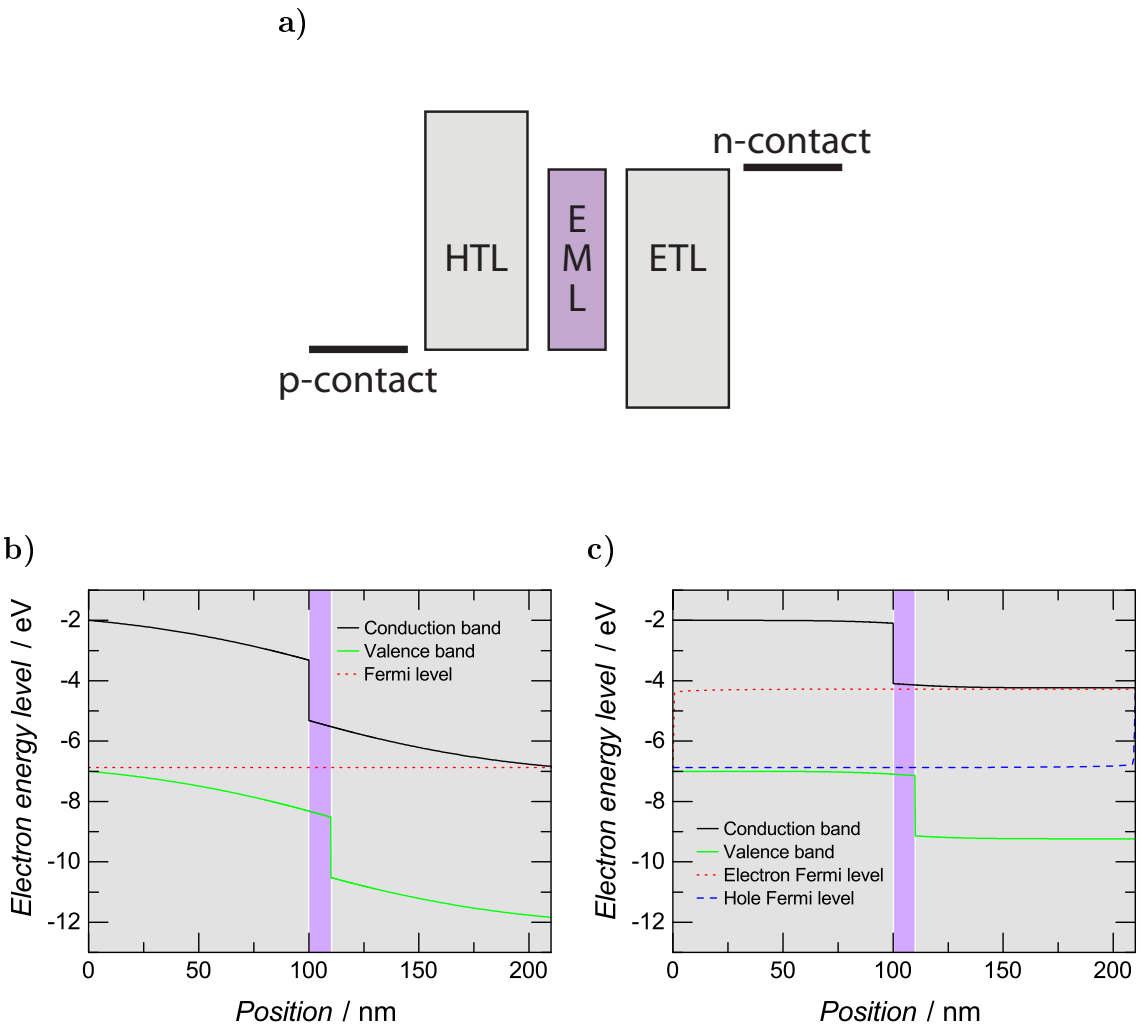

Figure 2.4. – (a) Sketch of a simple LED structure with the vacuum band levels of the involved layers. It consists of the emitting layer (EML) sandwiched between hole transport layer (HTL) and electron transport layer (ETL) with optimized band alignment. (b) Same structure with materials being in contact with each other without external bias and (c) at an external bias of 2.6 V and current density of 7.3 mA/cm^2. EML area has been filled with purple and transport layers with gray in all figures allowing for quick comparison. For more details regarding the simulation cf. Appendix A.2.

free charge carriers in the contacting layers. Therefore, tunneling injection becomes highly efficient and quasi-ohmic contacts are observed.[134–137]

Although deviations from the smooth band alignment are often unavoidable due to the limited choice of materials with specific band levels, a quantum dot device based on CdSe/CdS as EML has been presented recently with a band structure which is very close to this setup.[18] In these devices, ZnO has been used as ETL. The conduction band level of ZnO is very close to the respective value of CdSe and CdS, facilitating a good electron injection. On the other hand, the valence band level of ZnO is much lower than the one of CdSe/CdS, providing a substantial electron barrier. As HTL, NPB has been used with a substantial higher LUMO for electron blocking and a HOMO near the valence band of the quantum dots for hole injection. As a result, the internal efficiency has been reported to be near 90 %.

The injection efficiency is governed by the device architecture and the properties of the injection layers. It is therefore an efficient measure to compare different device setups, if one uses the same EML material.

2.4.3. Out-coupling efficiency

Photons generated inside the LED might get trapped or absorbed, which lowers the count of photons per charge carrier observed by an external spectator and therefore the external quantum efficiency. For average devices without dedicated measures to improve the out-coupling, about 80 % (OLEDs[95]) to 90 % (GaN epitaxial-layer LEDs[138]) of photons are lost this way. Without a proper back-reflecting mirror, even 50 % more of photons are lost, resulting in an out-coupling efficiency of only 5 % to 10 %. There are four important effects that determine the ability of a LED to release generated light into the surrounding, which is described by the out-coupling efficiency η_{out} (Fig. 2.5)[107, 138]:

1. Fresnel reflection,

2. incomplete back mirror reflection,

3. total reflection,

4. and absorption, finally.

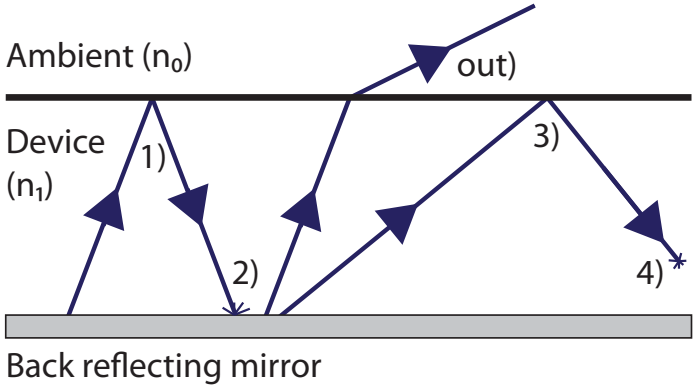

Figure 2.5. – Loss mechanisms in light out-coupling of LEDs: Aside from successful transmission of photons to the surrounding (out), photons might be trapped by Fresnel reflection (1), incomplete back mirror reflection (2) and total reflection (3), and might then be absorbed (4) before leaving the semiconductor.

Material	$\tilde{n}$
ITO	2.0[138]
Sapphire	1.78[138]
ZnO	2.1[139]
p-GaN	2.4[138]

Table 2.1. – Refractive indices $\tilde{n}$ of the materials used in the examples.

The Fresnel reflection coefficient R_F at the interface from a semiconductor material with refractive index $\tilde{n}_1$ to the surrounding with refractive index $\tilde{n}_0$ for perpendicular incident photons is given by the relation

$$R_F = \left(\frac{\tilde{n}_1 - \tilde{n}_0}{\tilde{n}_1 + \tilde{n}_0} \right)^2 . \tag{2.29}$$

In example, this equation gives a negligible Fresnel reflection coefficient of a ZnO→ITO interface of 6×10^{-4}, and a noticeable one of 1×10^{-2} for a GaN→sapphire interface. The refractive indices of these materials are found in Tab. 2.1. The second loss mechanism is total reflection.[107, 138, 140] It follows from Snell's law that every photon at an interface traveling from a media of higher refractive index to a material of lower one, that is incident above a certain angle, is reflected. This angle is called the critical angle and is given by [107]

$$\theta_c = \sin^{-1} \frac{\tilde{n}_0}{\tilde{n}_1} \approx \frac{\tilde{n}_0}{\tilde{n}_1}. \tag{2.30}$$

If photons are emitted equally in all directions within the half-space, the reflection coefficient R_{total} becomes

$$R = \frac{\pi/2 - \theta_c}{\pi/2}, \tag{2.31}$$

$$= \frac{\pi/2 - \tilde{n}_0/\tilde{n}_1}{\pi/2}. \tag{2.32}$$

This is usually the most important loss mechanism in planar semiconductors with large refraction index like ZnO and GaN, where Eq. 2.32 yields to a total reflection coefficient of about 70 % to air. Therefore, a lot of measures have been invented to reduce light trapping, like surface roughening[140] or scattering at a nanoparticle interlayer[141]. Nanorods and nanoparticles themselves possess roundly shaped surfaces, resulting commonly in alternating incident angle after every reflection and are therefore less likely to trap photons, which leads to better out-coupling properties of these materials.[142–144]

If we assume that photons are generated with arbitrary orientation of propagation and the LED is required to emit light into a certain direction by the application as it usually is, a back reflection mirror has to be used, e.g. a metal layer[138] or a distributed Bragg reflector[145]. The reflection should be as high as possible, because every absorbed or transmitted photon will be lost. (Re-)absorption occurs in every material and is minimized by choosing support layers exhibiting a band gap that is larger than the energy of the emitted photons and by minimized layer thickness. As every back-and-forth reflection elongates the way of the photons inside the LEDs, the total share of absorbed photons strongly depends on the chances of reflection.

3. Characteristics of ZnO

3.1. Crystal structure and band diagram of wurtzite ZnO

Zinc oxide is a widely investigated material for optoelectronic applications, because of its wide band gap of 3.34 eV[125] at room temperature and the high exciton binding energy of 60 meV.[146] In this chapter, the basic characteristics of ZnO as active material shall be discussed.

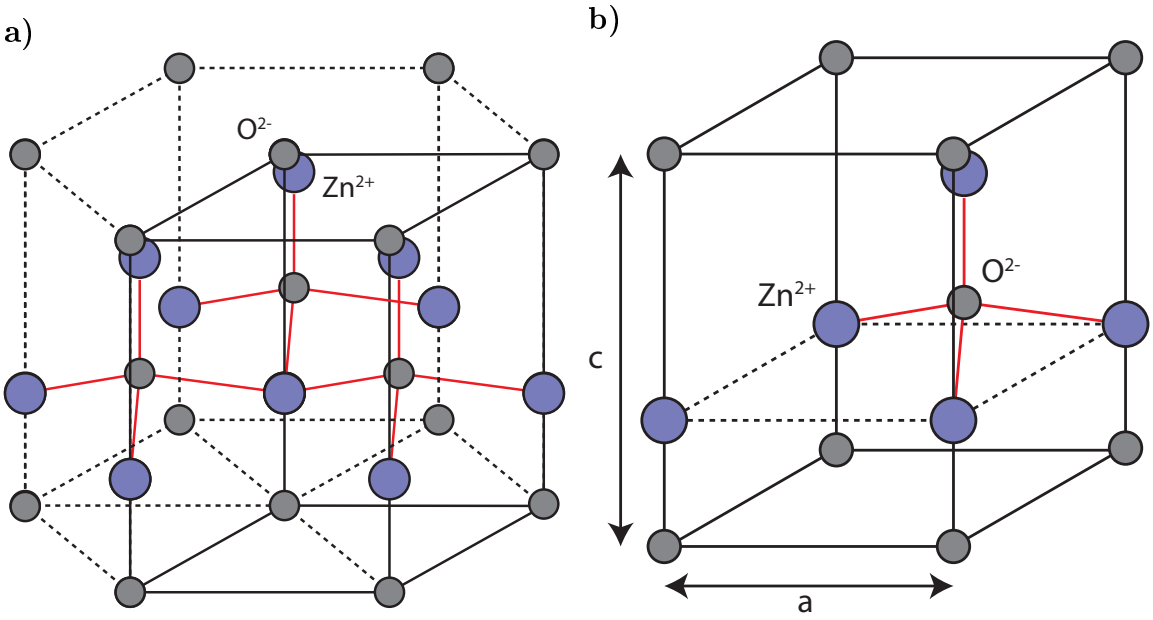

Figure 3.1. – (a) Hexagonal crystal lattice and (b) unit cell of ZnO in wurtzite configuration and its lattice constants a and c.[147, 148] Zn^{2+} ions are shown as violet spheres and O^{2-} ions as gray ones. Black lines the edges of the unit cell; red lines underline the tetrahedral coordination of ZnO.

ZnO is a II-VI compound, that exists in three different configurations: cubic rock-salt, cubic zinc blende and hexagonal wurtzite, which are described in detail in [147]. A schematic of the unit cell of the wurtzite crystal structure is presented in Fig. 3.1,

which is the most common configuration because it is the stable one at room temperature. ZnO nanoparticles usually adopt this form as well (e.g., cf. Fig. 9.2 and reports [102, 106, 149]). The wurtzite structure consists of two hexagonal closely packed sublattices with a 3/8 displacement along the threefold c-axis. The wurtzite structure has two lattice constants as shown in Fig. 3.1: a, which denotes the length inside the hexagonal plane, and c, which denotes the length perpendicular to it. They are related by the equation $c/a = \sqrt{8/3} \approx 1.63$. In case of ZnO, a and c are reported to be in the range of 3.2492 Å to 3.2503 Å and 5.2031 Å to 5.2075 Å, respectively.[150]

ZnO in cubic rocksalt or zinc blende structures are formed under special conditions, e.g. by deposition under high pressure (cubic rocksalt) or by epitaxial growth on a cubic substrate (cubic zinc blende). These configurations are not represented in any of the ZnO samples discussed within this thesis and will not be discussed further. More details are given in [147].

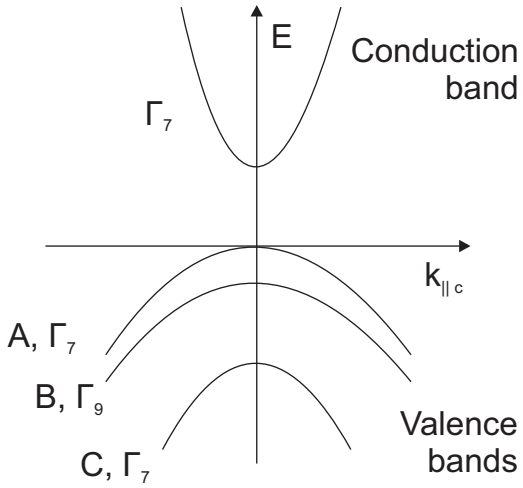

Figure 3.2. – Simplified band structure of wurtzite ZnO.[151, 152]

Wurtzite ZnO has a band structure as shown in Fig. 3.2. While there is only one conduction band, the valence band is splitted into three sub-bands which are separated by minor energy level differences. Band splitting and offset are caused by crystal field and spin-orbit splitting.[151] The A and C valence band and the conduction band have Γ_7 symmetry, while the B valence band has Γ_9 symmetry.[151] ZnO has a wide band-gap of 3.37 eV[32] at room temperature, which is the difference between the conduction band minimum and the maximum of valence band A. Valence band B is separated by 5 meV from valence band A at the Γ-point, while

the maximum of Band C is 45 meV below. Both energetic differences have been determined at low temperatures.[151] The minimum of the conduction band and the maxima of the valence band are all situated at the Γ-point which makes ZnO being a direct semiconductor. This allows optical emission without the need for a phonon to take part in the process to fulfill the conservation of momentum, making such transitions much more likely and enabling ZnO to act as active material in light-emitting devices.

3.2. Doping of ZnO

The ability of being doped is a very important characteristic of a semiconductor. Doping allows to tailor the conductivity and to form junctions that enable building of semiconductor devices, e.g. diodes and transistors.

ZnO is a material that is intrinsically n-doped with natural defects acting as donors. In example, a study has presented intrinsic bulk ZnO with a free electron density of $10^{16}\,\mathrm{cm}^{-3}$ with a mobility of $200\,\mathrm{cm}^2\,\mathrm{V}^{-1}\,\mathrm{s}^{-1}$.[153] For ZnO nanoparticles, an increased free charge carrier density due to intrinsic doping of about $10^{18}\,\mathrm{cm}^{-3}$ has been observed,[154] while the mobility decreases to a range of $2 \times 10^{-4}\,\mathrm{cm}^2\,\mathrm{V}^{-1}\,\mathrm{s}^{-1}$ to $7 \times 10^{-2}\,\mathrm{cm}^2\,\mathrm{V}^{-1}\,\mathrm{s}^{-1}$.[154–156] Nevertheless, the high intrinsic doping provides good electron conductivity, because ZnO nanoparticle layers usually still exhibit a sufficient electron mobility for many applications, which even holds true in case of very small particles with a diameter of 20 nm and less. For reference, this value is at least one magnitude above the typical electron mobility of organic electron transport layers.[157] Therefore, the increased electron mobility, compared to organic materials, has facilitated the materials application in electron transport layers in several organic and high performance nanocrystal LED concepts.[18, 155, 158]

The identification of the defect acting as donor for intrinsic doping is a controversially debated topic and no consensus could be achieved until now.[159] Three possible donors have been identified: zinc interstitials or their complexes,[159–162] oxygen vacancies,[159, 162] and adsorbed hydrogen[163]. As higher carrier concentrations have been achieved after removing hydrogen, e.g. after annealing,[162, 164] and oxygen vacancies have high ionization energies, zinc interstitials might be the most important intrinsic donor in ZnO. Apart from intrinsic doping, n-doping of ZnO

with Al[154] or In[165] have been reported. In case of ZnO:In, an electron mobility of $3.7\,\mathrm{cm^2\,V^{-1}\,s^{-1}}$ at a free electron doping concentration of $1.7 \times 10^{20}\,\mathrm{cm^{-3}}$ could be achieved.[165]

In contrast to n-doping, stable and reliable p-doping of ZnO is very hard to achieve, because compensating n-doping defects have comparably low formation energies.[101, 166] or the acceptor levels are situated too far away from the valence band edge.[167] Nevertheless, several reports claim to have presented LEDs incorporating a p-type ZnO layer, using sodium,[168] phosphorous,[146], antimony,[169], arsenic[170, 171] or nitrogen[172] as dopant. Their performance, however, is typically low.[167] To avoid difficulties arising from reliable and stable p-doping of ZnO, heterojunction LED concepts provide an alternative to homojunction ones, which combine n-type or intrinsic ZnO with a p-type semiconductor made from another material.

3.3. Optical emission properties of ZnO

ZnO is capable to emit light over a wide spectral range, spanning from the near UV over the whole visible range. UV emission originates from near band gap emission (3.3.1), while several defect structures in ZnO provide recombination levels allowing emission in every section of the visible spectrum (3.3.2). The origin of the various emission wavelengths will be discussed in the following sections together with the progress of fabricating luminous efficient ZnO quantum dots emitting at the respective wavelength.

3.3.1. Band gap related emission

The exciton binding energy of ZnO (60 meV[146]) makes excitons in this material stable at room temperature. Therefore, (near) band gap related optical transitions are significantly influenced by excitonic properties. Emission from recombining free excitons is dominant at room temperature with a transition energy of approximately 3.3 eV (376 nm).[173, 174] The only exception to this rule is the so called A-line at 381 nm,[174] which is observed in experiments on nanostructures with a high surface-to-volume ratio [174–179] and has been shown to dominate at room temperature.[174, 176] While the recombination mechanism leading to the emission at the A-line is still under debate,[180, 181] its relation to the surface is obvious from the type of systems

where it has been frequently observed. Common explanations favor excitons bound to surface defect states.[174, 176–181] Phonon replicas of both, free exciton and A-line, broaden the excitonic emission lines at room temperature.[174]

Upon nanoparticle size decreasing into the regime of the excitonic Bohr radius, which is reported for bulk ZnO to be in the range from 1.8 nm[147, 182, 183] to 2.8 nm[184], continuous bulk exciton energy levels separate from each other into discrete energy levels and the band gap increases. This effect is called quantum confinement, which has been observed in many nanoparticle materials including CdS,[123] CdSe,[132] InP,[185] Si[186, 187] and ZnO,[182, 188–192] as well. Usually, it can be described by a simple effective mass model, but in case of ZnO a strong discrepancy between this model and experiment is well known and widely discussed in literature.[182, 188–192] Some of the main reasons being discussed are: Stokes shift between absorption and emission peak due to different fine structure states involved,[188, 192] or due to phonon interaction,[188] leakage of the carrier wave function to surface states (i.e. a finite well depth height),[182] or Stark shift due to a strong electric field due to surface charges.[191] Therefore, no general relation between the nanoparticles size and the band gap energy in ZnO quantum dots that models the behavior in all systems could be presented.

Although several efforts have been made to increase it, the quantum yield of the band gap emission in ZnO quantum dots is very low in general and below 1 %, and no substantial progress to increase it could be achieved so far.[193–195] The reasons behind this are surface states, e.g. created by adsorbing of OH-groups,[195] and the low defect formation energies in ZnO.[196] While surface states might be controlled by applying ligands or a shell, it is very hard to make a sample without any defects. All of these surface and defect states provide radiative and non-radiative relaxation channels that compete with the excitonic transition and therefore decrease its efficiency.

3.3.2. Defect state related emission

In this section, the defect related emission of ZnO in the visible range of the spectrum will be discussed. A lot of optical active defects are known for ZnO, including zinc and oxygen vacancies, interstitials, antisites and various surface related states originating from adsorbed groups or ligands. Some transitions involve the conduc-

tion or valence band, while others are inter-defect transitions. Emission wavelengths will be discussed separately for the violet to blue, the green, and the yellow to red region due to transitions within these ranges being attributed to a similar group of defects. This structure should by no means distract from the fact that the origins of all defect transitions and their assignment to emission wavelengths is a very controversial debated topic and is by no means fully understood.[173, 178, 180, 189, 197–199] Progress in this field is essentially becoming difficult because the various defect types are being influenced by the positioning within the crystal lattice. This might be affected by the size, the shape and the exact creation process of the individual ZnO sample, including e.g. method, temperature, concentration of reactants and annealing conditions in different atmospheres.[97, 197]

Violet to blue emission

ZnO emission in the violet and blue spectral ranges (specifically between 400 nm to 488 nm) is commonly attributed to electrons in a donor state, which is most often identified as zinc interstitial, recombining with holes in the valence band.[22, 199–202] Emission in the lower energy, blue section of this spectral range has also been attributed to coupling of defect sites to a disordered lattice,[199] and to donor-acceptor transitions from zinc interstitials to zinc vacancies.[203] Violet to blue emission is typically weak compared to emission at other wavelengths,[22, 199] probably caused by the low stability of the zinc interstitial defect. Experimental results from optical detection of electron paramagnetic resonance at increasing temperature prove zinc interstitials to be much less stable than other defects.[204] This is supported by theoretical calculations showing that zinc interstitials are fast diffusers exhibiting a very low migration barrier of 0.57 eV, which leads to the instability of the defect.[196]

One report has presented very efficient, blue emitting ZnO quantum dots made by a solution based process that exhibit a record quantum yield of 76 % at an emission wavelength of 440 nm.[102] However, it has been concluded from PLE experiments that the emission of these quantum dots does not originate from ZnO volume, but from surface states that are attributed to complexes formed with the ligand oleic acid. These oleic acid molecules have been used to replace hydroxyl groups usually present after precipitation. The assumption has been supported by photoluminescence measurements in various chemical surroundings. The blue emission intensity

is shown to decrease with increasing size, which is a clear indication of a surface related mechanism, as well. Other reports show silica coated ZnO nanoparticles with a photoluminescence quantum yield of up to 60 %.[205, 206] As the emission peak wavelength of bare and silica-coated ZnO quantum dots is similar, this might be a hint that the emission is indeed from ZnO in this case.[205] However, there have been no further investigations on the responsible luminescent mechanism within this publication.

Other reports communicate the opinion that transitions from the conduction band to zinc defect acceptor states yield to blue emission from ZnO. These acceptor states have been identified to be zinc interstitials at the surface[198] or zinc vacancy-hydrogen complexes.[207] An involvement of either conduction band or valence band, however, is widely accepted and is supported by the temperature-induced, s-shaped shift of the violet-blue emission wavelength.[197, 200]

Green emission

Green emission (497 nm to 564 nm) is the most commonly reported defect emission from ZnO, and several different recombination mechanisms have been reported for radiative recombination in this section. It is very likely that indeed multiple recombination mechanisms exists that lead to green-yellow emission with their relative intensity depending on the density of recombination centers in the specific ZnO sample. This density distribution may be influenced to a great extent by the creation process of the sample. The most commonly mentioned transition involves radiative recombination at oxygen vacancies.[189, 194, 208–213] In structures with high surface-to-volume ratios, such as small nanoparticles, this recombination process is strongly supported by OH groups, which bond to the ZnO surface in humid ambient air or in ethanol.[189, 194, 212, 214]

Most of the ZnO samples exhibiting a high luminescent quantum yield emit in the green region. Silane-functionalized ZnO nanocrystals have been presented with a peak emission wavelength of 545 nm at a quantum yield of up to 20 %.[215] Another report presented ZnO nanoparticles capped with 3-(trimethoxysilyl)propyl methacrylate (TPM) with a quantum yield of up to 61 % at an emission center wavelength of 492 nm, while the bare nanocrystals emitted at almost the same wavelength (494 nm) at a lower, yet respectable quantum yield of 28 %.[23] The emission wavelength could

be redshifted to approximately 505 nm and 525 nm by reducing the concentration of the catalyst LiOH in the precipitation step. ZnO nanoparticles capped with poly(amidoamine) (PAMAM) dendrons show increased quantum yield with storage time, which increases from 21 % to 59 % after 20 days of storage in water at a center emission wavelength of 550 nm.[216]

Unfortunately, neither the mechanism of the emission at the different wavelengths leading to the high quantum efficiencies measured on these samples nor the cause for the shift in [23] could be elucidated, however. Dijken and co-workers investigated the insitu luminescent quantum yields of very small ZnO quantum dots with a diameter of 1.4 nm to 1.9 nm, which are increasing with decreasing diameter up to a value of 21 %. They attributed the emission to the commonly mentioned mechanism involving a singly-ionized oxygen vacancy.[208]

Despite the great popularity to explain green luminescence by relating it to singly ionized oxygen vacancies, it has been demonstrated that it cannot be the only recombination center leading to emission in this spectral range. Green emitting ZnO quantum dots have been reported that do not incorporate singly-ionized oxygen vacancies, which has been demonstrated by an absence of the signal of this paramagnetic state in EPR measurements.[217] Additionally, there have also been reports that claim oxygen vacancy/zinc vacancy donor-acceptor pair recombination,[218, 219] oxygen interstitials[22, 198, 220] and anti-sites[220] are involved in green emission from ZnO. Oxygen interstitials seem to emit at higher wavelengths compared to oxygen vacancies[22] and antisites[22, 220], and they appear to be less efficient radiative recombination centers compared to oxygen vacancies[22]. As reports on these mechanisms are rare, however, further research will be necessary to elucidate the characteristics of emission related to oxygen vacancy/zinc vacancy donor-acceptor pair recombination, oxygen interstitials and antisites.

Yellow to red emission

Emission in the yellow to orange regime (576 nm to 600 nm) is observed in ZnO samples that have been made under oxygen rich conditions. Therefore, it is most commonly attributed to oxygen interstitials.[221, 222] The exact recombination mechanism is not fully understood yet. However, yellow emission has been observed to be facilitated by OH groups at the surface of nanostructures, similar to green emis-

sion.[178, 223, 224] ZnO nanoparticles exhibiting a quantum yield of 19 % and a central emission wavelength of 579 nm have been reported, which have been made by an ethanol based precipitation method at pH 6.[24]

Similar to yellow to orange emission, orange to red emission (600 nm to 697 nm) is commonly observed in ZnO samples that have been made under oxygen rich conditions, and is therefore often attributed to be related to oxygen interstitials, [203, 225–227] while the exact mechanism remains unclear, as well. The fact that no single defects can be assigned to emission in this spectral range by energy level calculations[220, 228] and the high temperature stability support the concept that the responsible recombination centers might be defect complexes that most likely involve at least one oxygen interstitial.[178] Other reports assume that yellow, orange and red emission all involve holes in an oxygen interstitial level, but electrons from different energy levels originating from band gap or donor states.[203, 228] Aside from oxygen interstitials, zinc interstitials[229] and complexes including a zinc vacancy[178] have been suggested to act as red emitting recombination centers. Obtaining a high quantum yield in the red section of the visible spectrum remains a challenge and no highly efficient, red emitting ZnO quantum dots have been reported until the present day.

4. Experimental methods

4.1. Deposition of thin-films by radio-frequency magnetron sputtering

Sputtering is a deposition technique that has become extremely popular in compound semiconductor device technology because it preserves stoichiometry much better than evaporation processes.[230, 231] Additional advantages include improved adhesion, film homogeneity and better control of the deposited layer thickness.[231] The fundamental process involves ionization of a processing gas, such as argon, nitrogen or oxygen. Electrons are accelerated by applying an electric field between the substrate and the target, which consists of the material to be deposited. This field might either be static (dc sputtering) or alternating (ac sputtering), as described below. More electrons are separated from the atomic core upon collision of these very fast electrons with processing gas atoms, creating ions, and even more free electrons. After being accelerated by the electric field by themselves, even more free electrons are created upon further collisions. As this process repeated, an ion gas is created. The ions are driven toward the target by a negative electrical potential. Because they possess a much higher mass when compared to electrons, ions are able to gain a momentum that is sufficiently high enough to eject target surface atoms upon collision, which may then deposit on the substrate and form a film.

Sputtering processes are known in a lot of variations, among them direct current (dc), alternating current (ac, mostly radio frequency (rf)), magnetron and reactive sputtering, and combinations of these. The historically first developed variant has been dc sputtering.[230] Here, electrons are simply accelerated by a static field. Although the required setup is very simple, the plain dc-sputtering technique is not used in production environments anymore because of its low deposition rate, which is of the order of a few hundred ångström at most for many metals.[230] This results

from the low electron scattering ionization cross section, which causes many electrons to reach the anode without a single ionization process.[230] Also, this method is restricted to conductive target and substrate materials because otherwise they would be charged by the constant current of ions and electrons. This would create an opposing field and impede the process.[230, 231]

The limitation to conducting materials has been overcome by the development of ac sputtering processes. Typically, a radio-frequency field at 13.56 MHz is superimposed to a constant bias. Because of the high frequency, only electrons are able to follow the alternating share of the electrical field by performing an oscillating movement, while the influence on ions with much higher mass per electrical charge is negligible. This has two effects. First, electrons and ions are separated, which creates a plasma. Second, the electrons charge the isolated target when it is at positive bias, while the ions are not able reach the electrode due to their higher mass. At negative bias, the electrons are impeded from leaving and decharging the target by the extraction energy. The substrate is prevented from being charged by being grounded. Therefore, the target is negatively self-biased on time average, and positive working gas ions are accelerated to collide with it in analogy to dc sputtering. Without a requirement of a current for ac sputtering, various types of materials can be deposited by it, be it metal, semiconductor or insulator.

Both, dc and rf sputtering, can be combined with a magnetron to enhance the deposition rate.[230, 231] A magnetron arrangement consists of several permanent magnets that create a magnetic field strongly oriented in plane with the target.[232] This field enhances the density of electrons in close proximity to the target, allowing for sustaining the discharge plasma at lower voltages.[230, 231]. The increase of the electron density is achieved by elongating their travel distance by directing them on a spiral path utilizing Lorentz force.

Here, we use the rf magnetron system tectra SputterCoater. This type of system allows to deposit the rather insulating materials NiO and WO_3 at sufficiently high rates as discussed before. The plasma is ignited by a radio-frequency source operating at 13.56 MHz with a maximum power output of 300 W. The substrate is mounted on a sample holder approximately 8 cm from the target. The target itself is mounted in a sputtering gun at the bottom of the chamber. Oxygen and argon gas flow rates for reactive sputtering are steered by two mass flow controllers that set the ratio of both gases inside the chamber. The deposited layer thickness is supervised by changes of

the resonance frequency of an oscillating quartz crystal.

4.2. Epitaxial growth of GaN using MOVPE

The p-GaN hole injection layers used here have been made using metal-organic vapor phase epitaxy (MOVPE) and have been characterized electrically by the department of semiconductor technology at the University of Duisburg-Essen. Epitaxial growth processes are widely utilized in the semiconductor industry due to the superior material properties deriving from the single crystalline structure. MOVPE is the standard process for nitride growth because of lower requirements on the vacuum level and higher growth rates compared to molecular beam epitaxy.[233] The fundamental steps of an MOVPE process are as follows[230, 233]: The reactants are kept in bubblers and are streamed into the reaction chamber with a carrier gas. Typically gas-phase reactions occur, before the precursors diffuse to the heated substrate surface, where they are adsorbed. They diffuse over the heated semiconductor surface and are subject to further reactions, until the products are either incorporated into the crystal or are desorbed again, together with the reaction by-products. The desorbed molecules will then be streamed to the exhaust.

The process temperature is a critical parameter for MOVPE growth. Three growth regimes can be distinguished, reaction limited, diffusion limited and desorption limited.[233] In the reaction limited regime, the temperature is too low for the reaction to take place shortly after the reactants have moved a lattice spot. The reaction limited growth rate increases exponentially with increasing temperature until the diffusion limited regime is entered. Within this regime, growth is limited by the rate at which reactants are transported to the semiconductor surface. Diffusion is not a direct function of temperature, therefore the growth rate is almost stable throughout this regime. If the temperature is increased further, an increasing share of reactants is desorbed before the reaction took place, and the growth rate decreases exponentially. Therefore, the temperature is chosen to be in the diffusion limited regime, to ensure a stable and fast growth process.

GaN samples presented within this work have been prepared using the Aixtron 3x2" CCS MOVPE system. $Ga(CH_3)_3$, NH_3 and Cp_2Mg (Bis(cyclopentadienyl)magnesium, metal-organic source for p-doping) have been used as precursors, and N_2 has been the

carrier gas. The formation of GaN follows a complex reaction chain, which details are found in [233]. It can be summed up to

$$\mathrm{Ga(CH_3)_3 + NH_3 \xrightarrow{temperature} GaN + 3CH_4}. \tag{4.1}$$

Immediately after the growth process, incorporation of Mg in GaN films is very bad.[233] It has been enhanced by a post-growth activation step at 750 °C for 20 min.

4.3. Fabrication of ZnO nanoparticle LEDs

Following, the standard procedure for processing of the nanoparticle devices is presented, which has been followed unless special changes are announced in the respective chapter.

1. Cleaning of substrates

Substrates have been degreased in de-ionized water (DI) admixed with a few drops of common commercial dish washing cleaner. After subsequent rising with DI water, samples have been cleaned in a beaker with boiling acetone for two minutes. After that, the beaker has been placed in an ultrasonic bath for another two minutes. Subsequently, both steps have been repeated using ethanol. Finally, the substrates have been rinsed again with DI water and have been blown dry by a nitrogen pistol. For ITO, FTO and NiO covered substrates, a UV-ozone treatment has been carried out (device FHR UVOH 150 LAB) in an additional step to remove residual organic contamination and to increase the surface tension. This has been has proven to optimize wetting conditions for butyl acetate used as solvent for spin-coating of the nanoparticles, which follows immediately after UV-ozone cleaning.[97]

2. Deposition of p-contacts (only devices with GaN)

Metallic p-contacts have been evaporated on p-GaN only, ITO and FTO have been contacted directly. Au/Ni p-contacts on GaN have been deposited according to Fig. 4.1 through a shadow mask at a base pressure of approximately 10×10^{-6} mbar. Evaporation of metal contacts has been done on the Oerlikon Leybold Vacuum UNIVEX 350 equipped with a FerroTec M-6 ebeam evaporator. Ni has been deposited

on the substrate at a rate of 0.1 nm/s to 0.3 nm/s by electron beam evaporation from a half-filled vitreous carbon crucible. If a crucible is used for the first time, the nickel has to be melted very slowly with increasing electron beam current in the course of an hour in order to avoid excessive spitting of the metal. Subsequently, Au has been evaporated thermally at layer growth rates of 0.05 nm/s to 0.1 nm/s.

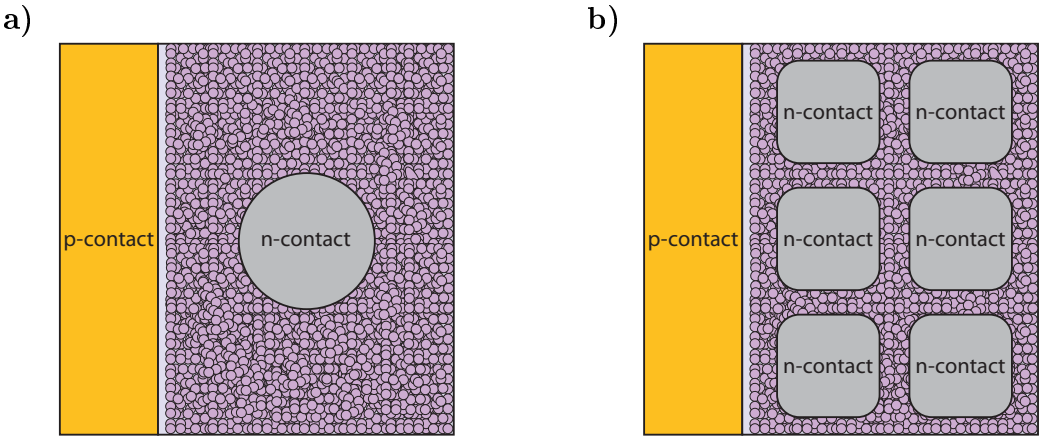

Figure 4.1. – Contact setups with the side anode contact (golden area), and (a) one centered circular aluminum cathode contact with a diameter of 3 mm or (b) six square shaped aluminum contacts with a length of 2.5 mm.

3. Spin-coating process

Spin-coating has been performed on the SCS G3P-8 system utilizing the following procedure described in [97] to produce dense films of ZnO nanoparticles: A dispersion volume of 40 µl to 50 µl has been dropped in the middle of the area to be coated and the substrate rotation has been initiated immediately after that. Initially, the substrate rotation has been accelerated by 2 rpm/s to spin at 10 rpm for 10 s in order to wet the whole area. Afterwards, rotation has been accelerated by 400 rpm/s and has been kept at 4000 rpm for 60 s. Thereby, excess dispersion has been spun off and a 100 nm to 400 nm thin, homogeneous ZnO nanoparticle layer has been left on top of the substrate. The variation of the thickness is attributed to different nanoparticle diameters and/or different dispersion concentrations, because the thinnest layers have been formed after filtration of the dispersion as described in chapter 8.2.2.

4. Annealing of ZnO nanoparticle layer (all devices without GaN)

After spin-coating, substrates have been dried on a hot plate at 150 °C for 30 min.[234] This step has been omitted for GaN based devices in order to prevent temperature-induced acceleration of GaN surface oxidation.

5. Deposition of n-contacts

Aluminum has been used to contact the ZnO nanoparticles layers. It has been evaporated at rates between 0.25 nm/s to 1 nm/s from either a TiB_2-BN or a vitreous carbon crucible (product name FABMATE) through a shadow mask. Because Al easily oxidizes, the chamber has been evacuated for at least 10 h prior to deposition resulting in very low base pressures of about 7.8×10^{-7} mbar to 1.6×10^{-6} mbar. Two different arrangements of n-contacts have been used throughout this work (Fig. 4.1).

5. Luminescent ZnO nanoparticles as active material for LED applications

5.1. Optical properties

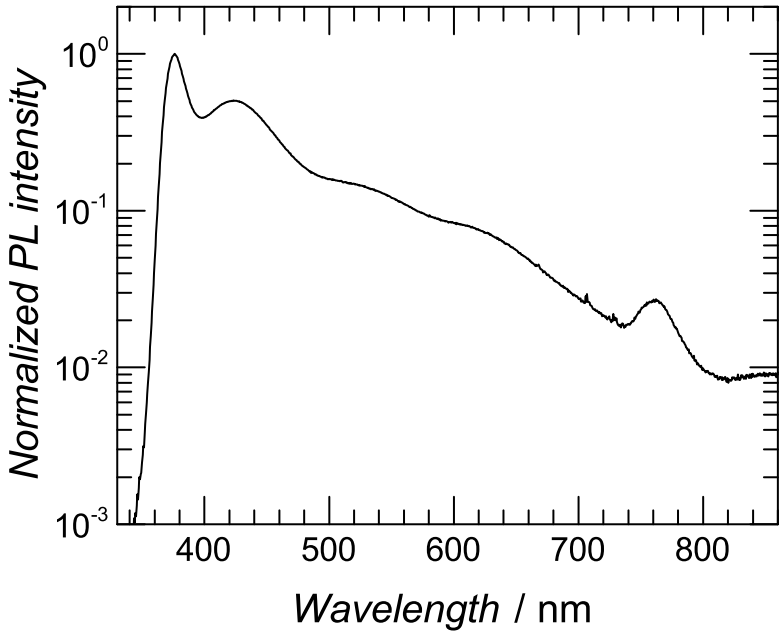

Figure 5.1. – Normalized photoluminescence (PL) spectrum on logarithmic scale of a ZnO nanoparticle layer spin-coated from a VP AdNano® ZnO20 dispersion made by Evonik Industries. Excitation power is 15 mW/cm^2.

The LEDs presented in chapters 6, 7 and 8 use an active ZnO nanoparticle layer that has been made from a dispersion produced on industry scale by Evonik Industries (VP AdNano® ZnO20 in butyl acetate). The nominal particle diameter of this dispersion is 20 nm. Aged particles, like the ones used here, however, can grow up to 150 nm, as shown in reference [235]. The production process has been published

earlier.[103] The photoluminescence spectrum of two nominally identical dispersions from the same production batch are shown in Fig. 5.1 at an excitation intensity of 15 mW/cm^2. The emission is centered around 377 nm for near band gap emission in the UV, 425 nm to 435 nm in the blue, 535 nm in the green, and 620 nm in the red spectral range, respectively. Emission peaks above 750 nm are attributed to second order detection of the UV and blue luminescence. Blue luminescence is commonly attributed to zinc interstitials, green to oxygen vacancies and red to oxygen interstitials (cf. 3.3.2 chapter for details). All devices presented within this publication have been made from this dispersion in order to enable a clear comparison between the concepts. The quantum yield of the nanoparticles in this dispersion has been determined to be 2.3×10^{-3} by a comparative method described in chapter A.1.1. This is a typical value for a ZnO sample that exhibits the major share of its emission in the UV range.[193, 194]

5.2. Simple device concept

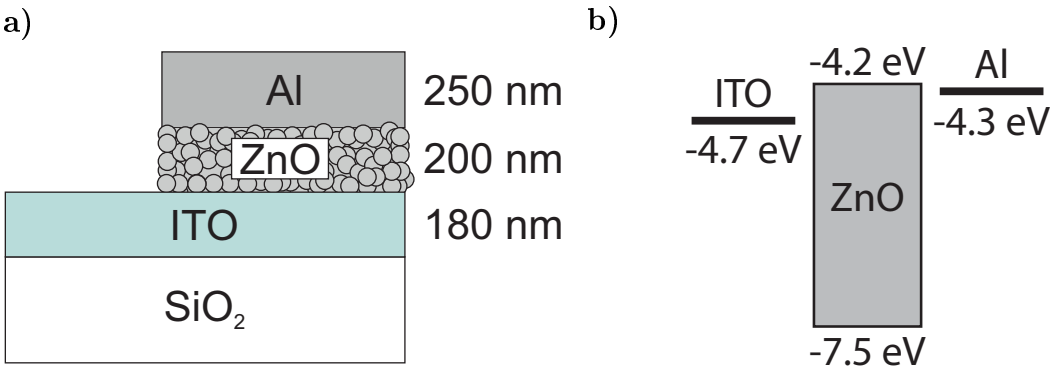

Figure 5.2. – (a) Schematic of basic ZnO LED layer design. The length specifications refer to the respective layer thickness. (b) Basic ZnO LED band level diagram in vacuum without contact of the materials to each other, showing the electron energy with respect to the vacuum level.[125, 236, 237]

The most simple nanoparticle light-emitter consists of two contact layers and a nanoparticle layer between them. Devices with ZnO nanoparticles sandwiched between ITO and an aluminum electrode have been fabricated from the VP AdNano® ZnO20 dispersion as described in chapter 4.3 (Fig. 5.2a). Similar concepts have already been published.[97, 234, 238]

The vacuum band level diagram is presented in Fig. 5.2b. On the electron side, a very good match between the work function of aluminum and the conduction band level of ZnO is observed, which results in ohmic contacts as it has been confirmed many times independently (cf. e.g. [239–241]). On the other hand, this concept creates a very large barrier at the p-contact. Electrons from the ZnO valence band have to overcome a potential difference of 2.8 eV to get into the ITO layer and to leave behind holes in ZnO. Without a p-type semiconductor, this is an unipolar, electron-only device, as discussed in chapter 2.3.2.

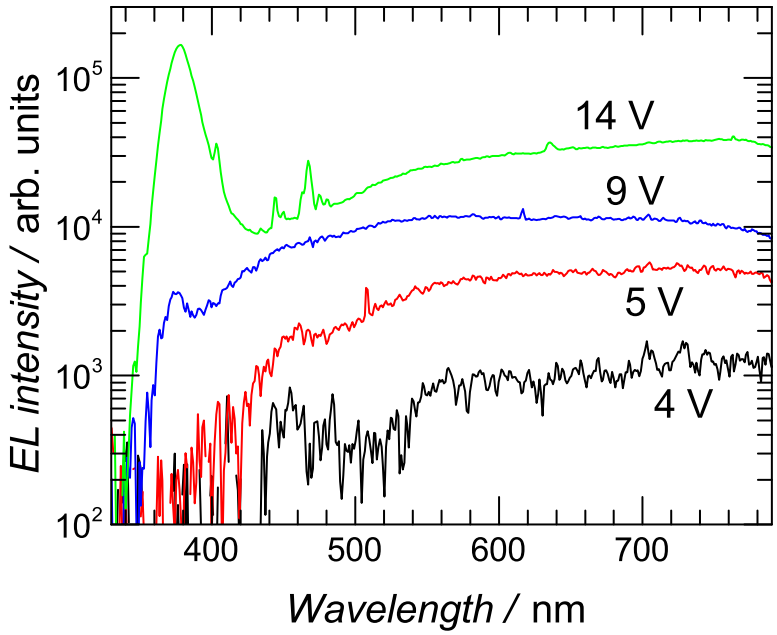

Figure 5.3. – Electroluminescence intensity of the simple ZnO nanoparticle LED in dependence of the wavelength for applied voltages of 4 V, 5 V, 9 V, and 14 V.

The characteristic electroluminescence spectra of the simple ZnO LED are summed up in Fig. 5.3. Emission spectra become observable at 3.5 V to 4 V, where one part of the emission is centered around 440 nm to 460 nm in the blue range and a very broad emission covering the whole visible spectral range above 550 nm is observed. After increasing the voltage to 5 V, the emission gets half a magnitude more intense, but the shape of the spectrum is very similar. At an applied bias of 9 V, UV EL becomes observable centered at 374 nm. It is strongly increased in intensity at 14 V, while the emission peak wavelength is shifted to 377 nm, which is identical to the wavelength

observed in PL (Fig. 5.1). The current/voltage characteristic of the simple devices is

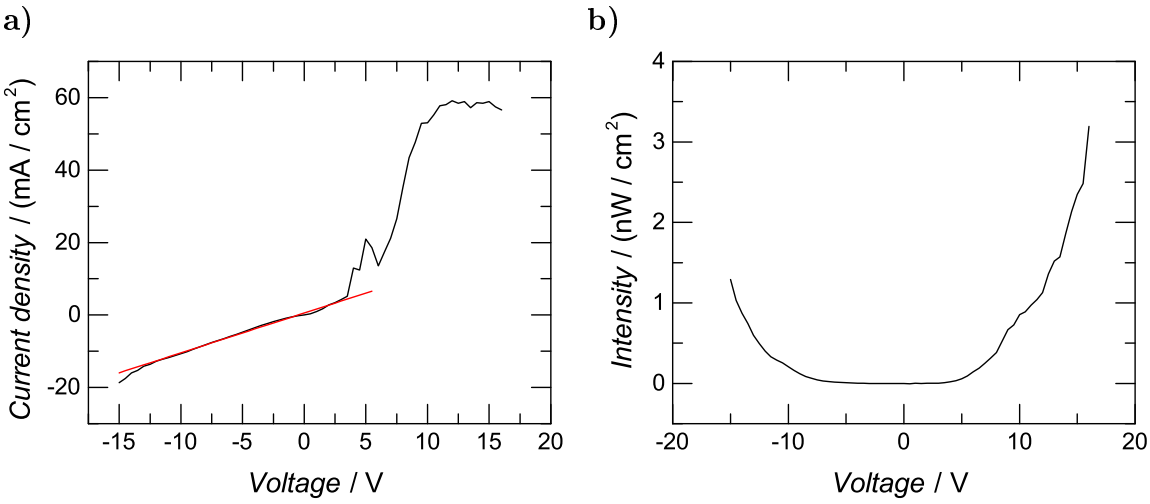

Figure 5.4. – (a) Current / voltage characteristic and (b) electroluminescence intensity as a function of voltage of the simple ZnO nanoparticle LED (black). The red line in (a) shows a linear fit of the current as a function of voltage between −12 V and 3.5 V.

presented in Fig. 5.4a. In forward direction, almost linear behavior with a total device resistance of about 10 kΩ is observed at low voltages up to 3.5 V, which is caused by an absence of a barrier for electrons as seen in the basic energy level diagram in Fig. 5.2. The small non-linearity is expected and results from clearing of the depletion zone at the ZnO / ITO interface. Above 3.5 V, suddenly rapid jumps in current are measured, and the device current gets unstable with several setbacks of current. At 9.5 V and above, the increase of current with increasing voltage is reduced, and it is completely stopped above 11 V where the current remains almost constant. Sudden setbacks of current with increasing voltage have been frequently observed, especially for devices with high dissipated power. The decrease of current might be attributed to thermal induced annealing of zinc interstitials. Zinc interstitials are assumed to be contributing to n-doping of intrinsic ZnO,[159–162] and have been reported to be rather unstable.[204] In backward direction, measured afterwards, the device is very stable indicating that unstable current influencing defects have already been annealed while the device has been run in forward direction. Up to about −12 V, the current-voltage characteristic is linear with a resistance identical to the one observed in forward direction at voltages below 3.5 V.

The electroluminescence intensity versus voltage is presented in Fig. 5.4b. The shapes of the curves in forward and reverse direction are very similar. The emission detection threshold is lower in forward direction (3 V) compared to reverse direction (4 V). The values of intensity are rather low, and the maximum is observed in forward direction at 3.2 nW/cm^2, owing to the much stronger current. Nevertheless, the correlation between emission intensity and current density seems to be rather weak, which is underlined by two observations. First, the strong super-linearity of emission intensity in reverse direction does not match to the linear behavior of the current in the same direction. Second, an increase of emission intensity at high positive voltage is observed, where the current is almost constant. An explanation can be given as follows: Because all materials are n-conducting, the charge carriers are electrons, which majority leaks through the device without taking part in a radiative recombination process. Only a minority of electrons are extracted from ZnO luminescent defect states and its valence band. Even if the amount of extracted electrons from these states is increased at higher voltage, this is not necessarily noticeable in the current-voltage measurement, because the leaking current is much stronger than the current related to extraction and subsequent radiative recombination.

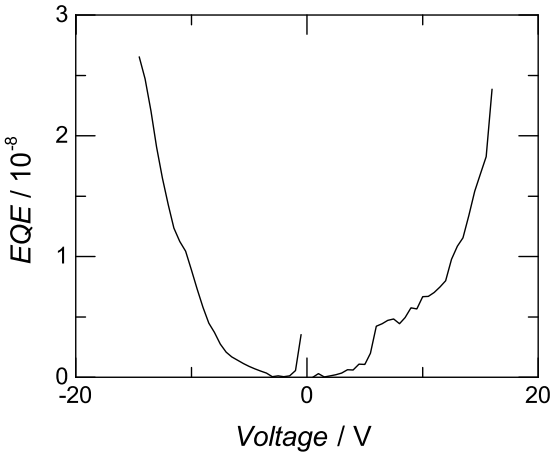

Figure 5.5. – External quantum efficiency characteristic of the simple ZnO nanoparticle LED.

The external quantum efficiency resulting from these measurements is presented in Fig. 5.5. It is very similar in both directions if the rapid jumps originating from the current behavior in forward direction are neglected. The recorded EQEs are in the order of 1×10^{-8}. Even with the poor quantum yield of the active nanoparticles in

mind, this value is very low. This is typical for an electron only device,[16] as there is no mechanism to actively keep the charge carriers from leaking through the ZnO layer without recombination and no favoring of radiative processes over non-radiative processes has been generated by the device design. The injection efficiency can be estimated to be in the order of 10^{-4} using a typical out-coupling efficiency of OLEDs without back-reflector of 10 %.[95]

Reports of devices without any support layers are very rare in literature. As mentioned, similar devices made from nanoparticles made by Evonik Industries have been reported that are based on ITO[238] and FTO[234] substrates. Despite incorporating ZnO nanoparticles being made using the same machine and process, the devices presented in these reports show higher current densities and a different, yellow to red emission spectrum. The dispersion used for investigations and devices presented here has been stored for a longer time after production which leads to out-diffusing of less stable defects being progressed further. This is most obvious if one compares the PL measurements from these publications with Fig. 5.1 regarding the intensity in the blue spectral range, which is much for the dispersion used here. As zinc interstitials are commonly related to both, blue photoluminescence and intrinsic n-doping, this matches well with the observed reduction of blue electroluminescence and current density after incorporation into a LED. This explanation is supported by the low stability of zinc interstitials in ZnO.[196, 204] The reduced defect density also leads to pronounced UV emission of these devices when compared to the ones reported in [234, 238].

6. Electron extraction with WO_3

6.1. Concept

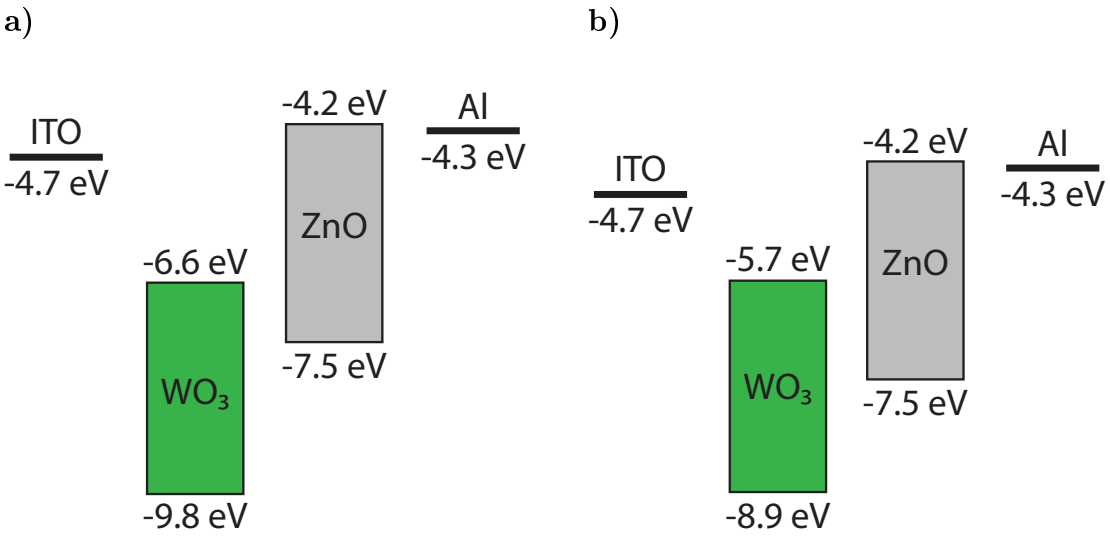

Figure 6.1. – Basic WO_3/ZnO vacuum band level diagram without contact of the materials to each other, showing the electron energy with respect to the vacuum level (a) before and (b) after exposure of tungsten trioxide to ambient atmosphere.[125, 236, 237, 242–244]

Tungsten trioxide is a metal oxide that exhibits a very low conduction band level of $-6.6\,\mathrm{eV}$.[243] Upon exposure to oxygen atmosphere, however, it is known that it is increased significantly to $-5.7\,\mathrm{eV}$.[244, 245] Because tungsten trioxide surfaces are known as strong absorbers, e.g. for water and hydrocarbon derivatives, the increase of the work function has been assumed to be related to absorbtion of ambient gas molecules.[246, 247] Tungsten trioxide is intrinsically n-conducting with oxygen vacancies acting as shallow donors.[242] This enables the use as electron extraction layer in electrical devices. The underlying concept involves electrons tunneling from the adjacent material into the electron extractors conduction band, leaving behind

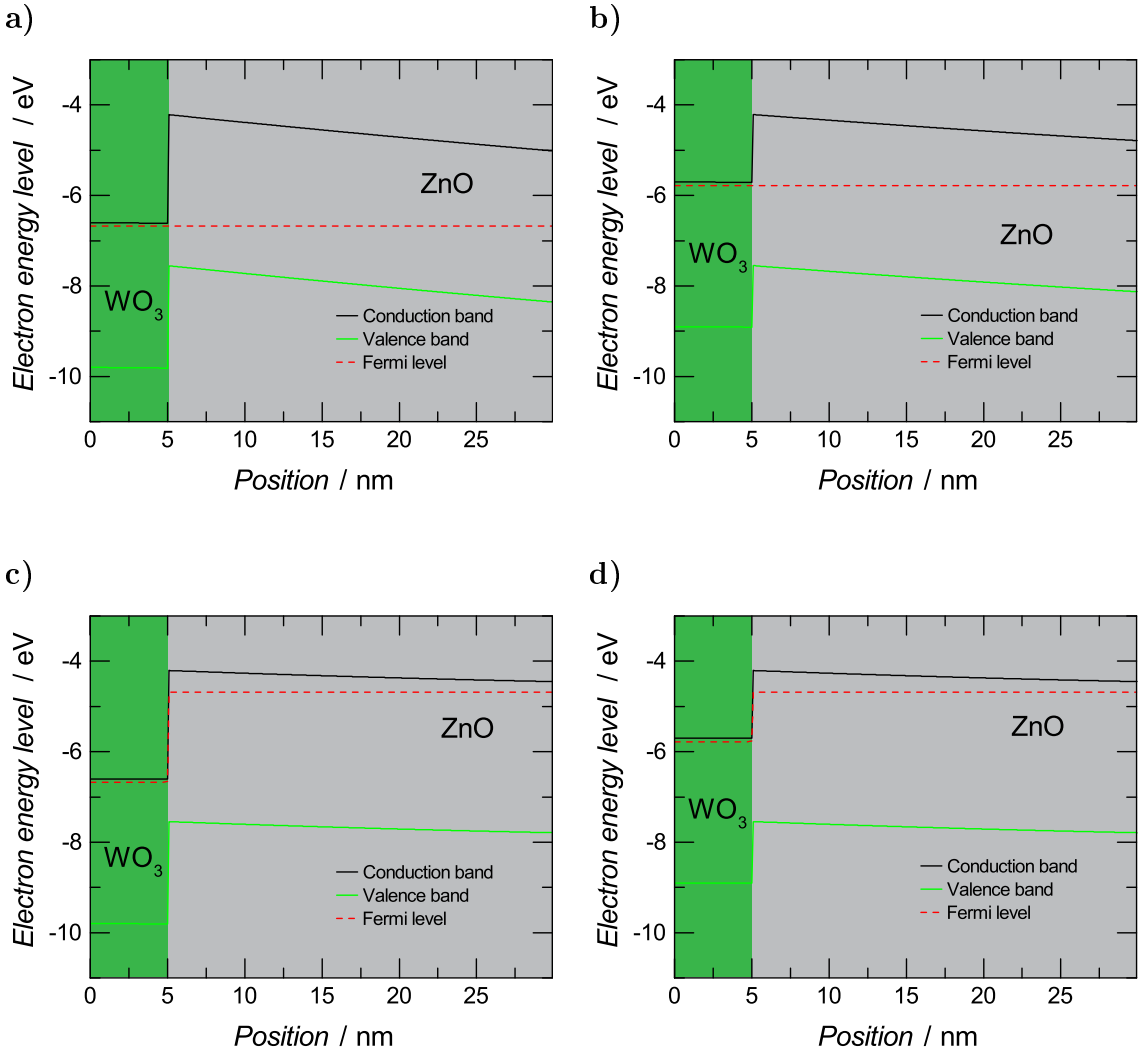

Figure 6.2. – Simulation of conduction band levels, valence band levels, and (quasi) Fermi levels of WO_3/ZnO structures; (a) without external bias, (b) WO_3 pre-exposed to air without external bias, (c) at external bias of 2 V and current density of 18 mA/cm^2, (d) WO_3 pre-exposed to air at external bias of 1.1 V and the same current density of 18 mA/cm^2. WO_3 layer has been filled with green and ZnO layer with gray in all figures allowing for quick comparison. For more details regarding the simulation cf. Appendix A.2.

a hole in the target state. It has been invented for use in light generation devices for OLEDs[248] to create holes in the adjacent hole transport layer. WO_3 has been studied extensively since then due to the good performance that has been observed including reduced turn-on voltage and increased efficiency. Additionally, WO_3 enabled a simplified device design by replacing multiple organic layers without a reduced performance.[242, 245, 247, 249–252]

Basic vacuum band level diagrams for a WO_3/ZnO LED are depicted in Fig. 6.1, without and with preexposure of WO_3 to oxygen, respectively. As the tungsten oxide layers have been in contact with ambient air after deposition, energy levels are assumed to be similar to 6.1b. Electrons from ZnO defect states at an energy level above or comparable to the WO_3 conduction band edge are suspected to tunnel into the WO_3 conduction band, leaving holes behind. These holes may then take part in radiant recombination. A noticeable extraction from the valence band is not suspected, because the barrier is still about 1 eV to 2 eV.[19]

In order to get a better understanding of the electronic properties of a WO_3/ZnO junction, simulations of band diagrams are presented in Fig. 6.2, with and without external voltage applied. Fig. 6.2a shows an increase of the hole concentration in ZnO near the interface of unexposed WO_3 without bias, as indicated by the Fermi level moving towards the ZnO valence band. This is caused by the very low work function, which makes electrons move from ZnO to WO_3. This effect is much weaker for the air exposed WO_3 (Fig. 6.2b), where the Fermi level remains in the upper half of the band gap. On the WO_3 side of the junction, a very steep potential drop is observed, which results from the exceptional large static dielectric constant of amorphous WO_3.[253] In case of the simulation with external bias, the applied voltage has been chosen to generate the same current density of 18 mA/cm^2 for devices incorporating air exposed and unexposed WO_3. Here, the quasi Fermi level moves very close to the ZnO conduction band for both, air exposed and unexposed WO_3, indicating that ZnO is n-conducting with a significant amount of free electrons. Therefore, the vast majority of charge carriers will be electrons leaking through to the WO_3 layer. After electrons gain energy at the potential drop at the interface from ZnO to WO_3, this will cause a high heat load concentrated at the junction and will probably lead to instability of the device at higher voltages. While defects, except for shallow donors, have not been included in determination of the quasi Fermi level shown here, the situation is assumed to be the same for defect-incorporating materials that are

intrinsic n-type, like ZnO and WO_3. The steep potential drop at the junction secures a short tunneling distance for electrons in interface-near ZnO defects, which makes tunnel extraction to the WO_3 conduction band feasible, as intended by the concept.

This device structure does not promise a satisfying efficiency because the majority of the current is suspected to leak through by conduction band to conduction band transport. Nevertheless, with the limited choice of materials with high work function in mind,[101] it enables us to study the influence of a reduced barrier height on hole creation within the defect states of ZnO. Tungsten trioxide has been used for similar investigations on ZnSe/CdSe/ZnS (core/inner shell/outer shell) quantum dots before, where it has been able to generate holes in the active material in contrast to another material of higher work function and thereby clarifying the role of the energetic band level offset for this system.[19] Additionally, the performance of ZnO nanoparticle LEDs incorporating a layer of intermixed WO_3 and ZnO nanoparticles has been shown to exhibit respectable device performance for white light emission, clearly visible to the naked eye.[97] In the following section, 6.2, the sputter deposition process is described and a characterization of the deposited tungsten trioxide layers is presented. In 6.3, the influences of tungsten trioxide layer thickness and oxygen content in the sputtering atmosphere on electrical and optical properties of the final device are discussed.

6.2. Sputtering of a thin WO_3 layer

WO_3 films are prepared by sputtering from a WO_3-target in an argon/oxygen atmosphere at different oxygen partial pressures, which are varied from 0 % to 100 % in

Oxygen partial pressure %	Massflow Argon sccm	Massflow Oxygen sccm
0	10	0
20	10	2.5
40	10	6.66
60	6.66	10
80	2.5	10
100	0	10

Table 6.1. – Mass flow of gases used for different oxygen partial pressures in sputtering atmosphere for WO_3 deposition.

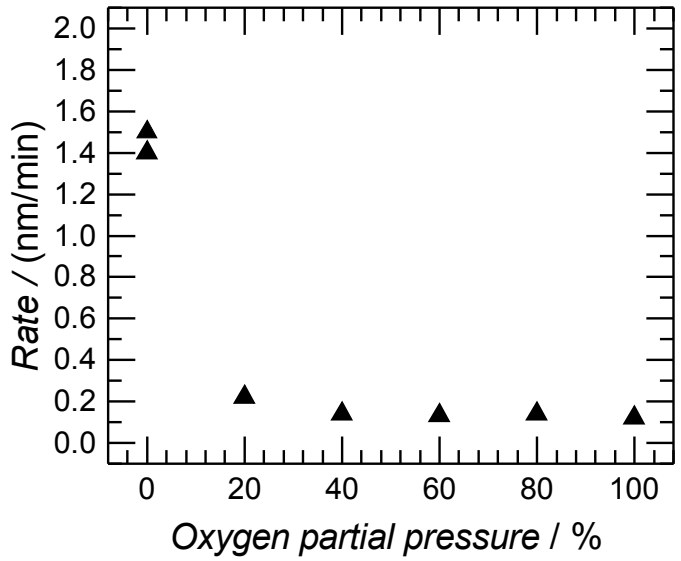

Figure 6.3. – WO_3 sputtering rate with respect to oxygen partial pressure.

steps of 20 %. The respective flow rates for each gas for the different partial pressures are shown in Tab. 6.1. The sputtering rate decreases for increasing oxygen partial pressure (Fig. 6.3) until a low rate of (0.13 ± 0.01) nm/s is reached at 40 %. After the oxygen partial pressure is increased further, the rate remains nearly constant. The main cause for this is the rather large scattering cross section of the oxygen molecule, which consists of two atoms, while the argon gas contains single atoms.[254] Therefore, sputtered ions have a reduced mean free path for acceleration and less ions hit the target with a sufficient momentum to separate molecules from the target, resulting in a lower deposition rate of WO_3.

Other parameters influencing the rate, among them the working pressure and the temperature of the sputtering target, are assumed to have a weaker impact under these conditions. The latter has been concluded from the following observations: Heating of the sputtering target in the process increases the sputtering rate, because the molecules need less additional energy to separate from the target. This can be observed in the first few minutes of pre-sputtering, when the rate increases. Heating of the target is favored in oxygen atmosphere, because the thermalization zone shifts

towards the target when the oxygen partial pressure is increased.[255] But because the sputtering rate is observed to be lower in contrast to the effect of heating, it is obviously super-compensated by the reduced mean free path in oxygen containing atmosphere, indicating that the mean free path has a stronger influence on the sputtering rate compared to the target temperature under the conditions of the presented experiment.

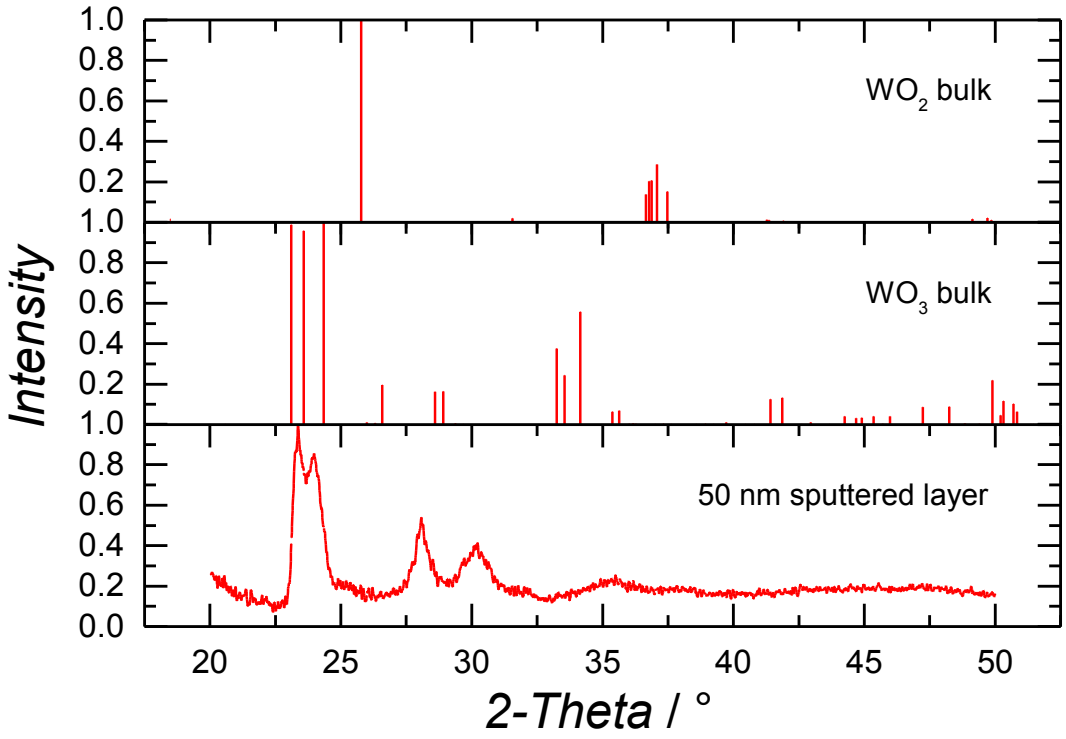

Figure 6.4. – Diffraction pattern of monoclinic, bulk WO_2, diffraction pattern of monoclinic, bulk WO_3, and diffraction pattern of a sputtered layer of WO_3, 50 nm thick. Bulk diffraction patterns are taken from [256].

In Fig. 6.4, the XRD diffraction pattern of a 50 nm sputtered layer is compared to the bulk reflexes of WO_2 and WO_3 in the monoclinic phase, which are the only configurations that are formed during deposition at room temperature.[257] The pattern of the sample is most similar to the one of monoclinic WO_3, therefore it is assumed that this type is the dominant one. The broad but clearly observable reflexes characterize a layer with a high amorphous share incorporating small crystalline grains. The average grain diameter has been calculated to be 16 nm using the Scherrer equa-

tion, which relates XRD peak broadening to the samples crystallite size.[258] While the reflexes of the sample below 25° match with the angle and relative intensity of the bulk ones, the reflexes that are observed on the bulk sample between 25° and 30° are shifted to higher angles by approximately 2°. This might be caused by strain or a superposition of grains of various sizes, with different grades of stoichiometry or with other tungsten oxide phases. At even higher angles, the reflexes are suppressed by the amorphous character of the sample.

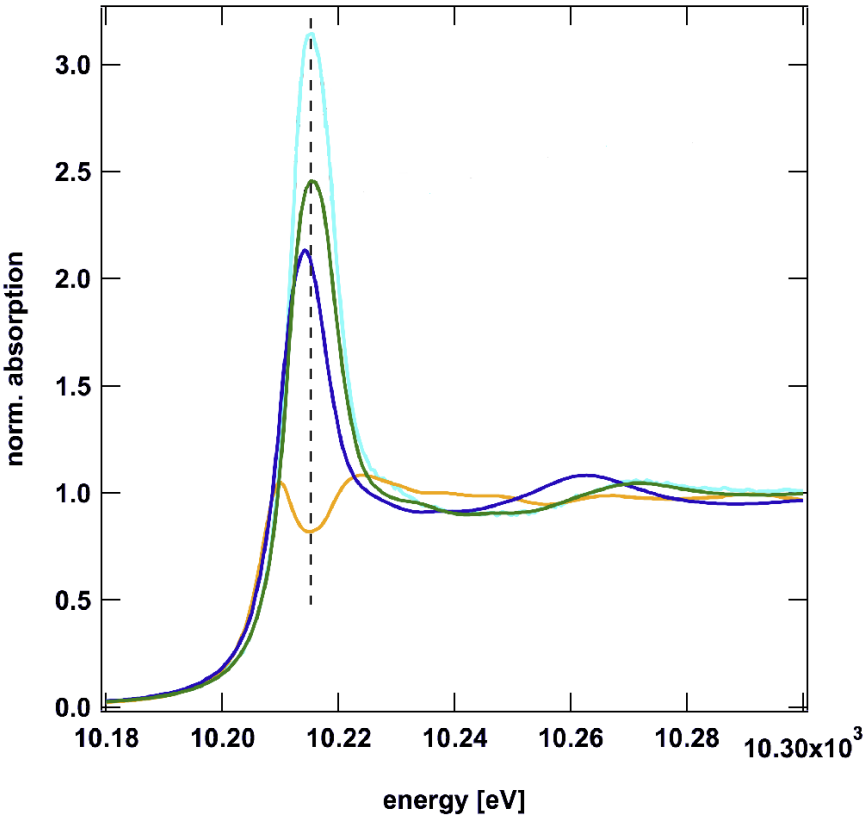

Figure 6.5. – WO_3 XANES spectra at the L_3 absorption edge of tungsten. Measurements were done on a sputtered layer with a thickness of 50 nm (cyan) and for reference purposes on a W foil (orange), and on WO_2 (blue) and WO_3 (green) powder pressed to pellets. The dashed line serves as guide to the eye and indicates the absorption maximum of tungsten in the sputtered layer. Measurements and graphic have been done by Alexander Kompch, NPPT, University of Duisburg-Essen.

The same sample is investigated by X-ray absorption near edge structure (XANES, Fig. 6.5). A W foil, WO_2 and WO_3 pellets are used as reference samples. The pellets

have been pressed from powders of 100 nm grain size. XANES reveals information about the energy levels of orbitals, that are very specific for every element and that are influenced by the oxidation state.[259] XANES is therefore an excellent way to examine the stoichiometric composition of the sample at the surface. The shown XANES spectra were taken at the L_3 edge of tungsten, that results from absorption at the $2p_{(J=3/2)}$ orbital.

The L_3 absorption peak of the sample matches with both, the WO_3 and W reference, closely, so that no clear identification can be given from this alone. The absorption at higher energy, in the area called the continuum, shows oscillations that are resulting from interaction of re-emitted photons after x-ray absorption.[259] The shape of these oscillations depends on the number and on the distance of adjacent atoms, which can be related to the lattice configuration.[259] The very good coinciding of the sample with the WO_3 reference implies a similar crystallographic configuration of both. It can be clearly distinguished from the W and WO_2 references, which is an additional indication, aside from the observations made by XRD, that the sample consists of tungsten trioxide.

The optical transmission of the sputtered WO_3 films is shown in Fig. 6.6 for layers of different thickness deposited on a pristine SiO_2-substrate, along with an inset that shows a picture of the samples. The transmission of the thin 2 nm and 5 nm layers is very high, above 97 % and 95 % in the spectral range from 380 nm (ZnO UV near band gap emission) to the end of the visible spectral range, respectively. The thicker layers both show a special but different behavior. Despite being ten times as thick, the 50 nm transmits more photons than the 5 nm layer between 354 nm and 415 nm, but shows a dip of the transmission in the visible range which is caused by interference. With an transmission above 93 % in the relevant spectral range, however, this layer is still considered to be suited as transparent injection layer for ZnO LEDs, along with the thinner 2 nm and 5 nm layers. The transmission of the 20 nm layer is significantly reduced above 325 nm compared to all other samples. This is an indication of a significantly higher defect concentration. Only the transmission of this sample, which is below 90 % for wavelengths smaller than 565 nm, is not regarded to be sufficient for application in a ZnO LED.

The bronze color of the 50 nm layer is an indication for a high concentration of reduced WO_3,[260] facilitated by the high specific surface of the thin film. The color of thin 2 nm and 5 nm samples is a pale yellow, which is generally an indication

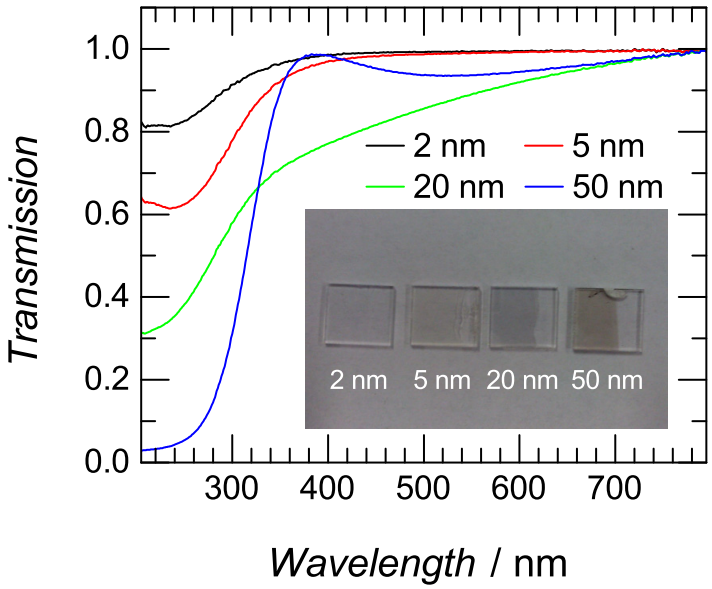

Figure 6.6. – Transmission of samples with different WO_3 layer thickness with respect to the wavelength. The inset shows a picture of the samples.

for stoichiometric WO_3.[260] In this case, however, it is likely that these layers are reduced like the 50 nm layer and only appear in a lighter color due to their small thickness. The 20 nm film looks very different, it appears gray. Gray WO_3 is considered to incorporate impurities.[261] Aside from W impurities and oxygen vacancies, these might be nitrogen impurities, as discussed below.

WO_3 is reported to be an indirect semiconductor with a bulk indirect bandgap in the range from 2.4 eV to 2.8 eV, which is about an electron volt below the bulk direct band gap at 3.5 eV.[262, 263] The indirect band gap of stoichiometric thin-film WO_3 is reported in the range from 2.9 eV to 3.4 eV,[19, 242, 264–266] about half an electron volt above the bulk value. Crystalline thin-film layers tend to exhibit a band gap at the lower end of the span and amorphous layers at the upper end.[264, 265] It has been reported, e.g., that the indirect band gap decreased from 3.2 eV to 2.9 eV after increasing the average nanocrystalline grain size from 9 nm to 50 nm by increasing the substrate temperature during sputtering from 100 °C to 500 °C.[266] This has been attributed to quantum confinement in the nanocrystalline grains. For comparison: The bulk exciton Bohr radius of WO_3 is about 13 nm.[267] The more a layer gets

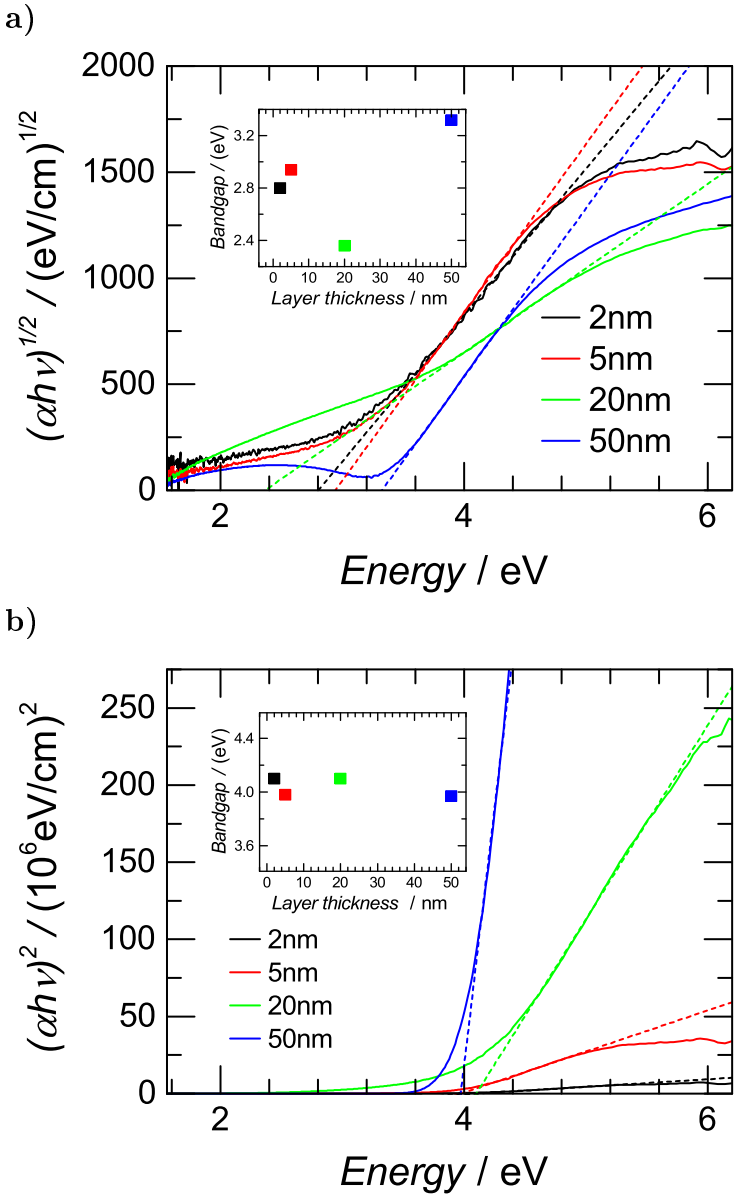

Figure 6.7. – Tauc plots of the absorption of WO_3 layers with a thickness of 2 nm, 5 nm, 20 nm and 50 nm, for (a) indirect and (b) direct transition. The dotted lines are fits to the linear part of the Tauc plots used to determine the band gap of the samples, which are shown in the respective figures inset in the same color as the corresponding Tauc plot.

amorphous, the smaller become the crystal grains, explaining why amorphous layers have the largest band gap.

Tauc plots[268] for determining the direct band gap are shown in Fig. 6.7a and

for determining the indirect bandgap in Fig. 6.7b. In this presentation, a quantity $(\alpha h\nu)^\eta$ is plotted against the photon energy $h\nu$, with the exponent η being dependent on the type of optical transition. Its value is 2 for a direct transition, and 0.5 for an indirect transition.[268] The intersection of a fit of the linear section of a Tauc plot with the energy axis reveals the materials direct/indirect band gap, respectively. The values for the band gaps evaluated are shown in the respective figures inset.

The determined direct band gap is almost constant for all samples at about 4.0 eV to 4.1 eV. This value is in agreement with a previous report on sputtered thin-film WO_3,[266] and is about half an electron volt above the bulk value, which is comparable to the indirect band gap increase observed for amorphous layers in literature and which might result from quantum confinement, as well. The Tauc indirect band gap is varying without showing a clear pattern regarding layer thickness. It is determined to be 2.8 eV (2 nm), 2.9 eV(5 nm), 2.36 eV (20 nm), and 3.3 eV (50 nm), respectively. The increased Tauc indirect band gap of the 50 nm film explains the high transparency of this layer in the near UV regime. In contrast, the Tauc indirect band gap of the 20 nm thick layer is especially small. While a contribution by improved layer crystallinity to a reduction of the indirect band gap is possible, it seems unlikely that neither the complete effect nor a major share of it can be explained this way here. A change of crystallite grain size would be expected to be noticeable in a reduction of the Tauc direct band gap, too, which has been determined to be constant. Furthermore, the indirect band gap of the 20 nm layer is well below the bulk crystal value, which is therefore impossible to be explained by increased crystallinity. The thin 2 nm and 5 nm layers are determined to have a band gap close to the bulk crystal value, which would correlate to an increased crystallinity observed at a substrate temperature of 500 °C during sputtering before.[266] Because both layers have been sputtered at room temperature, this is at least doubtful, even if the unregulated substrate temperature has been increased during deposition as a side effect of the sputtering process. It seems more likely, that the reduced Tauc indirect band gaps of the 2 nm, 5 nm and 20 nm layers are caused by defects, and that the 20 nm layer with the lowest Tauc indirect band gap might bear a particular high concentration of them. A reduced Tauc indirect band gap of WO_3 has been related to understoichiometry of WO_3,[261] and nitrogen impurities in literature.[269–271]

6.3. WO_3 / ZnO LED

6.3.1. Processing of devices

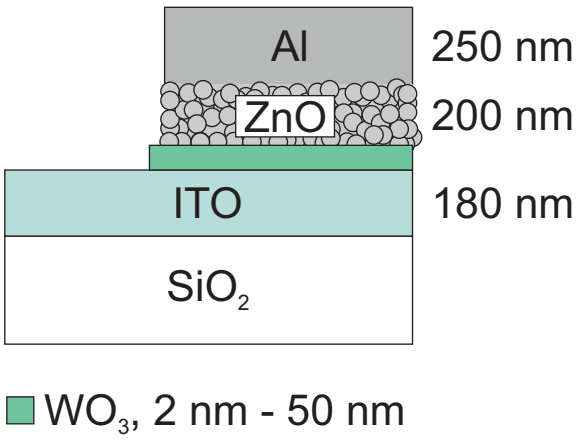

Figure 6.8. – Schematic of the WO_3/ZnO LED layer design. The length specifications refer to the respective layer thickness.

LEDs are prepared on the basis of the presented WO_3 coated ITO substrates. A schematic of the final devices is presented in Fig. 6.8. ITO substrates from Philips are used which have a smooth surface with a roughness below 1 nm and a very low sheet resistance of about 8 Ω/□ for current spreading and contacting the p-side (WO_3) of the device. A small stripe of about 3 mm at one edge of the sample was protected by a foil from being coated in the following process, which will be used to contact the ITO. The ZnO nanoparticle layer on top of the sputtered WO_3 layer is prepared by spin-coating at 4000 rpm from a dispersion presented in chapter 5. The details of the spin-coating process can be found in 4.3 with the exception that a dispersion drop volume of only 15 µl is used to produce these samples and that we measured a resulting thickness of the ZnO nanoparticle layer of about 200 nm. Finally, aluminum is deposited on top of the nanoparticle layer to serve as cathode by ebeam evaporation at a growth rate of 1 nm/s through a shadow mask until the final thickness of 250 nm is accomplished.

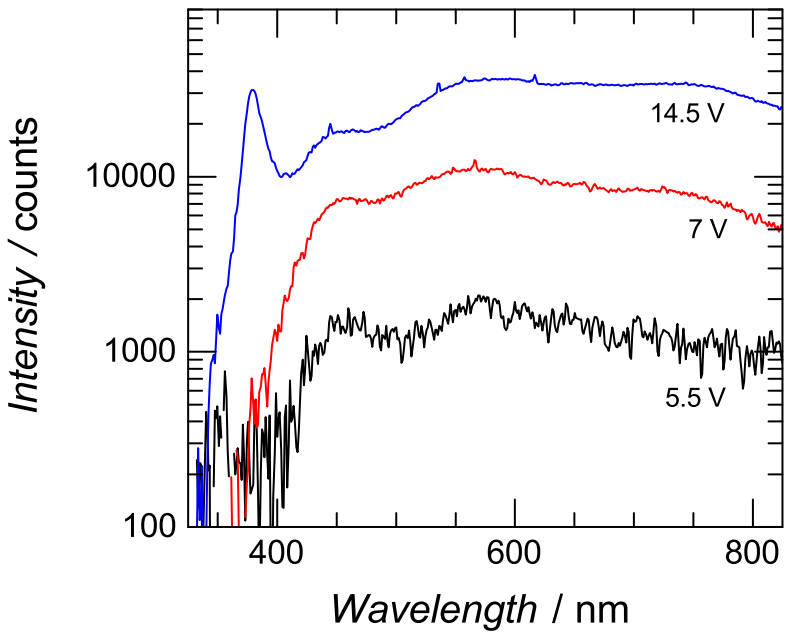

Figure 6.9. – Logarithmic plot of electroluminescence intensity of a WO_3/ZnO LED in dependence of the wavelength for applied voltages of 5.5 V, 7 V and 14.5 V. The WO_3 layer has been sputtered in pure argon atmosphere and is 5 nm thick.

6.3.2. Light-emission characteristics

The electroluminescence spectra recorded from a WO_3/ZnO LED with a 5 nm WO_3 layer that has been sputtered in pure argon atmosphere are shown in Fig. 6.9. They have been taken at 5.5 V (low voltage), 7 V (medium voltage) and 14.5 V (high voltage). At low driving voltages close to the detection limit, we see a broad emission spectrum that covers the entire visible range, but no UV emission. The emission maxima are around 450 nm to 460 nm (blue), 550 nm to 570 nm (green) and 740 nm to 760 nm (red). At medium voltages the emission intensity increases, but the shape of the emission spectrum remains almost constant with very weak UV emission. At high voltages, green to red is preferred over blue emission, presumably by current annealing of less stable blue emitting defects.[204] UV emission is observable only at high voltages, where the device is already unstable. If we recall the photoluminescence spectrum of the ZnO nanoparticles presented in Fig. 5.1, the relative emission intensity distribution of the different spectral ranges is surprising. Under laser excitation, the green luminescence is one magnitude, the red luminescence even

1.5 magnitudes less intense compared to the blue emission, yet the electrical devices show comparable intensities in all three spectral ranges at low to medium voltages. UV emission is missing completely, while it is even stronger in PL than blue emission. It has to be noted that the center emission wavelengths of the green and red emission are identical in PL and EL, while they differ for the blue emission. In PL, the intensity maximum has been positioned at a shorter wavelength of 425 nm.

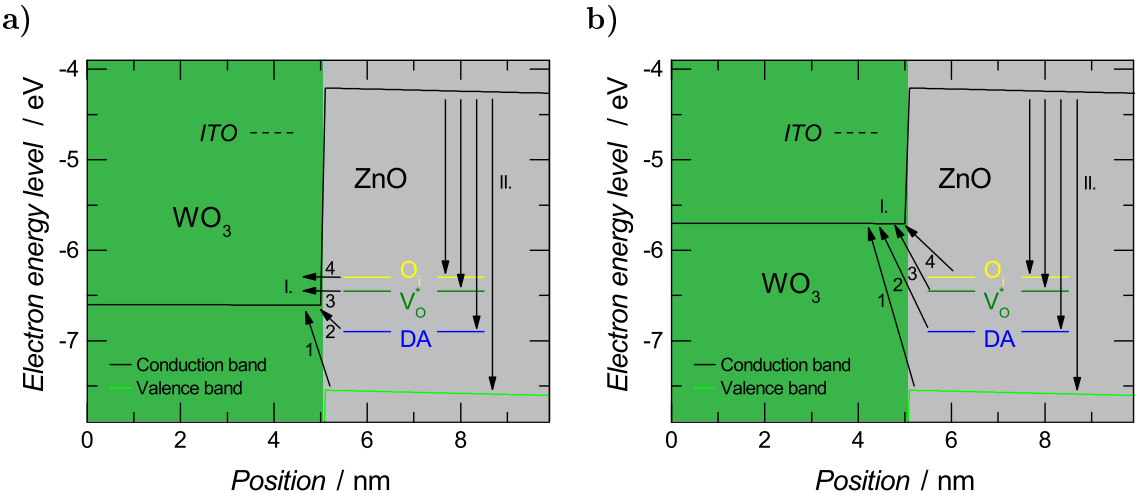

Figure 6.10. – Sketch of assumed electron extraction transitions at the WO_3/ZnO junction (I.) and suggested subsequent radiative recombination with an electron from the ZnO band gap or a shallow donor state (II.). ZnO defect levels[203, 221] have been set into the band gap simulations already shown in (a) Fig. 6.2c for the unexposed WO_3/ZnO junction and (b) Fig. 6.2d for the air exposed WO_3/ZnO junction. O_i: oxygen interstitial, $V_O^{\bullet}$: oxygen vacancy, and DA: deep acceptor level. For reference, the ITO level is been indicated by a dashed line.

The suggested electron extraction transitions are presented in Fig. 6.10: from ZnO valence band (1, creating holes involved in UV emission), a deep acceptor level DA (2, blue), singly ionized oxygen vacancies $V_O^{\bullet}$ (3, green), and oxygen interstitials O_i (4, yellow/orange/red, depending on the electron level involved). In case of unexposed WO_3, extractions from $V_O^{\bullet}$ and O_i are spontaneous, while extractions from the deep acceptor and the ZnO valence band need additional energy, about 0.3 eV and 0.9 eV, respectively. In case of air exposed WO_3, all extraction transitions need additional energy (Fig. 6.10b; approximate additional energy required: 0.6 eV (O_i)/0.7 eV ($V_O^{\bullet}$)/1.2 eV (DA)/1.8 eV (ZnO valence band)). For reference, the ITO work function

is indicated by dashed lines in Fig. 6.10a and Fig. 6.10b, showing the much lower energy barrier for electron extraction by WO_3.

Following the energy level alignment, the different shapes of the electroluminescence spectra compared to the photoluminescence spectrum (Fig. 5.1) are explained as follows. Green to red emission is assumed to be pronounced by a smaller barrier height for electron extraction. On the other hand, UV and blue emission involving holes in the ZnO valence band are suppressed at medium voltage levels, because the barrier is too large. Similar observations regarding increased barrier height have been made by Wood et al.,[19] which have built a LED using ZnCdS/ZnS quantum dots as active material. They have tried to create holes in this material by hole injection from NiO, which valence band is 1.6 eV higher, and by electron extraction with WO_3, which conduction band is only 0.7 eV higher. The first device did not show any EL, while the second one did. While the majority of blue emission in PL is attributed to transitions from zinc interstitials to the ZnO valence band, the remaining blue emission in EL is assumed originate from transitions from zinc interstitials to a deep acceptor level, which might be identified as zinc vacancy (cf. chapter 3.3.2). The donor-acceptor transition emits at a higher wavelength, which correlates with the observed redshift of the peak wavelength in the blue spectral range between PL and EL. The concentration of zinc vacancies is expected to be low, because the particles have been made under zinc rich conditions. With blue emission involving the ZnO valence band being suppressed, this leads to a significantly reduced intensity of blue emission in EL.

The UV intensity that has been observed for the simple ITO/ZnO device (cf. Fig. 5.1), is quite surprising if compared to the WO_3 device. Despite a higher injection barrier of ITO to the ZnO valence band at the anode side of about an electron volt, UV emission of the simple device is more intense. Without another electrical resistive support layer, this may be related to a concentration of the voltage drop within the particle layer and, e.g., favoring a recombination mechanism as depicted in Fig. 2.3b.

Figure 6.11 shows the intensity distribution over the contacted area for a circle shaped contact with a diameter of 3 mm. The emission is distributed over the full area with 2000 counts to 6000 counts on the majority of pixels. This is a proof for the good current spreading by the underlying ITO layer, little spatial variation of the quantum yield of the ZnO nanoparticle layer and little spatial variation of the resistance of all layers. The intensity increases slightly towards the center and the

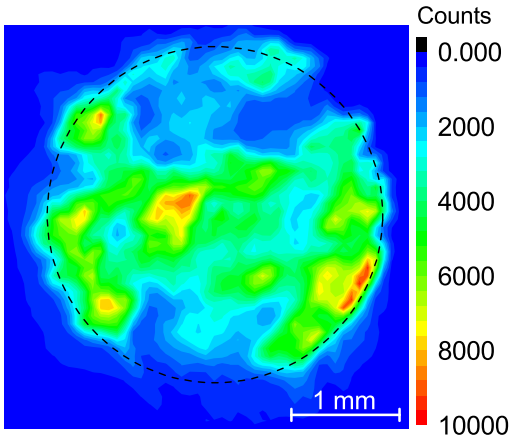

Figure 6.11. – 2D contour plot of the intensity distribution at 10.5 V for a device with 5 nm WO_3 layer sputtered in pure argon atmosphere. The dashed circular line indicates the area of the aluminum top contact. The ITO-anode has been contacted on the left-hand side outside the image according to the contact setup shown in Fig. 4.1a.

edge of the contact.

The IV-characteristic for devices with a WO_3 electron extraction layer and a reference device without is presented in Fig. 6.12. With increasing layer thickness (Fig. 6.12a), an increase of onset voltage[1] is observed with larger offsets between the reference, the devices with the 2 nm, 5 nm and 20 nm films and the device with the 50 nm film. An increased current by a factor of up to 14 is measured for the device with a 5 nm layer at voltages at 5.5 V and above, while a reduced current is detected for the devices with the thicker 20 nm and 50 nm layers. While the device with the 2 nm layer exhibits a higher onset voltage, it shows comparable current densities to the reference at voltages at 6 V and above. Fig. 6.12b shows current-voltage characteristics of the devices with different oxygen content in the oxygen/argon sputtering atmosphere. A reduced onset voltage is observed for the layer sputtered in 20 % oxygen compared to the one sputtered without, which is comparable to the onset voltage of the reference without WO_3 layer. At low voltages, the current density of the device with the layer sputtered in 20 % oxygen atmosphere is increased up to 10 times compared to the reference, while it is below the layer sputtered without oxy-

[1] The lowest voltage, which leads to a current above 1 mA/cm^2, will be regarded as onset voltage for discussion here.

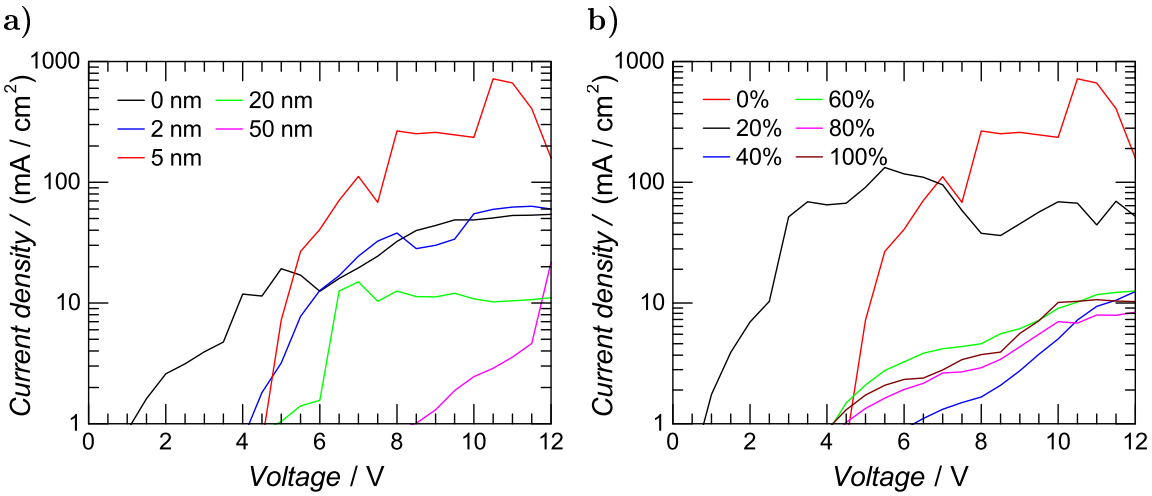

Figure 6.12. – Current / voltage characteristics of LEDs (a) with different WO_3 layer thickness sputtered in pure argon atmosphere and a reference device without WO_3 layer and (b) 5 nm WO_3 layer thickness sputtered at different oxygen concentrations.

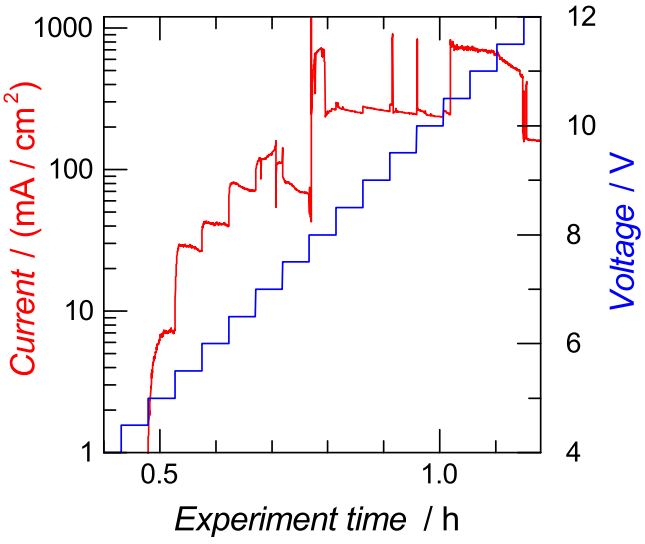

Figure 6.13. – Time-dependent current flow (red) and driving voltage (blue) of an experiment with a LED with 5 nm WO_3 layer.

gen at voltages of 7 V and above. With an oxygen concentration of 40 % and more, devices show a decrease in conductivity. This is attributed to less oxygen vacancies which act as donors, and therefore a reduction of charge carriers. In contrast, the layer sputtered in 20 % oxygen atmosphere may have been improved by better stoichiometry, which leads to a higher crystallinity and, e.g., carrier mobility, which may have overcompensated the loss of charge carriers.

Insight into the stability properties of devices with WO_3 layer is derived from a time-resolved current/voltage characteristic of a LED with 5 nm WO_3 layer. Fig. 6.13 shows current flow (red) and driving voltage (blue) as a function of experiment time. The current has been measured every second, while the voltage has been increased from 0 V to 20 V in steps of 0.5 V and has been kept at each voltage level for about three minutes. The resulting curve has been divided into six areas with similar properties. While the exact progress of degradation differs for every WO_3/ZnO LED due to the nature of an instability process, some observations have been made repeatedly:

1. The onset of visible emission is observed close to the onset of current. At these voltage levels, no serious degradation is observed.

2. As long as the device current is stable over time at a certain voltage level, its magnitude increases with increasing voltage. At some point, in Fig. 6.13 at around 7 V after 0.7 h, current becomes unstable. After increasing the voltage, current is initially increased, but often immediately starts to decrease again. From this observation, it is assumed, that the current of these devices is limited by stability.

3. Rapid current decreases often occur coupled with changed emission spectra.

4. UV emission is observed at high voltages only, where the device is already unstable.

Fig. 6.14 shows the maximum intensity observed for the WO_3/ZnO devices. The intensity was determined by a comparative method by capturing an image with a CCD camera, summing up all the counts for every pixel and comparing the result to the value determined for a reference with known intensity in the same way:

$$P_{sample} = \frac{Counts_{sample}}{Counts_{reference}} P_{reference}. \tag{6.1}$$

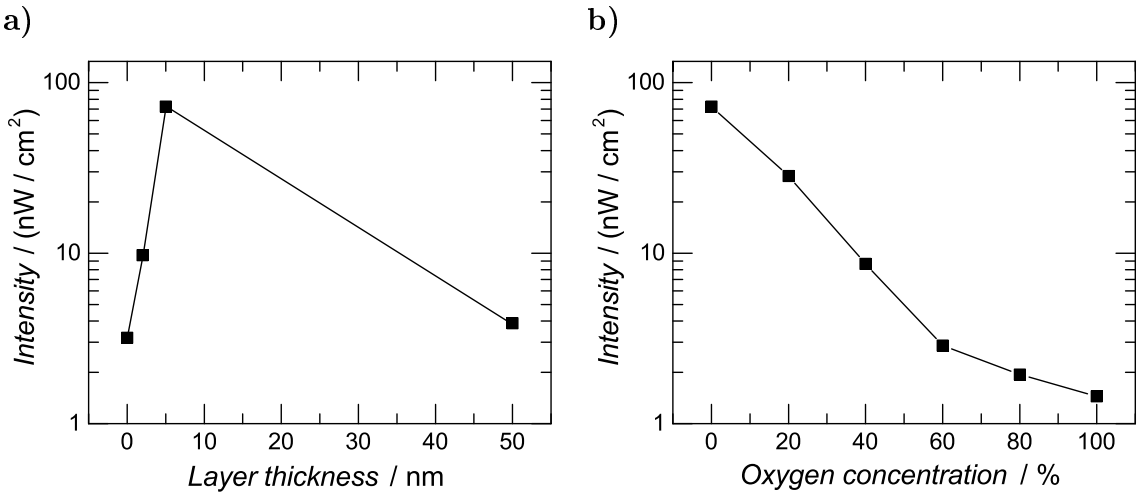

Figure 6.14. – Maximum total emission intensity of LEDs (a) with different WO_3 layer thickness sputtered in pure argon atmosphere and a reference device without WO_3 layer and (b) 5 nm WO_3 layer thickness sputtered at different oxygen concentrations.

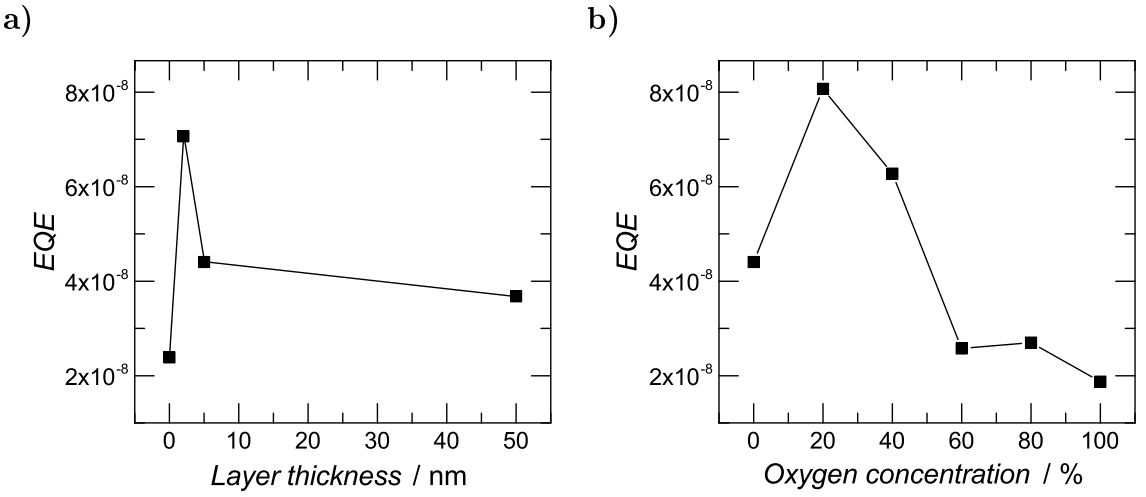

Figure 6.15. – External quantum efficiency of LEDs at the voltage showing their maximum intensity (cf. Fig. A.4), (a) with different WO_3 layer thickness sputtered in pure argon atmosphere and a reference device without WO_3 layer and (b) 5 nm WO_3 layer thickness sputtered at different oxygen concentrations.

While the maximum intensity already increases with a thin 2 nm layer, the effect is significantly enhanced with a 5 nm WO_3 layer sputtered without oxygen. For a 50 nm layer, the maximum intensity decreases again to a value comparable to the one of the reference. The emission of the device incorporating a 20 nm layer has been much lower (0.63 nW/cm^2, not shown here), which is attributed to a high defect concentration of the layer as concluded from the absorption measurement before. With increasing oxygen content in the sputtering atmosphere (Fig. 6.14b), the maximum intensity decreases. While there is definitely a large increase in maximum intensity for the device with a 5 nm layer sputtered in pure argon, the absolute value of 73 nW/cm^2 is still rather low. Because the current flow is within the typical mA/cm^2 scale for a LED, the low intensity is caused by a low efficiency, which will be discussed in the next paragraph.

The external quantum efficiency of the WO_3/ZnO LEDs is determined analogue to the emission intensity by

$$EQE_{sample} = \frac{Counts_{sample}/Current_{sample}}{Counts_{reference}/Current_{reference}} EQE_{reference} \tag{6.2}$$

using the maximum intensity and the respective current flow of each sample. The results are presented in Fig. 6.15. A general increase of the EQE of devices with a WO_3 layer is observed. Regarding layer thickness, the highest increase is detected for the thinnest layer, and the EQE is being reduced again with increasing layer thickness. Regarding oxygen content, a further increase could be observed at low oxygen contents of 20 % and 40 %. The highest value of the EQE has been obtained for a 5 nm layer sputtered in 20 % oxygen (8.1×10^{-8}), while the EQE decreases if the oxygen content is increased further.

Nevertheless, even the maximum value of 8.1×10^{-8} is still rather low. With the out-coupling efficiency being in the order of 10 % (cf. chapter 2.4.3) and the quantum yield of the ZnO nanoparticle being 2.3×10^{-3}, both factors together are responsible for about four magnitudes missing. The others are lost due to the low injection efficiency, which is estimated to be about 3.4×10^{-4} and is limited by two effects. We can expect the majority of electrons to travel from the ZnO conduction band to the WO_3 conduction band. As there is no electron blocking layer incorporated in this simple design, both materials are n-conducting, and there is a high density of states in the band levels, this is clearly the preferred route and all of the electrons

moving this way do not recombine radiatively.

7. Hole injection with NiO

7.1. Concept

A major weakness of the WO_3/ZnO device concept presented in the previous chapter is the missing electron barrier, which results in low efficiencies from electron leakage. By replacing WO_3 with intrinsic p-doped NiO with low electron affinity (Fig. 7.1), electron blocking can be implemented. In inorganic quantum dot LEDs, NiO has first been studied as combined hole injection layer and electron blocking layer for cadmium based quantum dot devices that showed high brightness of up to 1950 cd/m^2.[14] The initial high emission threshold voltage has been reduced to 2 V for 1.94 eV emission.[272] NiO is therefore proven to be an hole injection material of interest, even as the efficiencies of the devices still need to be improved.[14, 272] ZnO LEDs using a NiO hole injection/electron blocking layer have also been reported. Orange emission (670 nm) has been detected at a p-Si/NiO/ZnO device with a threshold of about 5 V.[86] Recently, violet emission (404 nm) has been detected at about 4.8 V.[87] UV emission from these devices is observed at higher voltages. Combined NBE emission close to the UV (385 nm) and green emission (570 nm) have been observed for ZnO nanowires with a threshold of 7 V[88]. A similar result from another ZnO nanowire device was obtained and true UV emission (380 nm) and green emission (500 nm) at a very high voltage of 20 V have been presented.[89] Pure ZnO NBE emission at 371 nm has been reported from n-GaN/ZnO/i-$Mg_{1-x}Zn_xO$/NiO LED at a very low threshold voltage of 2.5 V.[90]

The NiO/ZnO electron interface barrier has been measured to be 2.93 eV for a sample consisting of a NiO layer deposited by electron beam evaporation and subsequent growth of a ZnO layer by plasma-assisted molecular beam epitaxy.[273] Yang et al. report a much lower conduction band offset of 1.8 eV for sputtered NiO on a sputtered ZnO layer and attribute the difference to the previous report to the switched growth

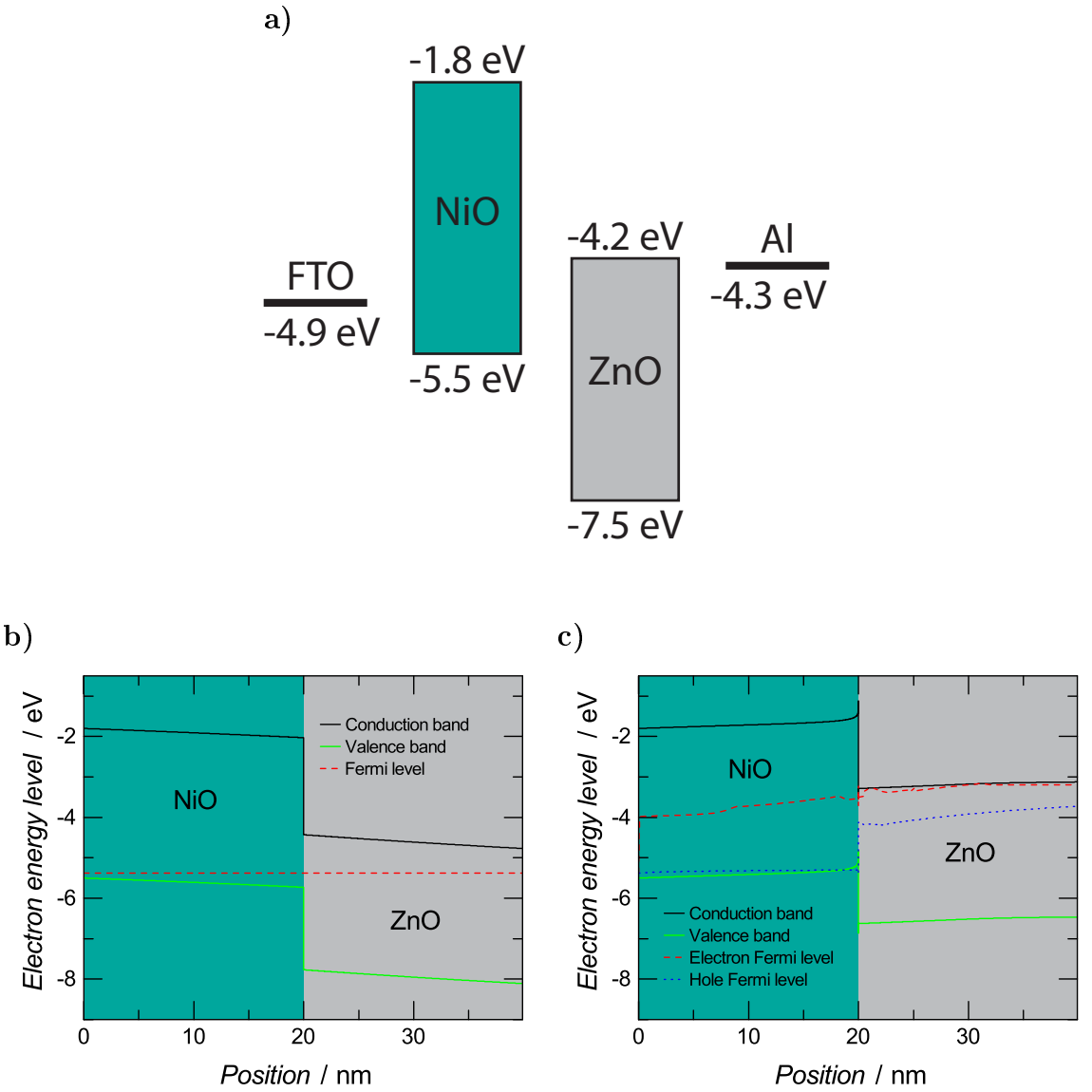

Figure 7.1. – (a) Basic NiO/ZnO band level diagram in vacuum without contact of the materials to each other, showing the electron energy with respect to the vacuum level.[14, 125, 234, 236, 237] (b) Simulation of conduction band level, valence band level, and Fermi level of NiO/ZnO structures without external bias, and (c) band levels, quasi electron and quasi hole Fermi levels at external bias of 2.2 V. NiO layer has been filled with green-blue and ZnO layer with gray in all figures allowing for quick comparison. For more details regarding the simulation cf. Appendix A.2.

order and the influence of interface strain.[274] For a nanoparticle device, however, interface strain may be of minor importance due to the low interaction between a NiO layer and post-growth deposited ZnO nanoparticles. Therefore, the barrier is estimated for these devices by taking the energy offset of the vacuum levels of the materials into account. The conduction band edge of amorphous, sputtered NiO has been determined to be at $-1.8\,\mathrm{eV}$ (electron vacuum level, Fig.7.1a),[14] which leads to an estimated electron barrier of $2.4\,\mathrm{eV}$ for an unbiased nanoparticle device (Fig. 7.1b).

After an external voltage of $2.2\,\mathrm{V}$ is applied (Fig. 7.1c), thin barrier spikes at the interface and a reduction of the offsets of the band levels some nanometers away from the junction are observed due to band bending. Such a behavior could lead to a greatly increased tunneling current with increased voltage. A similar shape of the band diagram of a biased NiO/ZnO junction has been published in reference [89]. Nevertheless, the band diagram shown in Fig. 7.1c is of limited validity, because the simulation of current did not converge and the shape of the band diagram varies strongly with different discretization of the spatial grid. The grid positions chosen in the presented simulation are summed up in Tab. A.3. Therefore, this band diagram will not be employed in further discussions.

7.2. NiO/ZnO LED

7.2.1. Processing of devices

The NiO/ZnO devices to be presented here (7.2a) are prepared from commercial FTO substrates from DyeSol with a sheet resistance of $8\,\Omega/\square$, that is used as base current spreading layer. It has a granular surface with a roughness of about $17\,\mathrm{nm}$ (7.2b). A small stripe of $2\,\mathrm{mm}$ to $3\,\mathrm{mm}$, which is designated to serve as p-contact, has been covered with tape to prevent any coating from the following process steps. A $20\,\mathrm{nm}$ thin NiO layer is then deposited by sputtering on top of the FTO, followed by spin-coating of the ZnO nanoparticle layer at $4000\,\mathrm{rpm}$ from a dispersion presented in chapter 5. The details of the spin-coating process can be found in chapter 4.3. A thickness of the ZnO nanoparticle layer of about $400\,\mathrm{nm}$ is measured. Finally, aluminum is deposited on top of the nanoparticle layer to serve as n-contact by ebeam evaporation at a growth rate of $1\,\mathrm{nm/s}$ through a shadow mask until the final

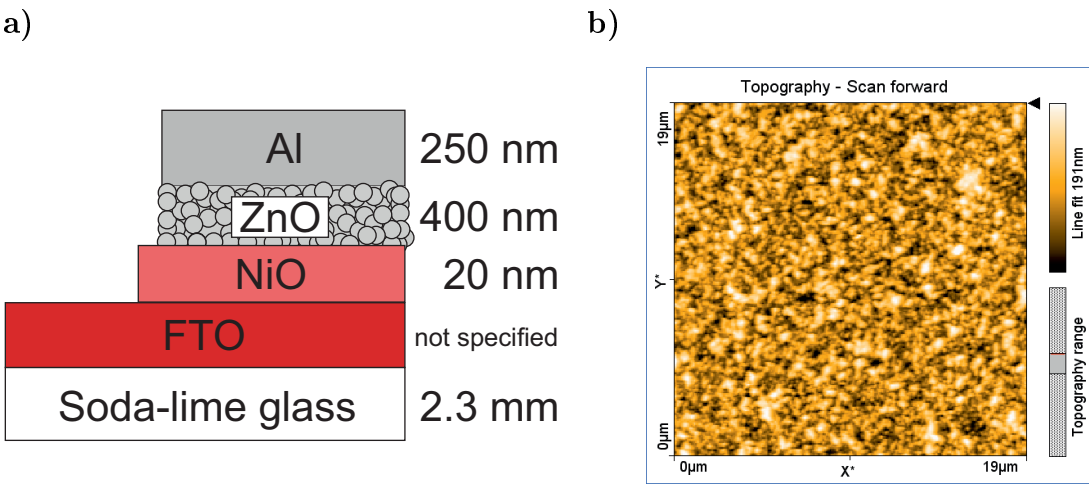

Figure 7.2. – (a) Schematic of NiO/ZnO LED layer design. The length specifications refer to the respective layer thickness. (b) AFM topography scan of the FTO surface.

thickness of 250 nm is accomplished.

7.2.2. Light-emission characteristics

Fig. 7.3 shows the measured electroluminescence spectra of the NiO/ZnO LED for different applied forward voltages ranging from 5.5 V to 11 V. A broad emission covering the entire visible spectrum is observed at all voltage levels. It is centered in the green area around 550 nm with additional maxima around 440 nm in the blue area and 710 nm in the red area. While the intensity increases with increasing voltage, no remarkable shift in relative intensity between emission centers in the visible range is detected. At medium voltage levels of 8.5 V to 10.5 V, only a low intensity shoulder is observed, but its relative intensity increases with voltage. This becomes especially obvious at 11 V, where the UV emission intensity increases strongly and a distinct peak is observed at 382 nm. The observed threshold voltages of visible and UV emission, 5.5 V and 11 V, are in reasonable agreement to the values reported in literature (chapter 7.1).

Compared with the photoluminescence spectrum of the ZnO nanoparticles, a clear pronouncing of green to red emitting defect states is obvious. While in PL green emission is one magnitude and red emission two magnitudes less intense compared to blue emission, intensities of all three are comparable under electrical excitation,

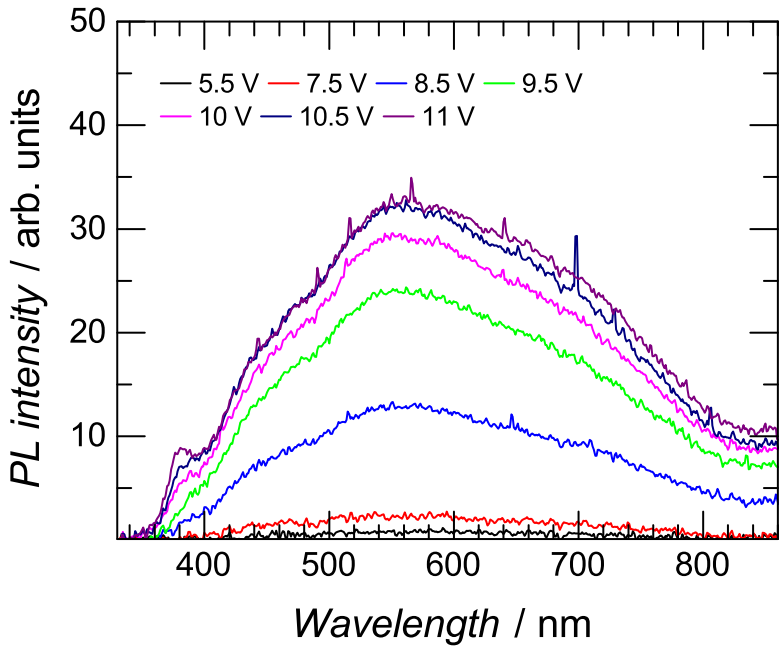

Figure 7.3. – Electroluminescence intensity of the NiO/ZnO LED in dependence of the wavelength for applied voltages of 5.5 V, 7.5 V, 8.5 V, 9.5 V, 10 V, 10.5 V and 11 V.

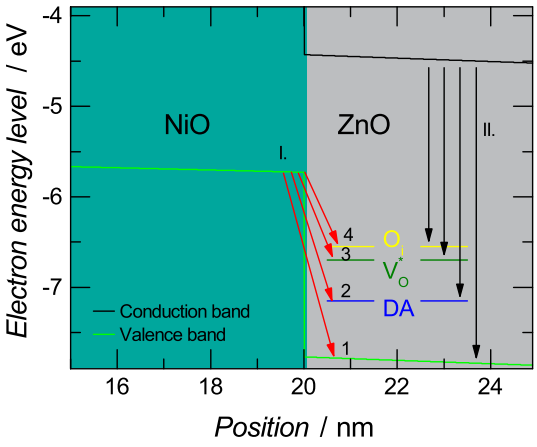

Figure 7.4. – Sketch of assumed hole injection transitions at the NiO/ZnO junction (I.) and subsequent radiative recombination with an electron from the ZnO band gap or a shallow donor state (II.). Approximate ZnO defect levels have been set into the band gap simulation already shown in Fig. 7.1b. O_i: oxygen interstitial, $V_O^{\bullet}$: oxygen vacancy, and DA: deep acceptor level.

similar to simple ITO and WO_3 devices discussed before. UV emission, which is the strongest recombination process for PL, is clearly suppressed in EL giving an indication of inefficient hole injection into the ZnO valence band. The observed defect-related electroluminescence is attributed to direct hole injection into these defect states (Fig. 7.4). The reduced share of emission at lower wavelengths compared to PL is attributed to an increasing hole injection barrier, similar as it has been discussed for electron extraction in WO_3/ZnO LEDs (chapter 6.3).

Fig. 7.5a shows the IV characteristic of the FTO/NiO/ZnO/Al LED and a reference (ITO/ZnO/Al) made of the same ZnO nanoparticles. While the reference exhibits a linear, ohmic behavior, the device with NiO follows a super-linear characteristic with a turn-on voltage of 5 V. This is attributed to the rather large band offsets between the two materials at the interface, that cause a need for a higher applied voltage for carrier injection. For both devices, we see an increase in current with increasing voltage only up to a certain point at 7 V, and a decrease after that point. This might be related to degeneration of the device by the applied heat load at the interfaces resulting from the fact that most of the energy introduced into the device is converted to heat. Thereby, e.g., zinc interstitial donors in ZnO might be annealed, resulting in reduction of free charge carrier density and conductivity of the ZnO nanoparticle layer. In Fig. 7.5b, the current and voltage is depicted over time. We observe an improved stability of the device with NiO layer until the critical voltage level of 7 V. While we see a degradation of the current flow of the reference device after every increase in voltage, this is not observed for the NiO LED, which current increases over time at voltage levels between 5 V to 7 V. The increased stability might be caused by electron blocking of the NiO layer and therefore preventing short cuts, as well as by the additional resistance added with the NiO layer. At voltages above 7 V, however, both devices degrade likewise, and the degradation speed increases with increased voltage.

The electroluminescence intensity is shown in Fig. 7.5c. In case of the reference, we observe an increase of the emission intensity with voltage with an emission detection threshold of about 2.5 V. After 5.5 V the emission intensity stays almost constant with regard to voltage. With incorporation of a NiO layer the emission detection threshold is increased to 4.5 V, and the electroluminescence intensity is increased up to a voltage of 10.5 V. At this voltage, the emission intensity reaches its maximum, which is about three times as high as the intensity of the reference device at the

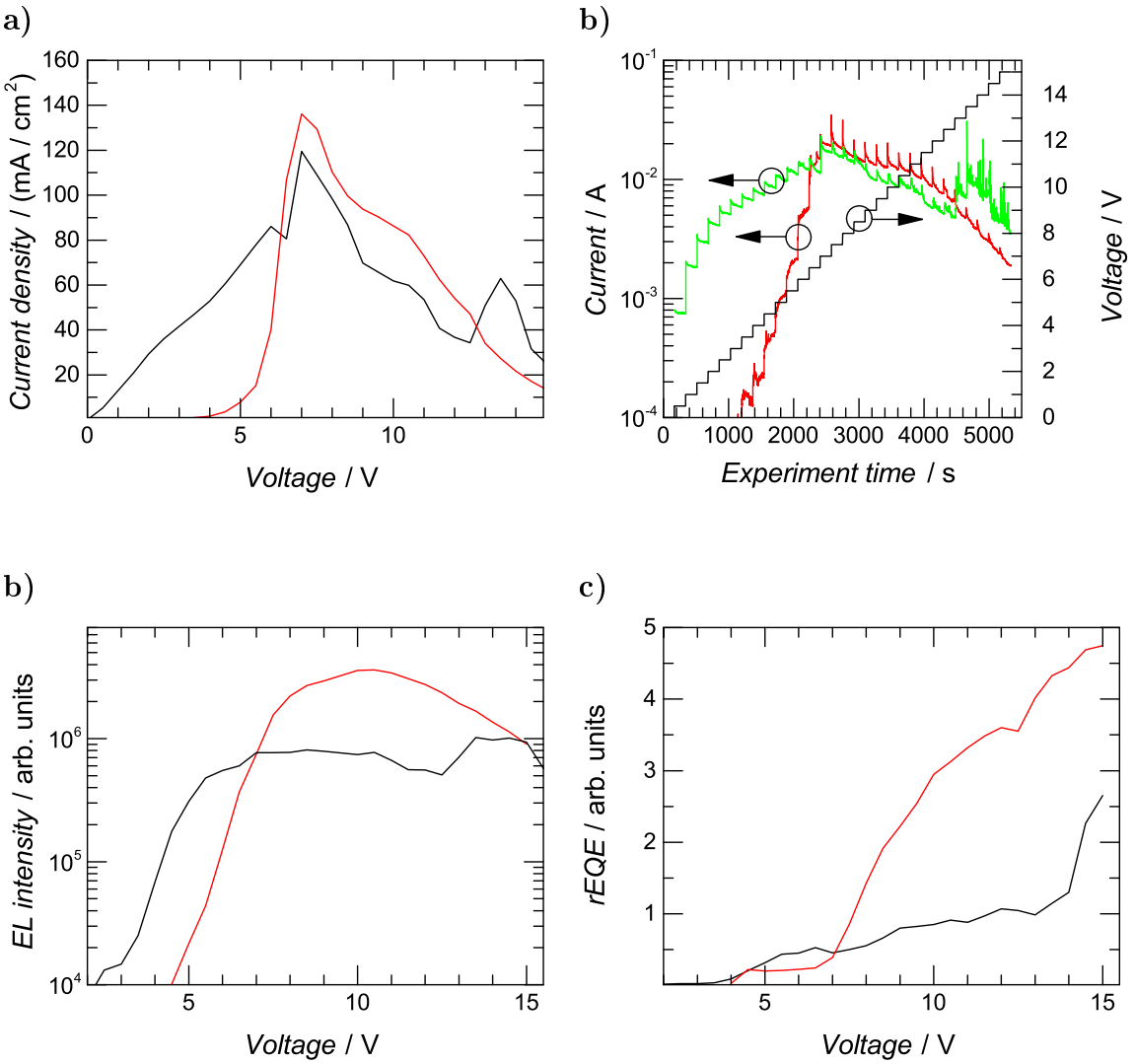

Figure 7.5. – (a) Current / voltage characteristic as a function of voltage of the FTO/NiO/ZnO/Al LED (red) and an ITO/ZnO/Al reference (black). (b) Voltage (black) and current of the NiO/ZnO LED (red) and the reference on an ITO substrate (green) as a function of time. (c) Electroluminescence intensity and (d) relative external quantum efficiency (rEQE, cf. text) as a function of voltage of the FTO/NiO/ZnO/Al LED (red) and an ITO/ZnO/Al reference (black).

same voltage. If the voltage is increased further, the emission intensity declines, as possibly the decrease of current becomes dominant. A measure for the relative external quantum efficiency of the NiO LED as a function of the voltage level is shown in Fig. 7.5d. It has been calculated by dividing the total intensity recorded on the CCD by the respective current flow. Compared with the efficiency of the reference on an ITO substrate, the efficiency of the NiO device is lower until 7.5 V, where it increases rapidly. At a voltage of about 12 V, the efficiency of the NiO device is about three times as high. While the electron blocking characteristic of NiO might have led to this increase, it is assumed that a stronger increase has been prevented by the still rather large valence band offset between NiO and ZnO. In the next chapter, GaN/ZnO devices will be investigated with a much better fitting of valence band levels.

8. Hole injection with GaN

8.1. Concept

The external quantum efficiency of the LEDs presented in previous chapters is far away from being at a level required for technical application. The very low valence band edge (7.5 eV below electron vacuum level) of ZnO is suspected to be the main reason for this: despite implementing the support layers, charge carriers still have to face injection barriers of more than an electron volt at the ZnO interface. Therefore, the electrical driven devices experience a great difficulty when injecting holes/extracting electrons into/from the ZnO valence band and obtaining efficient ultraviolet (UV) emission from these material concepts might be very difficult. The choice of p-doped materials with a valence band edge that fits to the one of ZnO is very limited.[101] Among them is GaN, a material with well-established p-doping processes that is used in today's LEDs and laser-diode commercial products and has already been extensively studied in combination with ZnO.[27–85] The application of this material in a ZnO LED concept will allow for studying the effect of a fitting valence band level. The valence band and conduction band levels of GaN and ZnO are shown in Fig. 8.1 along with the work functions of a Au/Ni p- and an Al n-contact. Au/Ni has been reported various times to form ohmic contacts to p-GaN.[134–137]

Three different emission patterns have been observed with GaN/ZnO heterojunction LEDs: seldom UV centered emission below 380 nm,[27–33] more often blue centered emission around 400 nm,[34–72] and broad visible emission often centered in the green-yellow spectral range around 550 nm to 600 nm.[73–85] A clear identification of the emitting layer is often very difficult because both materials show band gap or defect luminescence in all of these spectral ranges.[38, 73, 147]

Traditionally, while visible emission has been detected at low voltage around 3.5 V to 5 V,[44, 48, 50, 53, 55–59, 67], UV emission from GaN/ZnO devices have had a

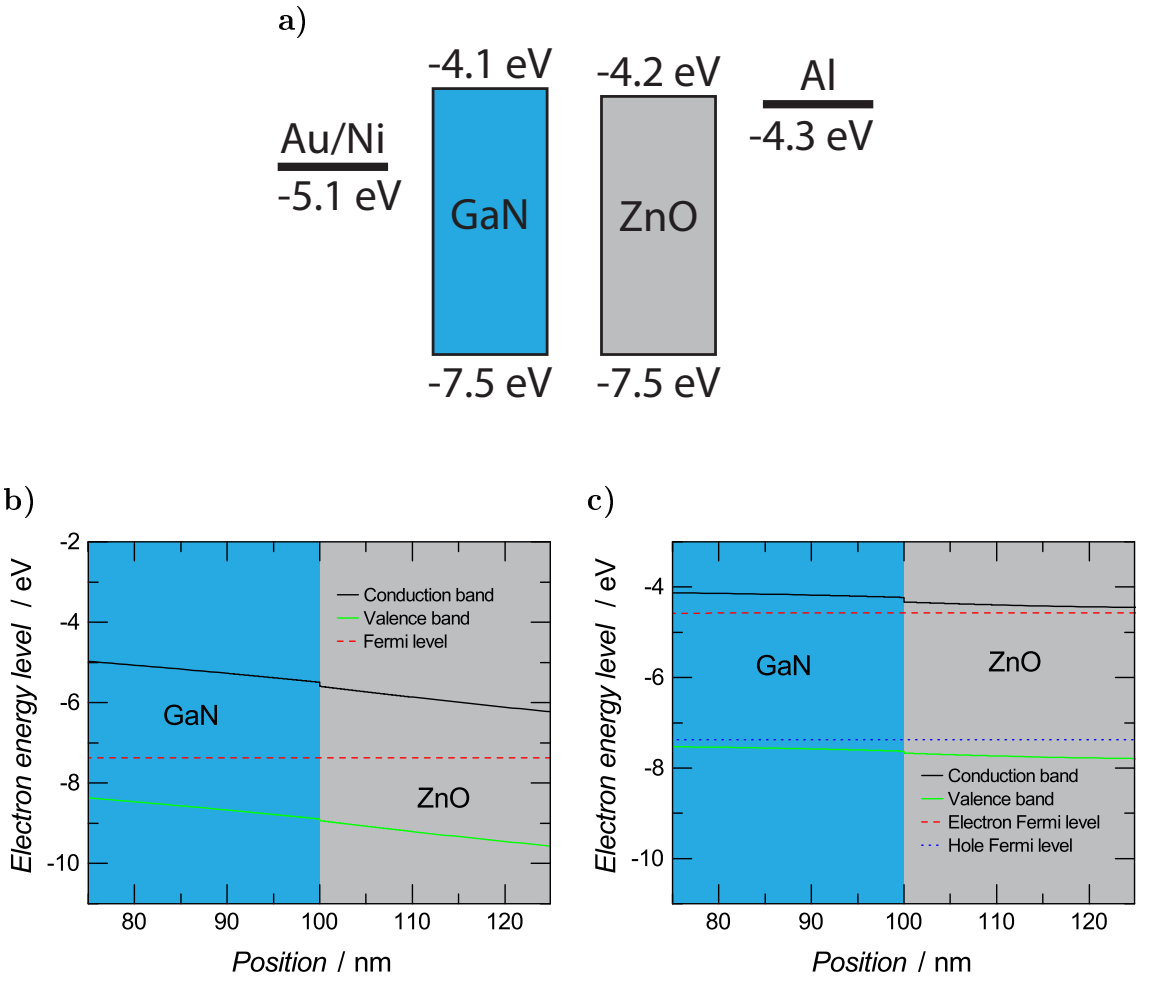

Figure 8.1. – (a) Basic GaN/ZnO band level diagram in vacuum without contact of the materials to each other, showing the electron energy with respect to the vacuum level.[84, 125, 135, 236] (b) Simulation of conduction band level, valence band level, and Fermi level of GaN/ZnO structures without external bias, and (c) band levels, quasi electron and quasi hole Fermi levels at external bias of 2.8 V and current density of 23 mA/cm^2. GaN layer has been filled with with blue and ZnO layer with gray in all figures allowing for quick comparison. For more details regarding the simulation cf. Appendix A.2.

very high emission threshold of at least 10 V and often far above.[28–33] The following observations have been made, that elucidate the reasons behind this:

- Due to the low energetic barrier for electrons of 150 meV at the ZnO/GaN interface, electrons leak into the GaN where they recombine afterwards.[27]

- If an electron blocking layer is applied, the emission threshold voltage is increased by either the blocking layer being insulating or by non-negligible valence band offsets between p-GaN, the chosen electron blocking material and ZnO.[27]

Some time ago, GaN surface oxidation has been identified as an important factor for high voltage emission threshold.[58] After removing the surface Ga_2O_3 layer by etching and applying a subsequent low temperature ZnO growth process to prevent thermal re-oxidation, blue emission at low voltage (5 V) has been observed. If one assumes a Ga_2O_3 layer being present in higher voltage devices, one explanation of the UV luminescence from high voltage GaN/ZnO devices [28–33] might stem from electron blocking by an unintendedly oxidized GaN surface. The conduction band edge of Ga_2O_3 is 1.85 eV above the conduction band edge of GaN at −2.2 eV (Ga_2O_3 valence band edge: −7.3 eV, 0.2 eV above GaN).[275]

Efficient emission from simple p-GaN/ZnO devices without electron blocking layer remains a challenge, as many of the carriers leak into the doped p-GaN layer because of the low interface barrier for electrons, which is only about 150 meV.[27] This results in inefficient emission from the doped GaN layer and interface recombination in the low voltage devices. So far, it has proven to be challenging to combine low voltage emission and carrier restriction to the active zone in a simple, wide area p-GaN/ZnO LED. A lot of electron blocking layers have been tested, among them AlGaN,[27, 68], AlN,[27, 70, 71] Al_2O_3,[276] Ga_2O_3,[275, 277] MgO,[56, 64, 275, 278–282] SiO_2,[29, 40, 283, 284] or polymers.[282, 285] Out of these, only AlN[27] (at 6.3 V) and SiO_2[29] (well above 10 V) have been observed to lead to UV luminescence, and only at these higher voltages. Only very recently, UV emission has been reported at 4.9 V using a GaN/ZnS/ZnO heterojunction.[27] A good valence band match has been recognized to be the main reason for achieving low voltage UV emission. An advantage from using a nanoparticle material might stem from more freedom in production processes. ZnO nanoparticles are produced separately from the device and the ZnO layer is

build by spin-coating or ink-jet printing. It allows the ZnO growth process to be independent from the device.

Here p-GaN/ZnO heterojunction LEDs are presented that show pronounced ZnO NBE emission at 377 nm, appearing at a threshold of 4.4 V. Strong ZnO NBE emission is observed without incorporation of an electron blocking layer. The reasons leading to this optimized device characteristics are analyzed by presenting three device generations called Gen I, II and III. Changes in emission characteristics (chapter 8.3) will be linked directly to changes in the processing of the LEDs (chapter 8.2).

8.2. GaN/ZnO device fabrication

8.2.1. Growth of GaN layers by metal-organic chemical vapor deposition (MOVPE)

The GaN templates have been prepared using metal-organic chemical vapor phase epitaxy (MOVPE) to deposit GaN layers on a commercial sapphire wafer at the department Halbleitertechnologie of the University of Duisburg-Essen. A 2 µm thick intrinsic GaN layer has been deposited first to serve as buffer layer. On top, a 500 nm layer of p-GaN (doped with Mg) has been grown. The growth temperature of Gen I and Gen II substrates has been 920 °C and has been increased for Gen III to 1000 °C. For doping of the p-GaN layer, Mg has been incorporated and activated by an annealing step at 750 °C in nitrogen atmosphere. It has been shown by Dennis Albrecht and Tobias Litwin that ohmic contacts could be formed by Au/Ni contacts that have been annealed at 570 °C after deposition. They observed strongly reduced contact and sheet resistances for a p-GaN layer grown at 1000 °C as opposed to the one grown at 920 °C (Tab. 8.1). The carrier density and mobility can only be measured reproducibly in case of the p-GaN grown at 1000 °C using a hall effect setup, and have been determined to be $9 \times 10^{16}\,\mathrm{cm}^{-3}$ and $20\,\mathrm{cm}^2\,\mathrm{V}^{-1}\,\mathrm{s}^{-1}$, respectively. The Gen I GaN templates have been made by Dr. Ingo Regolin, Gen II and III by Dr. Robert Köster.

Fig. 8.2 shows the transmission T_{opt} of the Gen I GaN substrate. The fringes within the visible spectral range are caused by interference with repeatedly reflected waves. This effect is described by the Airy function (Eq. 8.1), which is also depicted

p-GaN growth temperature °C	Contact resistance Ω	Sheet resistance Ω/□
920	5600	4.0×10^5
1000	88	1.7×10^5

Table 8.1. – Contact and sheet resistances of p-GaN layers grown at 920 °C and 1000 °C after contacting with Au/Ni contacts and subsequent annealing at 570 °C.

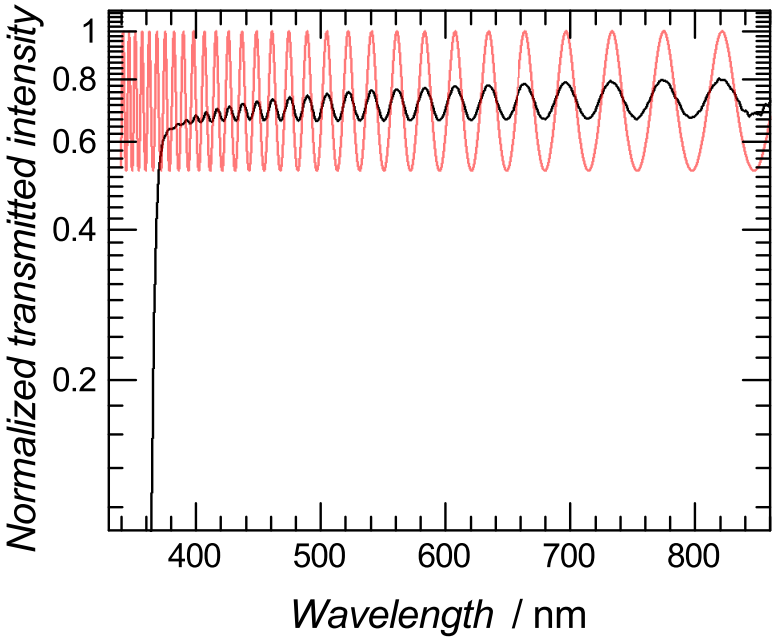

Figure 8.2. – Transmission spectrum of a substrate of Gen I (black line) and Airy function for the layer setup (red line).

in Fig. 8.2 for perpendicular incidence.[286]

$$T_{opt} = \frac{1}{1 + F \sin^2\left(\frac{\delta}{2}\right)} \tag{8.1}$$

$$\text{with} \quad F = 4R_F / \left(1 - R_F\right)^2 \tag{8.2}$$

$$\text{and} \quad \delta = \frac{4\pi d_{GaN}\, \tilde{n}_{GaN}}{\lambda} \tag{8.3}$$

$d_{GaN} = d_{i-GaN} + d_{p-GaN}$ is the thickness of the complete GaN layer including undoped and doped GaN. R_F is the Fresnel reflection given by Eq. 2.29. The refraction index of air $\tilde{n}_{air}$ has been approximated by 1 and the refraction index of GaN $\tilde{n}_{GaN}$ has

been estimated by the Sellmeier equation with specific parameters for GaN (Eq. 8.4, using λ in µm).[287]

$$\tilde{n}_{GaN}(\lambda) = \sqrt{3.60 + \frac{1.75\lambda^2}{\lambda^2 - 0.256^2} + \frac{4.1\lambda^2}{\lambda^2 - 17.86^2}} \tag{8.4}$$

The Sellmeier equation is an empirical formula which is a good approximation in the visible spectral range. When going farther and farther into the UV or IR spectral ranges, the difference between the experimental value and the result from the Sellmeier equation increases.

A perfect fit between the position of the maxima and minima of the measured transmission and the Airy function is observed in the visible spectral range for $d_{GaN} = 2.795\,\mu m$, which is within reasonable agreement to the nominal thickness of 2.5 µm. In the UV range, we observe a steep decline of the transmission due to the GaN band gap. Here, deviations between the calculated Airy function and the measured transmission start to grow because of the inaccuracy of the Sellmeier equation in this range. However, the periodicity of fringes evaluated from experiment and calculation are still close to each other.

8.2.2. Processing of devices

The fabrication of the GaN LEDs will be presented starting with the devices of generation one (Gen I) and describing the changes in the process for generation two and three (Gen II and Gen III, respectively) thereafter. Gen II and Gen III devices have been processed almost identically. A schematic of the final devices is presented in Fig. 8.3. Gen I substrates have been cleaned according to the procedure described in chapter 4.3. After cleaning, a small stripe of about 4 mm at one edge of the sample has been protected by a foil from being coated in the following process, which will be used to contact the p-GaN layer. The ZnO nanoparticle layer on top of the GaN layer is prepared by spin-coating at 4000 rpm from a dispersion presented in chapter 5. The details of the spin-coating process can be found in 4.3. A thickness of the ZnO nanoparticle layer of about 400 nm has been measured by an atomic force microscope in non-contact mode. A 3 mm x 12 mm stripe of Ni and Au has been deposited on one edge of the substrate to form the p-contact. Finally, aluminum is deposited on top of the nanoparticle layer by ebeam evaporation to serve as n-contact.

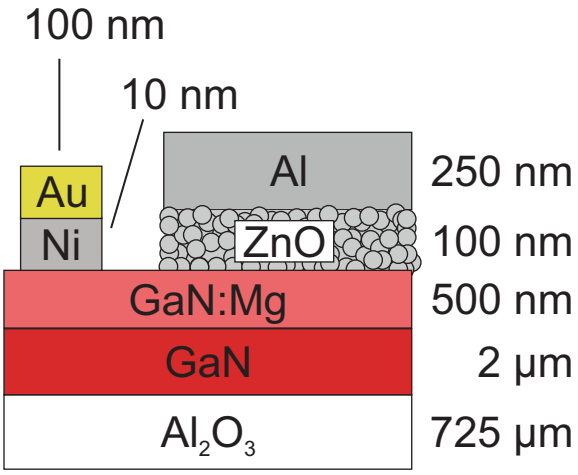

Figure 8.3. – Schematic of GaN/ZnO Gen III LED layer design. The length specifications refer to the respective layer thickness in Gen II and Gen III. For Gen I, most of the values are the same but the ZnO nanoparticle layer is about 400 nm thick.

The following changes to this procedure have been made for Gen II and III:

1. a different cleaning process has been introduced, which includes an etching step to remove Ga_2O_3 from the GaN surface (identical for Gen II and III),
2. evaporation of p-contacts directly after cleaning and etching of the p-GaN template (identical for Gen II and III),
3. annealing of Au/Ni contacts (introduced in Gen III),
4. and filtering of the nanoparticle dispersion (similar for Gen II and III).

which will now be described in detail. The new cleaning process has been developed by Lupan and Co-workers [58] and consists of the following steps:

1. Degreasing in trichloroethylene at 50 °C for 10 min,
2. cleaning in acetone at 53 °C (near the boiling point) in an ultrasonic bath for 5 min,
3. cleaning in methanol at room temperature (21 °C) in an ultrasonic bath,
4. rinsing in de-ionized water,

5. etching in concentrated ammonia (28%) at (60 °C) for 10 min,

6. and finally rinsing in de-ionized water, again.

After cleaning, the substrate has been moved into the chamber of the evaporation system and evacuation has been initiated immediately in order to minimize reoxidation. Thereby the process order is changed: p-contacts are evaporated after cleaning and before spin-coating. Subsequently, p-contacts of Gen III have been annealed at 570 °C for 2 min. For fabrication of Gen II devices, the nanoparticle dispersion has been filtered by syringe filters with a polytetrafluoroethylene (PTFE) membrane with a pore size of 450 nm and centrifuging before spin-coating. Centrifuging has been done by rotating 5 ml of dispersion at 12 000 rpm in a Thermo Scientific Heraeus Biofuge Stratos and only the top, very clear layer has been extracted for further processing. A reduced layer thickness has been observed of 100 nm after spin-coating of the centrifuged dispersion. Centrifuging of dispersions used for fabrication of Gen III devices has been done at 10 000 rpm in an Eppendorf MiniSpin device. No obvious changes have been observed in the nanoparticle layer spin-coated thereafter due to the changes in the centrifuging process.

8.3. GaN/ZnO LED

The electroluminescence spectra of the GaN/ZnO devices are shown in Fig. 8.4 (Gen I), Fig. 8.5 (Gen II), and Fig. 8.6 (Gen III). Electroluminescence spectra become observable for Gen I at around 14 V with a broad spectrum ranging from green-yellow to the infrared range. The maximum intensity is observed at around 730 nm. After an increase of voltage to 17 V, the intensity increases by one magnitude and UV emission not only becomes observable but is already more intense (per nm spectral range) than the visible emission. The voltage threshold >10 V for UV emission is in agreement to previous reports of UV emitting GaN/ZnO devices without nominal electron blocking layer.[28–33] The UV emission has two maxima at 363 nm and 374 nm, and is attributed to an overlap of GaN NBE emission, ZnO NBE emission and GaN/ZnO interface emission, influenced by interference at the GaN layer. With increasing voltage further, UV emission becomes even more dominant over visible emission, exhibiting a ratio of 10:1 (UV counts per wavelength:visible counts per wavelength).

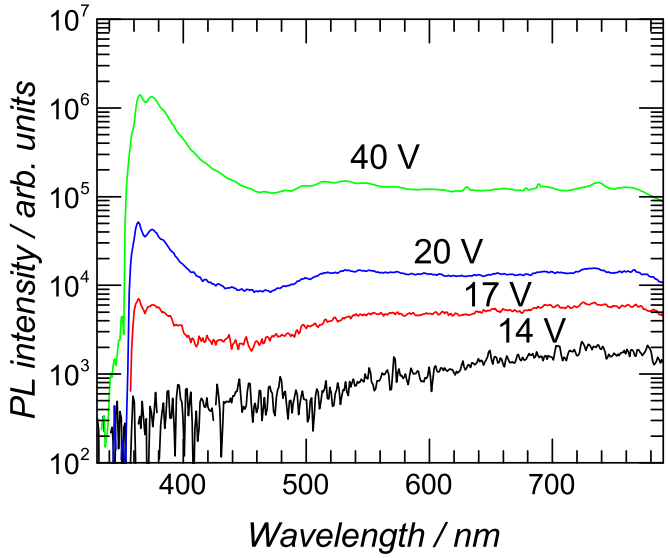

Figure 8.4. – Electroluminescence intensity of the Gen I GaN/ZnO LED in dependence of the wavelength for applied voltages of 14 V, 17 V, 20 V, and 40 V.

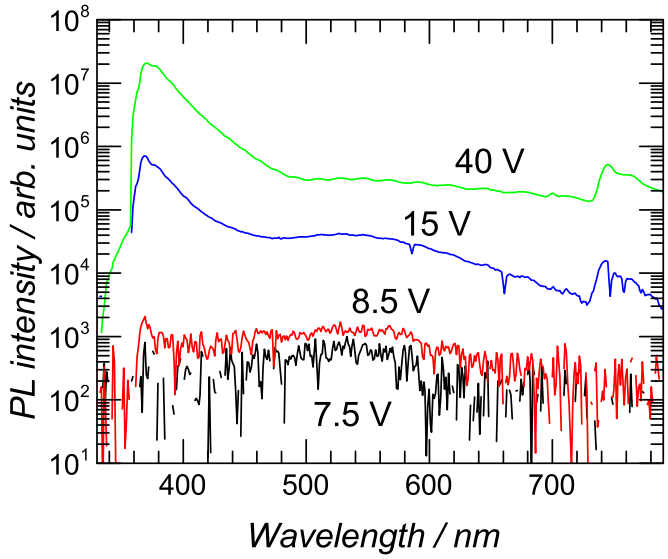

Figure 8.5. – Electroluminescence intensity of the Gen II GaN/ZnO LED in dependence of the wavelength for applied voltages of 7.5 V, 8.5 V, 15 V, and 40 V.

For Gen II devices, the emission detection threshold is strongly reduced to 7.5 V with an emission maximum at around 525 nm in the green spectral range. By in-

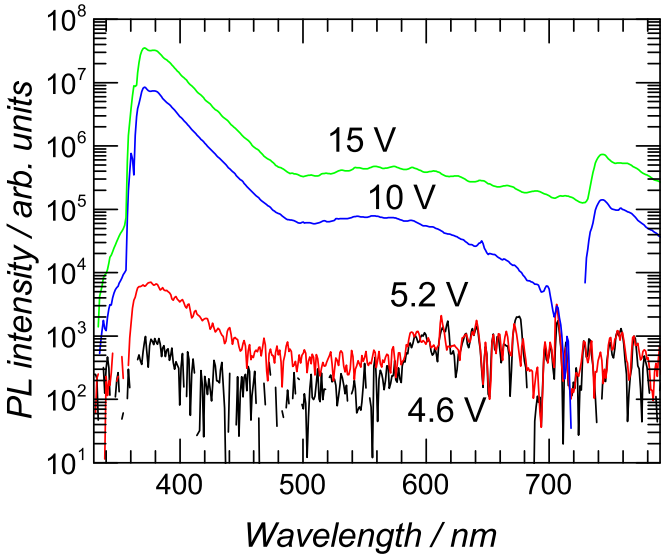

Figure 8.6. – Electroluminescence intensity of the Gen III GaN/ZnO LED in dependence of the wavelength for applied voltages of 4.6 V, 5.2 V, 10 V, and 15 V.

creasing the voltage by only 1 V to 8.5 V, UV emission is becoming detectable with maxima at 370 nm and 377 nm. The intensity rapidly increases with voltage and a gain in intensity by 4 orders of magnitude from 8.5 V to 40 V is found.

For Gen III devices, the emission detection threshold is decreasing again to 4.6 V. Here, UV emission is detectable at the threshold already at 377 nm with an intensity comparable to the value of the visible emission, which is detected in the yellow-red spectral range (580 nm to 780 nm). With increasing voltage further, UV emission at shorter wavelengths is added. This is attributed to an increased amount of electrons leaking into the GaN layer, which has the higher recombination energy. At higher voltages, the visible emission is clearly centered in the green spectral range around 565 nm.

To elucidate the origin of the emission, photoluminescence spectra of GaN have been recorded. They are shown along with the already presented ZnO spectrum (Fig. 5.1) and a GaN/ZnO Gen III LED electroluminescence spectrum in Fig. 8.7. In the UV spectral region, a very close match between ZnO photoluminescence and the LED emission is observed with a maximum at 377 nm. The maximum UV intensity of the UV part of the GaN photoluminescence is at 354 nm. GaN/ZnO interface emission is expected at wavelengths longer than 382 nm, because the GaN valence

band level is assumed to be at least about 100 meV above the ZnO valence band level.[27, 43, 288] This value might even be increased due to a remaining, very thin layer of Ga_2O_3 with an even higher valence band level.[275] Interface emission is suspected to be less intense than emission from band gap related recombination because of a reduced recombination rate of spatially separated charge carriers. Therefore, LED emission at 377 nm is likely originating from ZnO. In the visible range, GaN photoluminescence and the LED emission are very similar in position and shape, which is centered around 565 nm. The ZnO photoluminescence spectrum shows no distinct peak at this wavelength. It is regarded, that the green emission likely originates from GaN, even if ZnO has defect levels in the same spectral region. The share of visible emission from p-GaN might be pronounced in EL, e.g., by charge carrier recombination within the topmost, very defective p-GaN region. The presence of (almost) pure ZnO UV emission at low voltage levels has never been observed in ZnO/p-GaN devices without application of an electron blocking layer before.

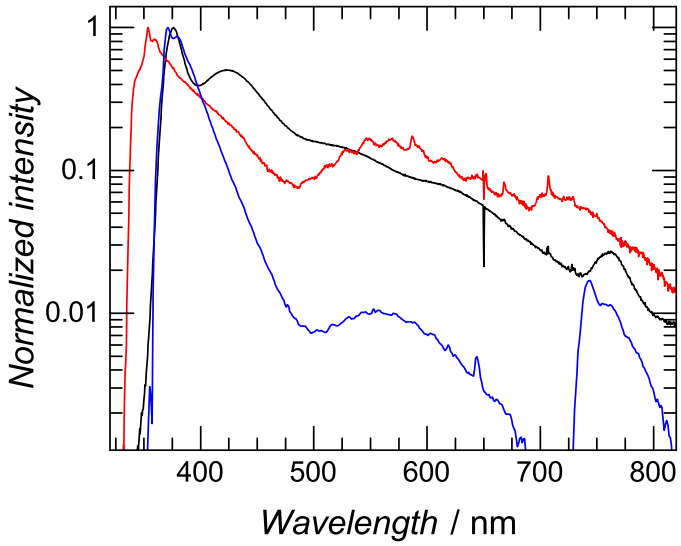

Figure 8.7. – Photoluminescence spectra of ZnO (black line) and GaN (red line) under excitation with a 325 nm HeCd-laser with an intensity of 147 mW/cm^2 and electroluminescence intensity of the Gen III GaN/ZnO LED at an applied voltage of 5.6 V (blue line) in dependence of the wavelength.

The current/voltage characteristics of the Gen I-III GaN/ZnO LEDs are much more stable compared to simple ZnO, NiO/ZnO and WO_3/ZnO devices (Fig. 8.8a). Gen II and III show a steeper increase of current with increasing voltage at low voltage

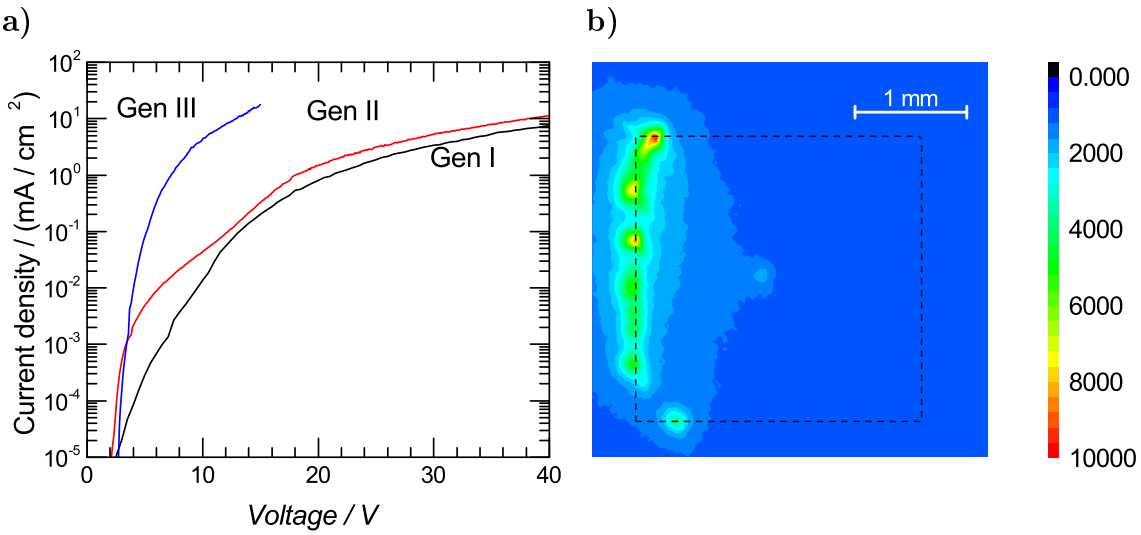

Figure 8.8. – (a) Current / voltage characteristics of the Gen I-III GaN/ZnO LEDs and (b) 2D contour plot of the intensity distribution over the contacted area at 10 V for a Gen III device. The dashed line indicates the area of the aluminum top contact number 2 according to the contact setup shown in Fig. 4.1b. The Ni/Au p-contact is positioned on the left-hand side outside the image.

levels compared to the Gen I device. At voltages above 12 V, the difference between Gen I and Gen II devices is rather small and currents observed are clearly within one magnitude at a certain voltage. The remaining current difference might caused by reduced resistance by reducing the thickness of the Ga_2O_3 and the ZnO nanoparticle layers. The Gen III devices allow for much more current. This is might be related to a better material quality and a better incorporation of magnesia dopants by increasing the GaN growth temperature. But nevertheless, a quick estimation using the Gen III p-GaN sheet resistance of $1.7 \times 10^5\,(\Omega/\square)/\mathrm{cm}^3$ shows that still most of the major voltage drop occurs within the GaN layer. This leads to a concentration of the current flow at the side of the contact pad which is situated towards the p-contact. Therefore, light emission is concentrated in this area as well, which is shown by a picture of the contacted area in Fig. 8.8b. This observation leads to the assumption that the low share of visible emission from these devices may be caused by saturation of defect recombination centers. Additional facts supporting this theory are the typically long radiative recombination time in the order of µs for transitions involving defect states of ZnO,[212, 289] and an increased share of UV luminescence with increased intensity.

As previous reports on GaN/ZnO devices do not report on external quantum ef-

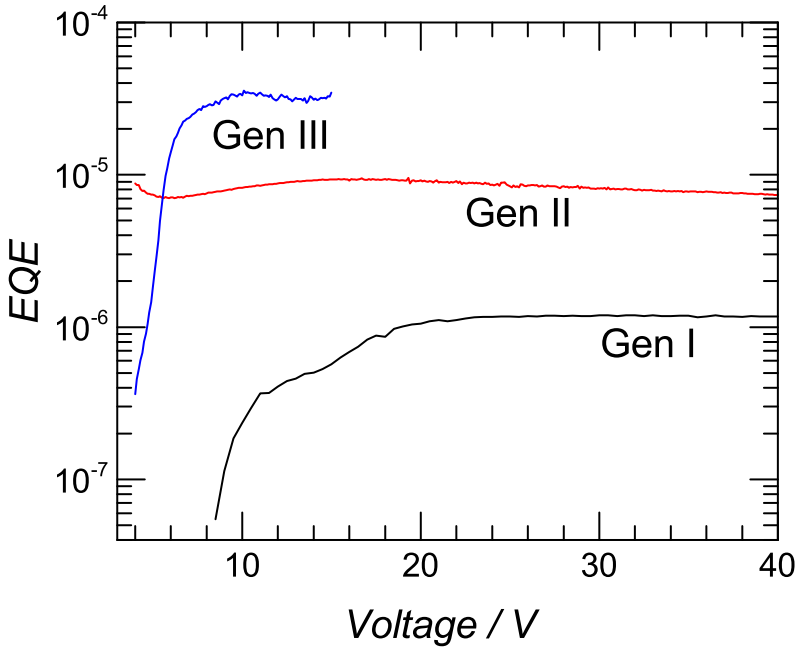

Figure 8.9. – External quantum efficiency characteristic of the Gen I-III GaN/ZnO LEDs.

ficiency, this information has been missing. Fig. 8.9 shows the external quantum efficiency characteristic of the Gen I-III GaN/ZnO LEDs. For Gen I, two times an increased slope of the EQE characteristic with increasing voltage is observed: at the visible emission onset (8.5 V to 13.5 V) and at the UV emission onset (15 V to 17 V), showing when the external voltage has reached a sufficient level to efficiently inject into the respective luminescent defect or band gap states. We observe a maximum η_{ext} of 1.2×10^{-6} above 25 V for this device. According to Eq. 2.28, an injection efficiency of 1.0 % is estimated using the nanoparticles quantum yield of 2.3×10^{-3} and the out-coupling efficiency of 5 % of GaN devices without back-reflector.[138] After this point, the efficiency remains constant if the voltage is increased further.

The Gen II device shows luminescence at very low voltage levels. But as the emission intensity has been so weak below 7.5 V that no spectra could be recorded, the origin of this low voltage emission remains unclear. The maximum EQE η_{ext} is determined to be 9.3×10^{-6} at 15.1 V, corresponding to an estimated η_{inj} of 8.1 %. The efficiency is constant with increasing voltage for the presented experiment. The Gen III EQE/voltage relation shows again a steep increase at the emission onset voltage, which is here at 3.8 V to 6.1 V. The maximum η_{ext} is attained at 10.1 V.

	Gen I	Gen II	Gen III
Vis. detection	14 V	7.5 V	4.6 V
UV detection	17 V	8.5 V	4.6 V
η_{ext}	1.2×10^{-6}	9.3×10^{-6}	3.6×10^{-5}
η_{inj}	1.0 %	8.1 %	31 %

Table 8.2. – GaN/ZnO LED Gen I-III key figures.

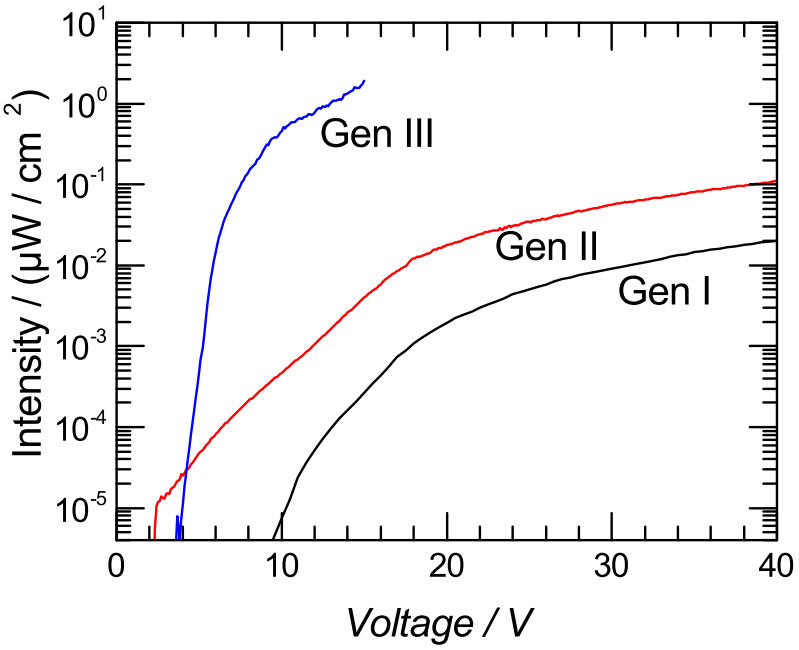

Figure 8.10. – Electroluminescence intensity as a function of voltage of the Gen I-III GaN/ZnO LED.

It is observed to be 3.6×10^{-5}, what corresponds to an η_{inj} of 31 %. The detection thresholds and efficiencies of the GaN/ZnO devices are summed up in Tab. 8.2.

The electroluminescence intensity as a function of voltage of the Gen I-III GaN/ZnO LED is depicted in Fig. 8.10. The shapes of the graphs belonging to Gen I and II are very similar, with the intensity of Gen II being about one magnitude above the intensity of Gen I due to the increase of the external quantum efficiency. From Gen II to Gen III, not only the injection efficiency has been increased, but the current is strongly increased, as well, leading to an increase of almost four magnitudes of emission intensity. Still, the even the maximum intensity of 2 µW/cm^2, which has been measured for the Gen III device at 15 V, is rather low for practical applications.

A quick estimation of the external power efficiency (light output power per electrical input power) of Gen III at 15 V yields to a value of 7.5×10^{-6}, which is about five times smaller than the determined external quantum efficiency. Because only about 3 V of 15 V are needed to excite emission at about 3 eV, additional four fifths of the electrical power are lost non-radiatively, which explains the difference between external power efficiency and external quantum efficiency.

With a maximum injection efficiency of 31 % of the Gen III devices, most of the external quantum efficiency is lost due to the not optimized quantum yield of the active material. Therefore, high quantum yield ZnO nanoparticles have to be developed. This topic will be covered in the next chapter, where highly luminescent, green emitting ZnO quantum dots will be presented.

9. Highly luminescent ZnO quantum dots

Note: The contents of this chapter have already been published in [290].

9.1. Production in a nonthermal plasma

Liquid phase processing of nanoparticles is a standard method to produce high quality nanoparticles exhibiting superior luminescent quantum yields that has been extremely successful in the last two decades. Nanoparticles with good emission characteristics have been presented from different material systems, among them CdSe,[130–132] InP,[185] Si[187] and ZnO[23, 24, 102, 205, 206, 208, 215, 216].

But despite the very successful history, and liquid phase processing being regarded satisfying in laboratory environments where typically low material volumes are sufficient, gas phase processing of nanoparticles offers a wide range of advantages that are especially important for industrial mass production. Liquid processes are typically executed in batch form, such as mixing a set amount of different reactants with each other, while gas phase processes can be run continuously. Therefore, less variation in the nanoparticles characteristics is expected.[291] Gas phase processes are also easily up-scalable to industry production volumes in the kilogram or even ton range, making them especially interesting for practical applications. Additionally, particle formation is usually much faster in gas phase processes with only about a few milliseconds to tens of milliseconds compared to liquid phase ones and is less complex.[292] Liquid phase processes often have to follow a detailed procedure including several heating/cooling and stirring steps, which have to be executed manually or by complex process controlling systems. If a multilayer device is to be built out of several layers of different nanoparticles, orthogonal solvents have to be used in order to prevent dissolving of the layer coated before applying the next. This can be handled much easier with gas phase processing utilizing subsequent, direct deposition of nanoparticle layers onto the device structure.[293] Another very important

aspect of gas phase processing is the fact that it is able to produce quantum dots free of insulating surface ligands which is especially important for electrical devices like LEDs. Therefore, it is highly desirable to develop production processes to synthesize nanoparticles from the gas phase that exhibit characteristics which are comparable to the superior properties of particles made from liquid phase processing in order to facilitate industrial applications.

A lot of gas phase processes have been presented that are capable of making quantum dots, among them flame pyrolysis,[103, 104] hot wall reactors,[105, 106] microwave[104] and radio frequency plasma reactors.[294] Out of these, nonthermal plasma reactors have shown the greatest potential to produce semiconductor quantum dots exhibiting high luminescent quantum yields, as it has been demonstrated for silicon with quantum yields above 60 %.[186, 295–297] Aside from highly luminescent silicon quantum dots, germanium quantum dots made in a nonthermal plasma have been investigated and have shown promising properties for optical applications. Narrow band gap photoluminescence shifted by quantum confinement has been identified, which has been scarcely observed from germanium nanocrystals before.[298] Currently, experiments are done to evaluate the quantum yield of the germanium quantum dots.[298] Synthesizing of compound semiconductor nanoparticles from the gas phase has been much more difficult. While several materials have been studied, quantum yields remained low and reports on their actual value are scarce. The photoluminescence quantum yield of InP quantum dots, that have been capped with organic ligands and that have been made from a nonthermal plasma, has been reported not to exceed 1 %.[299]

This promising method shall be investigated for synthesis of ZnO quantum dots and their luminescence properties here. ZnO quantum dots of high luminescent quantum yield have already been reported multiple times from liquid phase processing independently. Among the stable quantum yields that have been published are 26 % without any additional treatment,[24] and 61 % for LiOH-mediated growth and subsequent post growth surface capping.[23]

It has been observed that the luminescent quantum yield of green emission from ZnO quantum dots could be increased by reducing their size.[208] The supposed reason behind this is that surface states are involved in the recombination process.[213] The density of these surface states is increased by reducing the particle diameter, simply because the surface-to-volume ratio is increased. Some time ago, very small

ZnO nanoparticles exhibiting a diameter between 4 nm to 6 nm have been made in a microwave plasma which might be the smallest ones until today, but unfortunately their luminescence properties have not been investigated.[104] The ZnO nanoparticle production in a nonthermal plasma is a promising method to reduce the size even further while retaining a high crystal quality as highly luminescent Si quantum dots synthesized by the same method have been reported to be as small as 3 nm.[296]

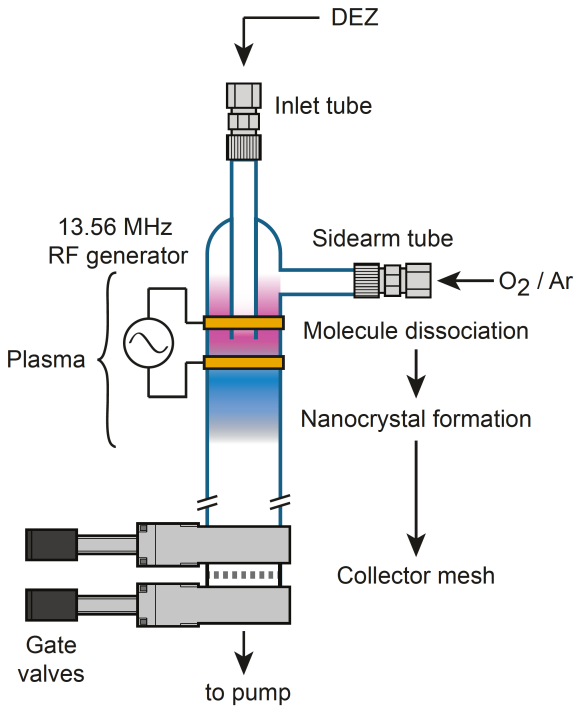

Figure 9.1. – Sketch of the plasma reactor with the newly designed inlet tubes.[290]

A low pressure flow-through reactor operated with a 13.56 MHz radio-frequency source has been designed for producing ZnO quantum dots. Diethylzinc (DEZ) and an oxygen gas (O_2) are used as precursor materials, while argon (Ar) has been injected to serve as background gas. It is very important to separate these precursors by using two different injection lines before they finally meet inside the plasma because otherwise they would react in an uncontrolled way with each other. Therefore, a new reactor chamber has been designed as shown in Fig. 9.1 with the inlet tube of DEZ extending into the main reactor chamber and continuing into the plasma region between both electrodes. The upper end of the plasma torch is situated approximately 1 cm above this point and is ignited downstream. O_2/Ar is injected

through a sidearm tube above the torch. Thereby the goal of dissociation of both precursors before they meet each other in the plasma zone has been accomplished. The flow rate of DEZ has been controlled by a needle valve and has been set to 6 sccm. The flow rates of oxygen and argon have been 3 sccm and 40 sccm, respectively. The nominally applied plasma power supervised by a power meter has been adjusted to 100 W, although only a much lower value has been actually coupled into the plasma. For collection of the produced ZnO quantum dots, a stainless steel mesh at the reactor exhaust has been used. The size of the ZnO quantum dots has been varied by adjusting their residence time inside the plasma, which has been influenced by the pumping rate throttled by a butterfly valve before the pumping line. The pressure inside the plasma chamber has changed thereby between 0.5 Torr and 1.3 Torr (66 Pa to 200 Pa). A reactor chamber with a diameter of 1 inch (2.54 cm) has been used to make all but the smallest ZnO quantum dots, which have been made in a chamber of reduced diameter (0.75 inch/1.91 cm). Plasma power and flow rates have been left unchanged.

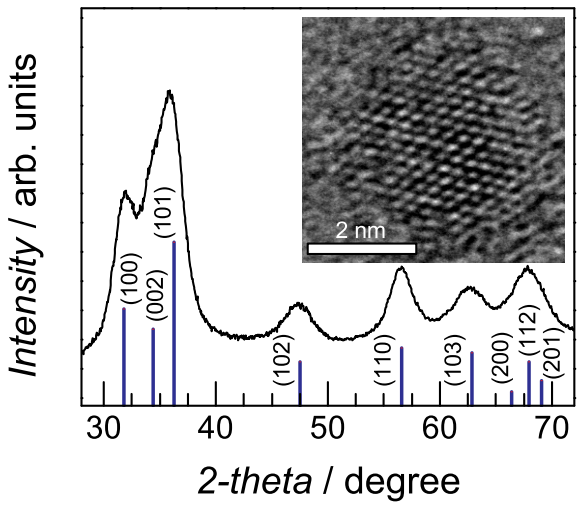

Figure 9.2. – X-ray diffraction study of ZnO quantum dots made in a non-thermal plasma. The vertical lines give an indication of the ZnO bulk reflex position and relative intensity. The diffraction pattern presented has been recorded from a sample with a particle diameter of 3.4 nm. Vertical lines indicate the diffraction peak position and intensity of bulk wurtzite ZnO. A HRTEM image of the same sample is presented as inset.[290]

X-ray diffraction (XRD) studies on the produced ZnO quantum dots have been conducted which prove their identity and good crystallinity. The observed diffraction patterns match closely with the pattern reported for wurtzite ZnO. The size of the quantum dots is estimated from the Scherrer equation which gives a relation on XRD peak broadening with samples crystallite size.[258] Thereby, diameters of 3.4 nm, 3.0 nm and 2.4 nm of the quantum dots produced in the larger-diameter reactor (1 inch) at 1.3 Torr, 1.0 Torr, and 0.5 Torr have been determined, respectively, and 2.1 nm has been calculated for the ones made in the smaller-diameter tube (0.75 inch). These values are among the lowest reported in literature for ZnO quantum dots made from the gas phase. The XRD pattern of ZnO quantum dots with a diameter of 3.4 nm is shown in Fig. 9.2, and an image from high-resolution transmission electron microscopy (HRTEM) of the same particles is shown in the inset giving additional proof of their very good crystallinity from the periodic electron diffraction pattern observed.

9.2. Luminescence properties

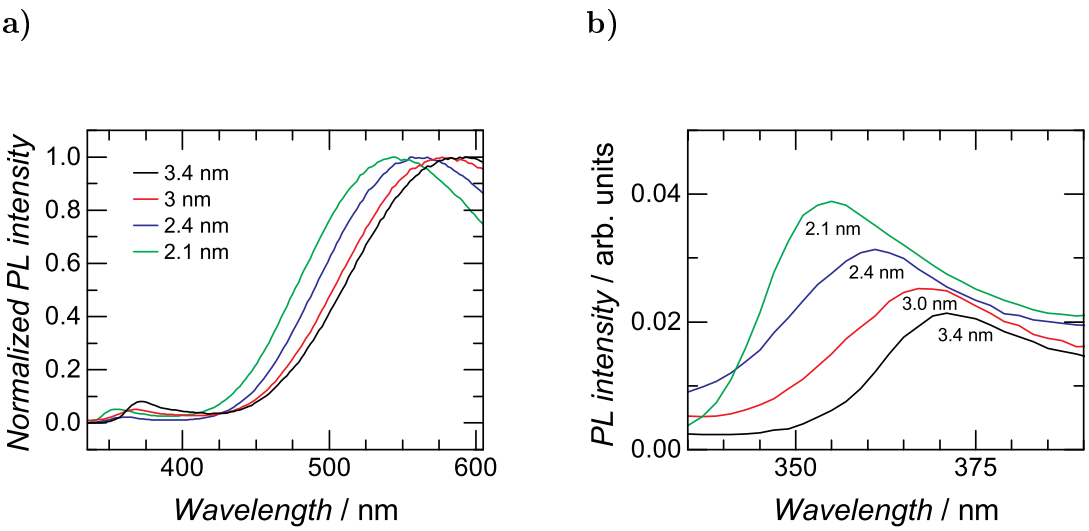

Figure 9.3. – (a) Normalized photoluminescence spectra of the ZnO quantum dots in ethanol with diameters between 2.1 nm and 3.4 nm. (b) Near-band gap exciton emission from the same measurements in more detail.[290]

Photoluminescence spectra of the ZnO quantum dots have been recorded. Prior to

measurement, the particles have been dispersed in ethanol after being stored for 12 h in ambient air. Fig. 9.3a shows the normalized spectra including the whole examined range, while Fig. 9.3b concentrates on the UV part only. The main share of the emission spreads over the whole visible range and attains its maximum intensity in the green-yellow area around 550 nm to 590 nm. It is attributed to recombination involving defect and surface states as discussed in detail in chapter 9.3. A minor contribution to the emission comes from near-band gap exciton related recombination in the UV range. A blue shift of the emission maxima with decreasing size is observed, for both, the visible and the UV emission. While the quantum dots with a diameter of 3.4 nm show near-band gap emission at 371 nm, this value is shifted to 355 nm for a diameter of 2.1 nm. This is attributed to quantum confinement as the size of the quantum dots is below the exciton Bohr radius of ZnO of 2.34 nm.[300] The size dependent band gap shift, however, is much weaker than it would be expected from calculation by a simple effective mass model. For example, the effective mass model predicts an emission wavelength of 305 nm for a particle diameter of 3.4 nm as opposed to the peak emission wavelength of 371 nm detected here. This strong deviation has been observed multiple times for ZnO and is subject of intensive discussions.[182, 188–192] Some of the main reasons proclaimed in literature are: Stokes shift creating a wavelength difference between the position of absorption and emission peaks because of different fine structure states involved,[188, 192] or due to phonon interaction,[188] finite well depth height and other effects leading to extension of the carrier wave function to surface states,[182] or a Stark shift related to a strong electric field created by surface charges.[191]

In the visible spectral range, the observed emission peak wavelength is shifted, as well, in agreement with literature.[189, 301] While the maximum intensity is recorded at 589 nm for 3.4 nm quantum dots, it is detected at 545 nm for 2.1 nm quantum dots. The magnitude of the energy shifts of UV and visible emission are very similar with 0.15 eV and 0.17 eV, respectively. This is an indication that visible radiative recombination most likely involves electrons transitioning from states in or close to the conduction band to deep defects, as the effective electron mass in ZnO is smaller than the respective value for holes. This leads to upward movement of the conduction band edge making the main contribution to band gap widening in the quantum confinement regime.[149, 158, 190, 302–305] A mechanism for green luminescence based on defects of such energetic positioning is discussed in detail in chapter 9.3.

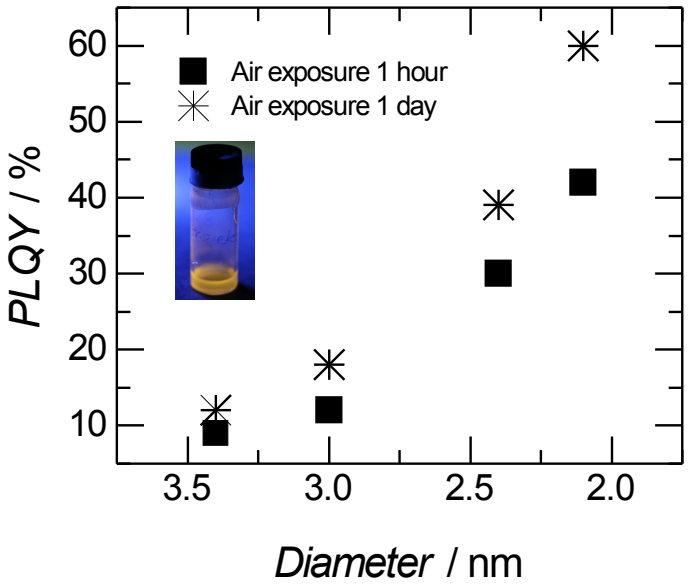

Figure 9.4. – Photoluminescence quantum yield (PLQY) of ZnO quantum dot ethanol dispersions as function of the particle diameter. The quantum yield is determined after air exposure of the dispersion for one hour and one day, respectively. A picture of 2.1 nm quantum dots in ethanol under UV illumination at 360 nm is shown in the inset.[290]

The quantum yield of the ZnO quantum dots has been determined in ethanol dispersion under excitation by an UV LED emitting at 315 nm. The results are depicted in Fig. 9.4. The entirety of emission, including UV and visible photoluminescence, has been included in the determination of these values. The quantum yield is observed to be increased by reduction of the quantum dot size as proposed. It grows strongly from 9 % for 3.4 nm quantum dots to 42 % for 2.1 nm ones. These values are increased even further after exposure to ambient air for one day to 12 % and 60 %, respectively. A comparable increase of the quantum yield with reduced particle diameter has already been observed from liquid phase synthesis, while the maximum value has been much lower, however.[208] The maximum value obtained from these experiments, 60 %, is the highest quantum efficiency determined for any compound semiconductor quantum dots made from the gas phase. Interestingly, this behavior of ZnO is quite different from highly efficient quantum dots made of other materials. In

example, the quantum yield of Si and CdSe quantum dots is observed to decline after size reduction.[155, 187] This exceptional behavior gives a clear indication that the luminescence observed here is surface related, which is not the case for luminescent materials with band gap related emission.

9.3. Mechanism of green-yellow luminescence

A lot of discussions have been conducted about the responsible mechanism for green-yellow luminescence. Most reports favor recombination at singly ionized oxygen vacancies,[189, 194, 198, 208–213] which is strongly enhanced for samples with high surface-to-volume ratio, like nanostructures, by the presence of surface OH-groups.[189, 194, 212, 214] The recombination process involving OH-groups is shown schematically in Fig. 9.5. After electron hole pair creation, the hole is trapped fast by such a surface OH-group (Eq. 9.1). The hole has a finite probability to tunnel back into the ZnO crystal to a singly ionized oxygen vacancy[1], which thereby becomes doubly ionized (Eq. 9.2.). An electron from the conduction band might then recombine at this doubly ionized oxygen vacancy and emit green light (Eq. 9.3).

$$\mathrm{OH_s^-} + \mathrm{h_{VB}^+} \longrightarrow \mathrm{OH_s^\bullet} \tag{9.1}$$

$$\mathrm{OH_s^\bullet} + \mathrm{V_O^\bullet} \longrightarrow \mathrm{OH_s^-} + \mathrm{V_O^{\bullet\bullet}} \tag{9.2}$$

$$\mathrm{V_O^{\bullet\bullet}} + \mathrm{e_{CB}^-} \longrightarrow \mathrm{V_O^\bullet} + h\nu \quad (green) \tag{9.3}$$

A variant has been proposed suggesting that the electron does not recombine from the conduction band, but from shallow donors in a donor acceptor pair recombination.[306]. Other reports argue that $\mathrm{V_O^\bullet}$ might be the recombination center and that the electron at this center recombines with a hole from the valence band.[22, 198]

Resulting from this mechanism, the higher quantum yield of smaller quantum dots is explained by the increased surface-to-volume ratio leading to increased availability of both, oxygen vacancies and OH-groups at the surface.[307, 308] Additionally, the probability for the tunneling step involved in this process is expected to be strongly increased with reduced particle size.[208] This would be consistent with our exper-

[1] A doubly negative charged oxygen vacancy is regarded neutral (V_O^x), a singly charged singly ionized ($V_O^\bullet$), and an uncharged one doubly ionized ($V_O^{\bullet\bullet}$). This definition describes the charge difference to a regular O^{2-} atom at the lattice spot in an ideal ZnO crystal.

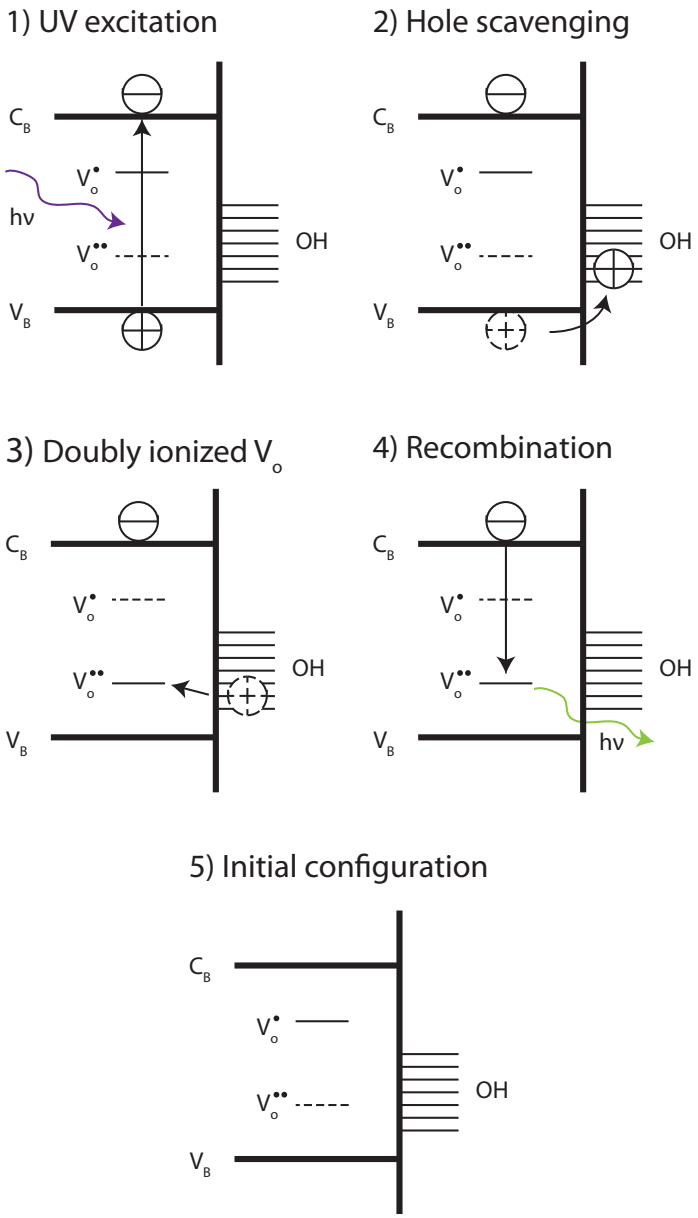

Figure 9.5. – Principle steps in the recombination process involving green emission by transitions of the conduction band to doubly ionized oxygen vacancies with assistance of surface OH-groups. 1) Excitation of an electron hole pair, e.g. by a photon with an energy above the band gap. 2) Capturing of the hole by surface OH-groups, which get oxidized. 3) Tunneling of the hole to a singly ionized oxygen vacancy $V_O^{\bullet}$ which becomes thereby doubly ionized ($V_O^{\bullet\bullet}$). 4) Recombination of an electron from the conduction band with the doubly ionized oxygen vacancy $V_O^{\bullet\bullet}$. 5) After electron hole pair recombination, the initial situation is restored.[189, 194, 212, 214]

imental results. Nevertheless, multiple mechanisms have been reported which very likely exist. The share of different mechanisms of the emission may then differ individually based on the relative densities of the involved states which are influenced by the production methods and the surface conditions. A description of other proposed recombination mechanisms involving defect states can be found in chapter 3.3.2.

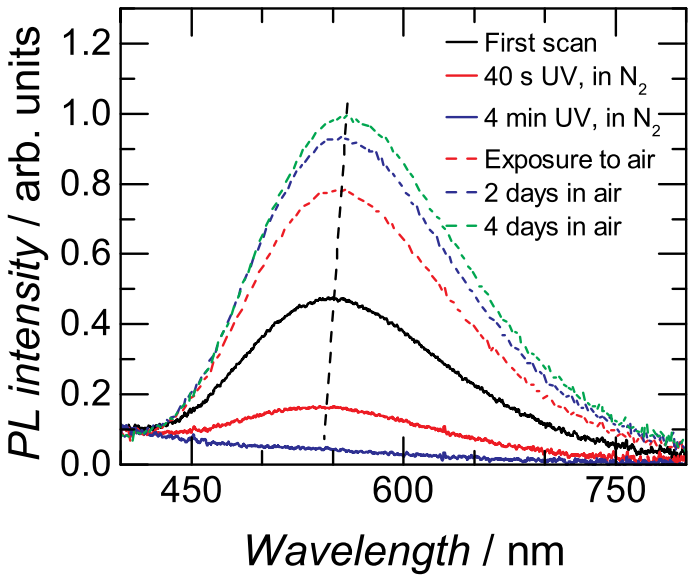

Figure 9.6. – Photoluminescence measurements of ZnO quantum dots after illumination by UV light in nitrogen and ambient atmosphere with a size of 2.4 nm. The peak wavelength shift of the emission is indicated by a dashed line to serve as guide to the eye.[290]

As the luminescence observed is supposed to be influenced by surface states, atmosphere conditions are suspected to influence the emission characteristics to a great extent. Therefore, photoluminescence spectra of ZnO quantum dots dispersed in ethanol with a diameter of 2.4 nm have been recorded under UV illumination in nitrogen and ambient air atmosphere (Fig. 9.6). Nitrogen atmosphere is expected to reduce the amount of oxygen present on the surface compared to air.

Initially, photoluminescence measurements of the as-produced quantum dots in nitrogen have been made, which have never been exposed to air. The first spectrum has been recorded only a few tens of seconds after beginning the excitation by UV light

(black line). After longer exposure to UV light while still in nitrogen atmosphere, the green-yellow emission starts to lose in intensity until it is completely gone after 4 min. It is observed, that this effect is reversed by exposure of the same dispersion to ambient air. The green-yellow intensity becomes clearly detectable again and increases further, but on a much longer timescale of several days.

A similar quenching of the intensity of visible emission after continuous UV illumination under anaerobic conditions has already been discussed several times.[188, 191, 212, 217, 309] Common agreement is made that quenching is initiated by solvent molecules like ethanol (C_2O_5OH) scavenging holes from the quantum dots (Eq. 9.4).

$$2h^+_{VB} + C_2O_5OH \quad \longrightarrow \quad CH_3CHO + 2H^+ \quad [310] \tag{9.4}$$

Under aerobic conditions, equilibrium is assured by a reverse process involving surface adsorbed oxygen ($O_{2,abs}$). It reacts with free hydrogen to dihydrogen dioxide and consumes two electrons (Eq. 9.5, Zn_s: zinc atom at the nanoparticle surface).

$$2e^-_{CB} + Zn_s - O_{2,abs} + 2H^+ \quad \longrightarrow \quad Zn_s + H_2O_2 \quad [214] \tag{9.5}$$

While both reactions can be repeated arbitrarily often in ambient atmosphere because the availability of solvent and oxygen molecules is unlimited, the latter is prevented under anaerobic conditions by the absence of free oxygen. Excess electrons are no longer removed and the quantum dots become charged. The mechanism, how this charging reduces the luminescence, is still in discussion. Some time ago, it has been suggested that trapping of excess electrons at the $V^{\bullet}_O$ recombination center forms neutral oxygen vacancies V^{x}_O which act as shallow donors near the conduction band. This prevents the mechanism for green luminescence while band gap recombination is still a possible relaxation channel, which thereby becomes more pronounced.[213] A more recent report disagrees with this explanation, because no signal of the paramagnetic $V^{\bullet}_O$ could be detected in EPR measurements of the ZnO quantum dot sample. They proposed a de-excitation of the green recombination centers by the Auger effect being responsible for the declining the visible luminescence.[217] The same study suggests that possibly some non-radiative recombination mechanism are less effective due to nanoparticle charging, as well, leading to UV relaxation gaining a larger share and UV emission being increased.

Under UV illumination, a shift to shorter wavelengths is observed for the visible emission, while it is shifted to longer wavelengths upon exposure to ambient air. A dashed line has been added in Fig. 9.6 to serves as guide to the eye for making this shift easily recognizable. In literature, observations regarding a shift under these conditions are quite different. While some experiments show shifts similar to the measurements presented here,[191, 212] no or only little shifts were observed from others.[188, 217] While the definite reason for the observation of a blue shift is still unsure, one hypothesis is that the blue shift is related to quantum dot charging and occupation of higher electron states.[191]

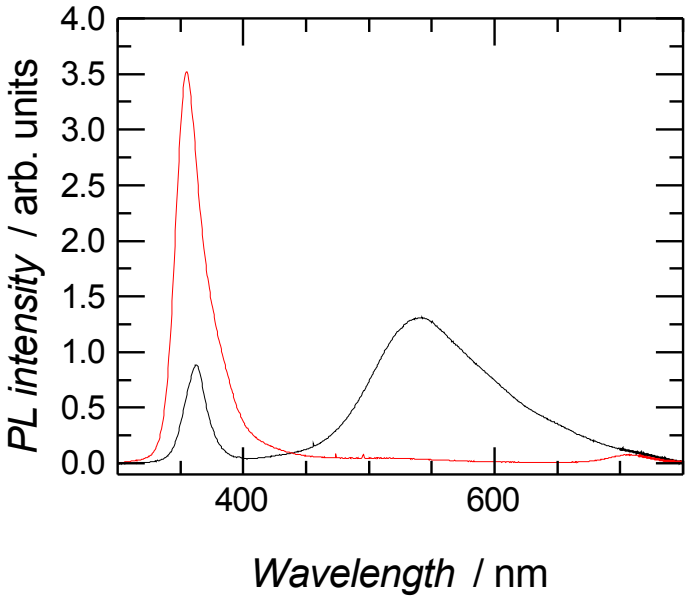

Figure 9.7. – Photoluminescence measurements in ambient atmosphere (black) and in vacuum (red, 5×10^{-5} mbar) of quantum dots with a diameter of 2.1 nm.[290]

To confirm the importance of oxygen and OH groups being present in the atmosphere for green luminescence, photoluminescence measurements of quantum dots in high vacuum (5×10^{-5} mbar) have been made (Fig. 9.7). Vacuum is expected to desorb surface oxygen-containing species, such as O_2 and OH groups,[184, 213] and green luminescence is thereby expected to vanish. Indeed, green-yellow luminescence is completely suppressed under these conditions, giving another confirmation for the

proposed mechanisms. It is observed that the intensity of UV luminescence is increased by approximately the same amount which is lost in the green spectral range. This leads to the total intensity being unchanged, interestingly.

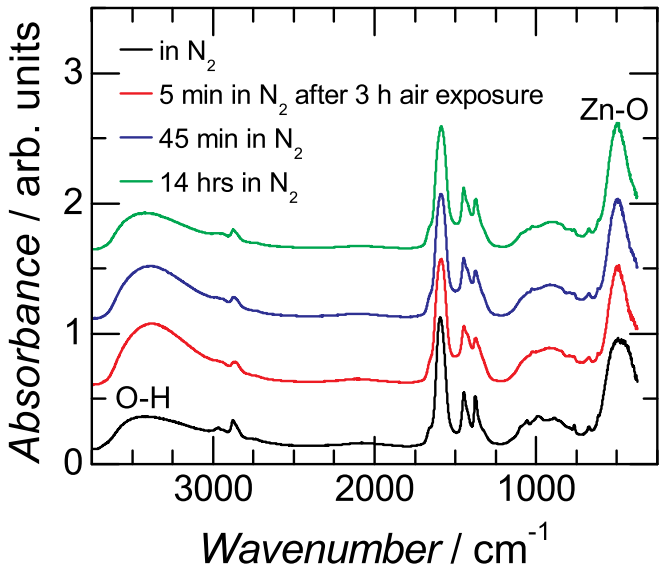

Figure 9.8. – FTIR spectra of ZnO quantum dots with a diameter of 2.4 nm Spectra have been recorded in nitrogen atmosphere, after air exposure for 3 h and reintroduction into nitrogen atmosphere for 5 min, 45 min and 14 hrs.[290]

FTIR measurements are used to gain more information about the surface chemistry of ZnO quantum dots in nitrogen and ambient air atmospheres (Fig. 9.8), which are supposed to have a great influence on the luminescence properties. According to the presented mechanism, the concentration of OH groups is especially important. Therefore, special emphasis is put on the O-H stretching vibration at 3400 cm^{-1}. The smallest OH signal is detected from ZnO quantum dots, that have been stored in nitrogen and that have never been in contact with ambient air. This signal is significantly increased after exposure to air for 3 hrs. After reintroducing the same sample into nitrogen atmosphere, this signal is observed to be reduced again. The effect becomes clearly notable after 45 min, already, and after 14 hrs, the signal intensity almost reverts back to the level before the particles have been in contact with air. From these results, it is concluded that exposure to air increases the concentration

of OH groups present on the quantum dot surface which play a major role in the proposed green radiative recombination process. Therefore, these observations are consistent with the increased intensity of green luminescence observed from photoluminescence measurements and explain, together with the availability of oxygen for de-charging, why the record efficiency has been recorded for the air exposed sample.

10. Summary and conclusions

The goal of this work was to develop ZnO nanoparticle LEDs with inorganic hole injection layers. The performance of a LED concept can be described by the external quantum efficiency, which is influenced by the out-coupling efficiency, the injection efficiency and the luminescence yield of the active material.[1] Because out-coupling concepts can be transferred from other LED designs,[95] the focus has been set on improving the injection efficiency and the quantum yield. The major challenge for efficient injection is found in the very low valence band of ZnO, which makes injection of holes into this material especially difficult. In order to improve the injection efficiency, different electron extraction/hole injection layers, WO_3, NiO and GaN, have been tested with different work functions (chapters 6, 7 and 8). Apart from the energetic configuration, the studied hole injection layers differed in significant other properties like whether being n- or p-conducting and providing an electron barrier or not. In order to optimize the quantum yield, ZnO nanoparticles from a nonthermal plasma reactor have been investigated that have exhibited intense green luminescence (chapter 9). The influences of atmosphere and particle diameter on the emission have been studied for understanding of the mechanism leading to efficient green radiative recombination in these particles and to enhance their quantum yield further.

Prior to further improvement studies, a simple ITO/ZnO/Al device has been characterized to serve as base reference. Indications of an unipolar driven recombination mechanism have been observed by a symmetrical emission intensity as a function of voltage in forward and reverse direction, respectively. A very low injection efficiency of 1.0×10^{-4} has been estimated for this device.

A WO_3/ZnO nn-heterojunction concept has been developed afterwards. The very low work function of WO_3 of 6.65 eV allowed the intrinsic n-conductor to extract electrons from defect levels within the ZnO band gap. Thereby a hole is left behind that might recombine radiatively. By inserting this material into the ZnO nanoparticle LED, a broad electroluminescence spectrum could be observed that covered the

entire visible spectral range including the blue regime. Only band gap UV emission could not be observed in a stable operation mode. After increasing the applied bias beyond 7 V, the current at a constant voltage level has been observed to decrease over time. However, increasing the voltage beyond this level has been necessary to detect a substantial emission intensity, which places the required operation voltage into an unstable regime.

The missing electron blocking layer could be implemented by replacing WO_3 with a NiO hole injection layer. NiO has a very low electron affinity, which leads to a high potential barrier for electrons at an interface from ZnO to NiO. This improved the stability of the device, which now could endure four times more electrical power. With up to a fourfold increase of current, a threefold increase of emission intensity has been observed at the same voltage level compared to a ITO/ZnO/Al reference. The efficiency could not be improved further with regard to WO_3 devices, despite the fact that electrons are less prone to leaking through in the NiO concept. The higher work function of NiO has been identified as possible reason, which results in an increased barrier from an even higher injection level compared to WO_3, and thereby in reduced carrier injection at the anode. This assumption is supported by the observation of a decreased share of high energetic emission compared to devices with WO_3: reduced blue emission and almost no UV emission are recorded from NiO devices. Again, UV emission could only be detected above 10 V where the device was unstable.

Finally, GaN has been introduced to serve as hole injection layer. This concept provides a little, yet existing electron barrier of about 150 meV. Utilizing the perfect fit of the materials valence band with the valence band of ZnO, efficient hole injection could be proven. Even the devices based on the not optimized p-GaN layers of the first generation already exhibited higher quantum efficiencies than the LEDs discussed before, despite the high resistivity and emission detection threshold voltage. This underlines the fact that valence band fitting has the greatest influence on the injection performance. The latest devices exhibited presumably almost pure ZnO luminescence in the UV spectral range, which has never been observed before without a barrier layer at voltages below 10 V. ZnO NBE emission has already been recordable at the general emission detection threshold of 4.6 V. In comparison with WO_3 and NiO based concepts, GaN/ZnO devices emitted almost pure UV emission from ZnO with only little green-yellow emission, which supposedly originated from the GaN

	Bare ITO	WO_3	NiO	GaN Gen I	GaN Gen II	GaN Gen III
η_{ext}	2.4×10^{-8}	8.1×10^{-8}	7.2×10^{-8}	1.2×10^{-6}	9.3×10^{-6}	3.6×10^{-5}
η_{inj}	1.0×10^{-4}	3.5×10^{-4}	3.1×10^{-4}	1.0 %	8.1 %	31 %
Vis.	4 V	5.5 V	5.5 V	14 V	7.5 V	4.6 V
UV	9 V	10.5 V	8.5 V	17 V	8.5 V	4.6 V

Table 10.1. – External quantum efficiency η_{ext}, estimated injection efficiency η_{inj}, visible and UV emission detection threshold voltage. The efficiency of the NiO device has been estimated from Fig. 7.5d using the efficiency of the bare ITO device and the typical out-coupling efficiency of OLEDs without back-reflecting mirror of 10 %.[95]

layers. With being able to inject directly into the ZnO valence band, this transition is clearly favored by Fermi's Golden Rule due to the much higher density of states in the band. Concrete values for the efficiency of the GaN device were shown which are rarely reported in literature so far. The injection efficiency of the LED could be increased to 31 % after removal of the Ga_2O_3 surface layer, thickness reduction of the ZnO nanoparticle layer, a size selection of nanoparticles by centrifuging, formation of ohmic contacts and high quality p-doping, proving that efficient hole injection into ZnO is possible if the energy levels of the materials fit. External quantum efficiency η_{ext}, injection efficiency η_{inj}, visible emission threshold and UV emission threshold of the different devices have been summed up in Tab. 10.1.

Aside from the injection efficiency, the second challenge is the quantum yield of the ZnO nanoparticles. It has been 0.23 % for the nanoparticles embedded in the LEDs presented here, which is too low for making efficient devices. As answer to this challenge, ZnO quantum dots have been presented exhibiting a superior luminescent quantum yield of up to 60 % for green emission centered around 550 nm to 590 nm. Their superior crystallinity has been proven by x-ray diffraction and high resolution transmission electron microscopy experiments. The emission mechanism has been related to oxygen vacancies and surface OH groups in agreement with reports from literature. It has been shown that reduction of ZnO quantum dot diameter and exposure to ambient air are among the key factors for achieving such a high efficiency. The influence of the quantum dot diameter has been related to two reasons: First, an increased volume density of surface states involved in the green luminescence mechanism, and second, reduced tunneling distance for holes between ZnO states in the volume and surface OH groups. Tunneling of holes from the ZnO valance band to surface OH-groups and from there to oxygen vacancies are regarded to be important

steps of the green radiative recombination process. Photoluminescence experiments in ambient air, nitrogen and vacuum have been conducted to gain information about the influence of the surrounding and especially to underline the importance of OH groups. An additional check by FTIR experiments has been made which clearly demonstrated the reduction of the O-H vibration signal under anaerobic conditions. The presented production method by a nonthermal plasma is a gas phase based process, that provides several advantages over liquid phase processes, which are especially important for industrial mass production: it is easily up-scalable, continuous and allows for synthesis free of ligands. Apart from the application in LEDs, these quantum dots might also be of interest for bio-imaging. The human eye is most sensitive for green color and ZnO is less toxic than traditional chalcogenide semiconductor quantum dots.

A lot of research has been done on ZnO LEDs in the last ten years because of the superior optical properties of the material, which have been underlined again by the development of highly luminescent ZnO quantum dots here. However, the optimism for ZnO LEDs, which has been shown in the beginning of the research activities, has recently changed to a much more skeptical attitude in the scientific community. Many publications of ZnO LEDs have been released without substantial progress being made regarding the key performance measures intensity and efficiency, which have not even been reported most often. Following from the observations made in this work, the greatest challenge for industrial application of ZnO nanoparticle devices is supposed to be the quest for a satisfying hole injection layer. GaN experiments present clearly efficient hole injection into ZnO. While this hole injection layer has been implemented in epitaxial form only, to make full use of the advantages of an inorganic nanoparticle device, all layers will have to be flexible and robust. While GaN is a very stable material in bulk, it is very prone to oxidation of the top most layers which is a serious obstacle for using it in form of loose nanomaterials. Unfortunately, the experiments with different hole injection layers presented here suggest that a good valence band fitting is by far the most important characteristic when choosing an appropriate hole injection layer for ZnO and little compromise can be made on this property. This seriously limits the number of available support materials. Until now and to the best of my knowledge, however, no flexible robust p-conducting material has been presented with a valence band that is close enough to the one of ZnO. Therefore and once again in LED technology, the key for the final breakthrough of a

LED concept will be the successful implementation of a suitable p-conduction layer.

While the road to ZnO devices in every day applications has been proven to be not as easy as it has been hoped for and many research groups have given in, their potential has been demonstrated and substantial and continuous steps forward have been made by the successful development of highly efficient ZnO quantum dots and demonstrating efficient hole injection by p-GaN. Additionally to improving the device performance, by comparing absolute values of the external quantum efficiency and other results from using hole injection materials with very different properties, insights into the relevance of each characteristic for ZnO LEDs have been gained.

A. Appendix

A.1. Characterization methods

A.1.1. ZnO nanoparticles from Evonik Industries and all LEDs

Absorption measurements have been done on the standalone device Shimadzu UV-2550 spectrometer using an integrating sphere. **Photoluminescence** measurements have been carried out on a standard photoluminescence setup. If not stated otherwise, the samples have been excited by the 325 nm line of a HeCd laser (Kimmon IK) and spectra have been recorded by the nitrogen cooled CCD camera Horiba Jobin Yvon Symphony attached to an imaging spectrometer Horiba Jobin Yvon iHR 320 with a 150 nm^{-1} grating. **XRD** diffraction patterns have been collected by Michael Schmitz and Alexander Kompch on a PANalytical X'pert PRO equipped with a 1.6 kW Cu tube at the nanoparticle process technology department at the University of Duisburg-Essen. The topography of TCO substrates has been examined using an Nanosurf Easyscan 2 atomic force microscopy system. The surface roughness S_a has been calculated by the microscope software according to the relation

$$S_a = \frac{1}{MN} \sum_{j,l}^{M,N} |z(x_j, y_l)|. \tag{A.1}$$

Here, z is the measured height at the coordinates x and y with index j and l. M is the number of coordinates measured in x direction, and N in y-direction. **Quantum yields** have been determined in dispersion using a comparative method described in [311]. Samples of different concentrations have been prepared for each material to examine and the absorbance and the PL emission intensity have been measured for each of them together with two reference materials of known quantum yield. The concentration has been kept low in order to prevent reabsorption of emitted photons.

Phosphor	QY	Solvent	$\tilde{n}_{sol}$
Anthracene	27 %[312]	Ethanol	1.36[313]
9,10-diphenylanthracene	90 %[312]	Cyclohexane	1.42[314]
ZnO nanoparticles	2.3×10^{-3}	Ethanol	1.36[313]

Table A.1. – Literature values of quantum yield QY, solvent and solvent refractive indices n_{sol} of the reference phosphors Anthracene and 9,10-diphenylanthracene. The same values are shown for the ZnO nanoparticle sample, with the difference that the QY has been experimentally determined as described in the text.

This results in linear plots of PL emission intensity over absorbance with slope a_x for material x. With these values, the quantum yield has been evaluated by the relation

$$QY_1 = QY_2 \frac{a_1}{a_2} \left(\frac{\tilde{n}_1}{\tilde{n}_2} \right)^2, [311] \tag{A.2}$$

where $\tilde{n}_1$ and $\tilde{n}_2$ are the diffraction indices of the solvent of sample 1 and 2, respectively. The quantum yield of the nanoparticle dispersion has been calculated comparing them with both references and are accepted if the deviation is within the measurement error. Anthracene and 9,10-diphenylanthracene have been used as reference samples for the ZnO nanoparticles because of their similar emission spectra, which cover the UV to blue range (Tab. A.1).

Electroluminescence spectra have been recorded by the Horiba Jobin Yvon Symphony/iHR 320 setup with a $150\,\mathrm{nm}^{-1}$ grating. The anode has been made by pressing a messing bar on the sample positioned on the sample holder and thereby fixating it. It is arranged in a way that the emitting area is visible for the detection setup through a hole. The cathode has been established by using a spring contact probe. The Keitley 2601 SYSTEM SourceMeter has been connected to serve as a voltage source. A lens has been used to project an image of the sample on the entry slit of the spectrometer. This enabled the setup to take images that record the spatial arrangement of the samples light emission when the gratings were turned to reflect the central maxima of zero order onto the camera chip without any diffraction. The electroluminescence spectra have been measured in first order. A Lab View program has been developed on basis of programs shipped along with the devices. It records current and voltage every second, moves the gratings, takes the images and electroluminescence spectra at a predefined center wavelength. The voltage is

increased from a starting to a final value in predefined steps. All recorded spectra have been corrected to account for the wavelength specific characteristics of the setup.

Current-voltage characteristics, electroluminescence emission intensities and external quantum efficiencies have been measured using the Keithley 2601 SourceMeter and spring contact probes. In order to determine the external quantum efficiency, the light emission intensity has been recorded simultaneously by placing the sample on the calibrated silicon photodetector Newport UV-818 connected to the Newport Power Meter 1936-C. Measurements have been controlled by a Lab View program, which has been developed for this task and allowed to set different parameters, including starting and final voltage or current level, step size and time to pass for stabilization after attaining a specific current/voltage level before conducting a measurement. The area of the aluminum contact of the respective sample has been used to calculate (spatially averaged) current densities and emission intensities.

The external quantum efficiency (η_{ext}) of emission with a spectral intensity as function of wavelength $I_{EL}(\lambda)$ has been determined from the current flow through the device I and the current flow I_{EL} through the photo detector as follows. The mean sensitivity $\overline{\gamma_{EL}}$ of the photo detector with given spectral sensitivity dependence $\gamma_{EL}(\lambda)$ has been calculated for the incident spectrum $I_{EL}(\lambda)$ and its normalized form $I_{EL,norm}(\lambda)$ by

$$I_{EL,norm}(\lambda) = \frac{I_{EL}(\lambda)}{\int_{-\infty}^{\infty} I_{EL}(\lambda)}, \tag{A.3}$$

$$\overline{\gamma_{EL}} = \int_{-\infty}^{\infty} \gamma_{EL}(\lambda) I_{EL,norm}(\lambda). \tag{A.4}$$

The total emission intensities I_{EL} and external quantum efficiencies presented here have been calculated according to

$$I_{EL} = \alpha^{-1} \overline{\gamma_{EL}} (I_{ph} - I_d), \tag{A.5}$$

$$\eta_{ext} = n_{ph} n_c^{-1} = \frac{I_{EL}}{hc/\lambda} \left(\frac{I}{e}\right)^{-1} = \frac{\overline{\gamma_{EL}} (I_{ph} - I_d) \lambda e}{hcI}. \tag{A.6}$$

I_{ph} is the current detected from the photodiode in the experiment, I_d is its dark current, n_{ph} and n_c are the counts of photons emitted and charge carriers flowing

through the device, respectively, h is Planck's constant and c is the velocity of light. α is the share of detected photons per emitted photon that is given by the geometry of the setup. With the circular shape of the detector with radius r in mind, and making the assumption of a point source with lambertian intensity profile $I_{EL} = I_{EL,0} \cos\theta$, the relation

$$\alpha = \frac{r^2}{r^2 + \Delta x^2} \tag{A.7}$$

has been evaluated. Here, α is evaluated to be 0.74 using the values of r (0.565 cm) and Δx (≈0.33 cm) of the setup. For a spatially extended light source, the real α will be smaller and $\eta_{ext} \propto \alpha^{-1}$ will therefore be underestimated by using the value of a point source.

A.1.2. ZnO quantum dots from a nonthermal plasma

Special measurement setups have been used to investigate the characteristics of the ZnO quantum dots covered in chapter 9 as most of the work has been done at the high temperature and plasma lab lead by Prof. Uwe Kortshagen at the University of Minnesota.[290]

Quantum yields have been determined by Dr. Jihua Yang and Jens Theis using an absolute method described in detail in [295]. After dispersing the ZnO quantum dots in ethanol inside a nitrogen-filled glove box, measurements have been conducted within the day. The ZnO dispersion has been inserted into an integrating sphere (Labsphere) and has been excited by a UV light-emitting diode (Seti UVTOP-315). The emitted photoluminescence has been detected by a fiber spectrometer (Ocean Optics USB 4000) with a free spectral range of 170 nm to 880 nm. A NIST traceable calibration lamp (Ocean Optics LS-1-CAL) has been used to calibrate its spectral response. All measurements have been averaged over three repetitions in order to improve the accuracy of the experiment.

Photoluminescence spectra of the ZnO quantum dots have been collected on three different setups with setup A being the same one as for quantum yield determination, which has been used to collect the data presented in Fig. 9.6. Here, the ZnO quantum dots have been examined in ethanol dispersions inside a vial which has been filled with nitrogen initially and has been opened during the experiment to expose the sample to ambient air. Setup B has been the stand alone device PTI Quantum

Master 4 Fluorometer, where the spectra of ZnO quantum dots in ethanol which are shown in Fig. 9.3 have been recorded. These two setups have been operated by Dr. Jihua Yang and Jens Theis. For recording of vacuum spectra in setup C, the sample has been drop casted on a silicon substrate and has been excited by the frequency tripled emission line of a Coherent Mira 900 that has been pumped optically by a Coherent Verdi-V10. Frequency tripling has been done by the Photop TP-2000B resulting in an incident excitation beam on the sample mounted within a cryogenic system with a wavelength of 266 nm.

FTIR spectra were collected by Dr. Jihua Yang and Jens Theis using an ALPHA infrared spectrometer (Bruker Optics) in the diffuse reflectance infrared Fourier transform spectroscopy (DRIFTS) mode inside a glove box filled with nitrogen atmosphere. **XRD** measurements were done together with Dr. Jihua Yang and Jens Theis using a Bruker-AXS microdiffractometer with a 2.2 kW sealed Cu x-ray. The quantum dot samples have been exposed to ambient air for several hours before XRD experiments have been performed. **HRTEM** (High resolution transmission electron microscopy) images have been taken by Andrew Wagner in a FEI Tecnai G2 F30 operating at 300 keV. The samples have been prepared by direct deposition of quantum dots on a carbon-coated TEM grid inside the reactor. The images presented have been made from samples which have been exposed to ambient air for one day.

A.2. Simulation of band diagrams and current-voltage-characteristics

Band diagrams and current-voltage characteristics have been simulated one dimensionally with SimWindows version 1.5.0. The simulation is based on a method described in detail in reference [110]. The material parameters employed are summarized in Tab. A.2 and the layer setup of the simulated devices is presented in Tab. A.3. The simulated current-voltage characteristics are shown in Fig. A.1. The band diagrams shown throughout this thesis are depicted over the full simulated range in Fig. A.2 (WO_3/ZnO) and Fig. A.3 (NiO/ZnO and GaN/ZnO).

Material	E_{gap} eV	χ eV	$\epsilon_r(0)$	d nm	N_D/N_A cm^{-3}		μ_n $cm^2V^{-1}s^{-1}$	μ_p $cm^2V^{-1}s^{-1}$	m_n^* m_e	m_p^* m_e
Si	1.12[107]	4.05[107]	11.9[107]	100	p	1×10^{17}	10	0.5	0.2	0.62
Ge	0.66[107]	4[315]	16[107]	100	n	1×10^{17}	10	0.5	0.2	0.62
HTL	5	2	13.18	100	p	1×10^{17}	10	0.5	0.067	0.62
EML	3	4	13.18	10	n	0	10	0.5	0.067	0.62
ETL	5	4	13.18	100	n	1×10^{17}	10	0.5	0.067	0.62
ZnO	3.34[125]	4.2[125]	8[300]	100	n	1×10^{17}	10	0.5	0.28[151]	0.59[151]
WO_3	3.2[265]	6.6[243]	90[253]	5	n	1×10^{17}	10	0.5	0.2	0.62
WO_3 (air)	3.2[265]	5.7[244]	90[253]	5	n	1×10^{17}	10	0.5	0.2	0.62
NiO	3.7[14]	1.8[14]	12[139]	20	p	1×10^{17}	10	0.5	0.2	0.62
GaN	3.4[84]	4.05[84]	9.7[300]	100	p	1×10^{17}	50	20	0.2	0.62

Table A.2. – Parameters used in simulations of band diagrams and current-voltage-characteristics. E_{gap}: band gap, χ: electron affinity, $\epsilon_r(0)$: static relative permittivity, d: layer thickness, N_D/N_A: Donor/acceptor concentration of n-type/p-type layers, respectively, μ_n: electron mobility, μ_p: hole mobility, m_n^* effective electron mass, m_p^* effective hole mass.

Materials	Position of junction(s)	Grid interval	Calculated positions
Si/Ge	100 nm	0 nm to 90 nm 90 nm to 110 nm 110 nm to 200 nm	100 1000 100
HTL/EML/ETL	100 nm and 110 nm	0 nm to 80 nm 80 nm to 130 nm 130 nm to 210 nm	100 1000 100
WO_3/ZnO	5 nm	0 nm to 10 nm 10 nm to 55 nm 55 nm to 105 nm	100 1000 100
NiO/ZnO	20 nm	0 nm to 15 nm 15 nm to 19.99 nm 19.99 nm to 20.01 nm 20.01 nm to 25 nm 25 nm to 120 nm	100 1000 10000 1000 950
GaN/ZnO	100 nm	0 nm to 90 nm 90 nm to 110 nm 110 nm to 200 nm	100 1000 100

Table A.3. – Number of calculated equidistant positions within a grid interval in simulations of the various junctions presented here. Length specifications refer to the distance from the anode contact.

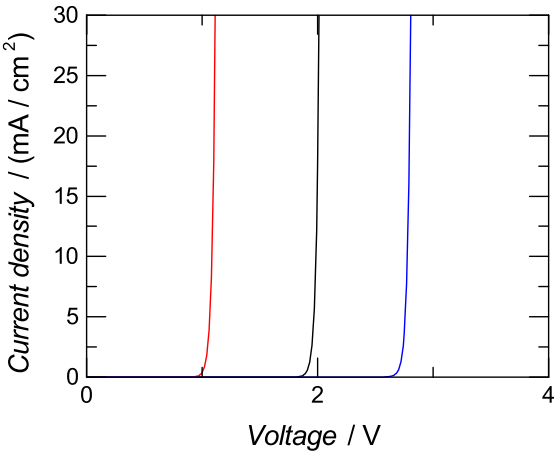

Figure A.1. – Simulation of current density-voltage characteristics of WO_3/ZnO LED (black), air-exposed WO_3/ZnO LED (red), and GaN/ZnO LED (blue).

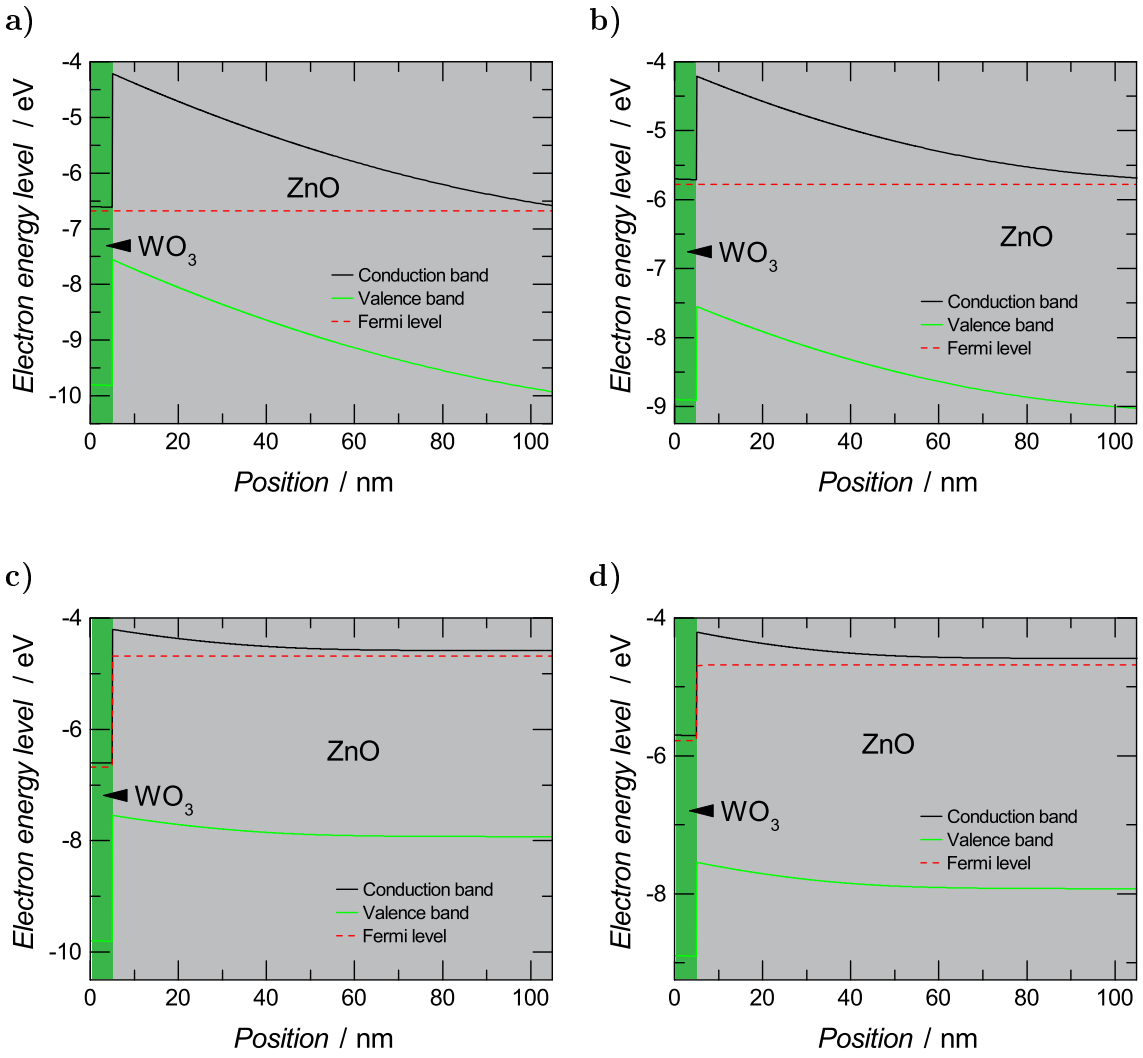

Figure A.2. – Simulation of conduction band level, valence band level, and (quasi) Fermi level of WO_3/ZnO structures shown over complete simulated spatial range; (a) without external bias, (b) WO_3 pre-exposed to air without external bias, (c) at external bias of 2 V and current density of 18 mA/cm^2, (d) WO_3 pre-exposed to air at external bias of 1.1 V and the same current density of 18 mA/cm^2. WO_3 layer has been filled with green and ZnO layer with gray in all figures allowing for quick comparison.

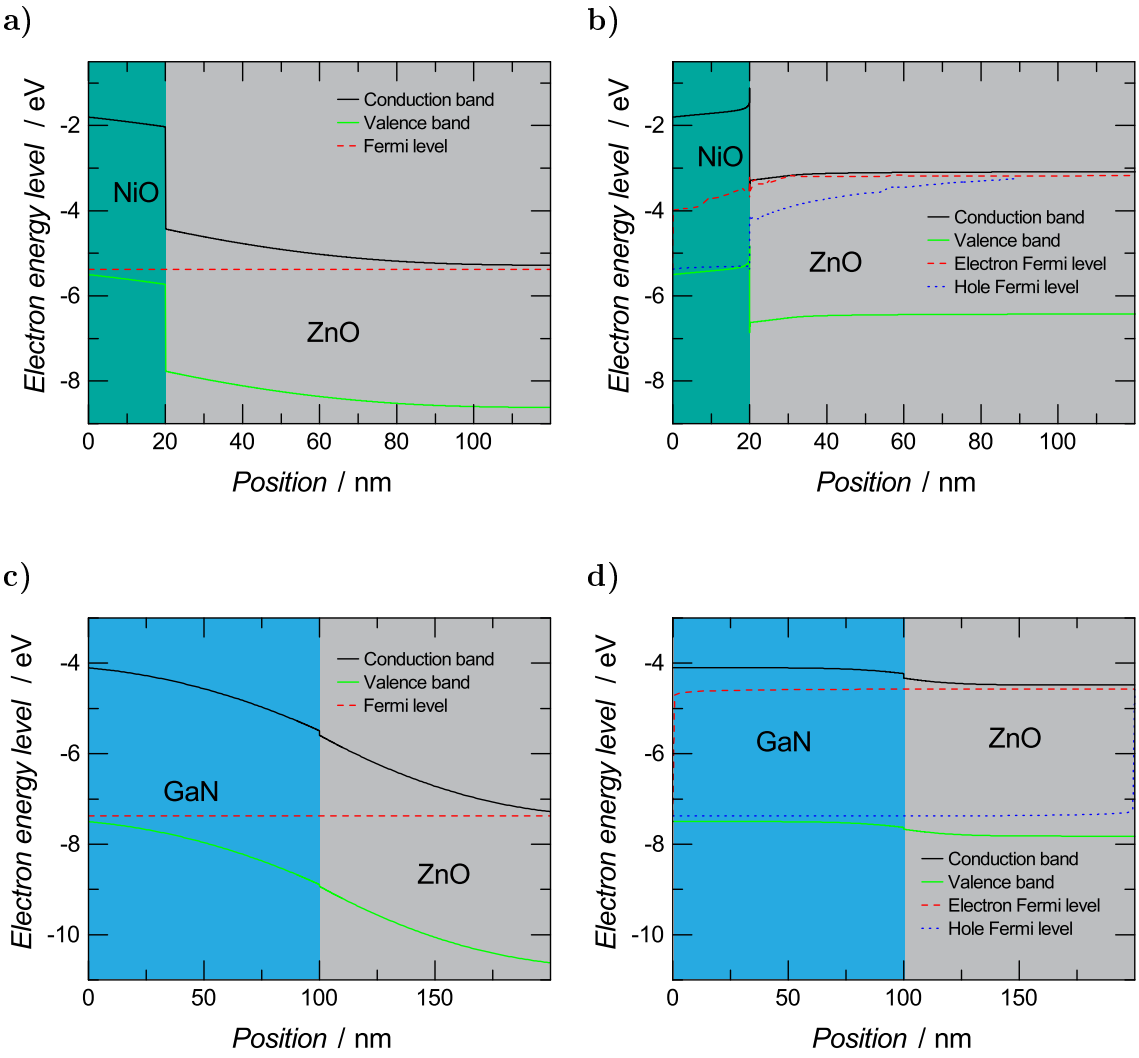

Figure A.3. – Simulation of conduction band level, valence band level, Fermi level (unbiased), electron Fermi level (biased) and quasi hole Fermi level (biased) of NiO/ZnO and GaN/ZnO structures; (a) NiO/ZnO without external bias, (b) NiO/ZnO at external bias of 2.2 V, (c) GaN/ZnO without external bias, (d) GaN/ZnO at external bias of 2.8 V and current density of 23 mA/cm^2. NiO layer has been filled with green-blue, GaN layer with blue and ZnO layer with gray in all figures allowing for quick comparison.

A.3. Supplementary information WO_3/ZnO LEDs

d nm	p_O %	$\dot{m}_{Ar}$ sccm	$\dot{m}_{O2}$ sccm	P_f W	P_r W	t_{pre} min	p_w 10^{-2} mbar	$\dot{d}$ nm/min
2	0	10	0	100	3	15	0.14	1.5
5	0	10	0	100	7	45	1	1.5
20	0	10	0	100	5	45	0.16	1.8
50	0	10	0	100	7	45	1	1.5
5	20	10	2.5	100	6	45	1.4	0.22
5	40	10	6.66	100	6	45	1.4	0.14
5	60	6.66	10	100	6	45	1.6	0.13
5	80	2.5	10	100	5	45	1.4	0.14
5	100	0	10	100	5	45	1.2	0.12

Table A.4. – Sputtering parameters used to fabricate WO_3 layers of different layer thickness d and with different oxygen partial pressures p_O in the sputtering atmosphere during deposition: mass flow of argon $\dot{m}_{Ar}$ and oxygen $\dot{m}_{O2}$, forward power P_f, reflected power P_r, pre-sputtering duration before deposition t_{pre}, working pressure p_w, and deposition rate $\dot{d}$.

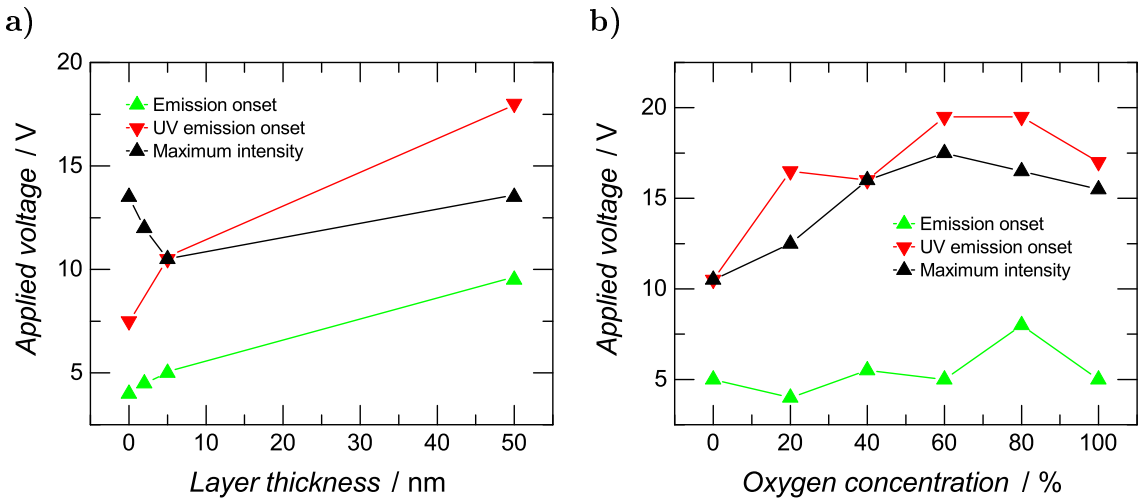

Figure A.4. – Emission onset, UV emission onset and voltage at highest emission intensity of WO_3/ZnO LEDs (a) with different WO_3 layer thickness sputtered in pure argon atmosphere and a reference device without WO_3 layer and (b) 5 nm WO_3 layer thickness sputtered at different oxygen concentrations.

Tab. A.4 gives detailed information on the parameters used for rf-magnetron sputtering deposition of WO_3 layers, and Fig. A.4 shows emission onset, UV emission

onset and voltage at highest emission intensity of the WO_3/ZnO LEDs discussed in chapter 6.

Bibliography

1. Pimputkar, S., Speck, J. S., DenBaars, S. P. & Nakamura, S. "Prospects for LED lighting". *Nat. Photonics* **3,** 180–182. ISSN: 1749-4885 (Apr. 2009).
2. Sekitani, T. *et al.* "Stretchable active-matrix organic light-emitting diode display using printable elastic conductors." *Nat. Mater.* **8,** 494–499. ISSN: 1476-1122 (June 2009).
3. Zheludev, N. "The life and times of the LED — a 100-year history". *Nat. Photonics* **1,** 189–192. ISSN: 1749-4885 (Apr. 2007).
4. Hirayama, H. *et al.* "222-282 nm AlGaN and InAlGaN-based deep-UV LEDs fabricated on high-quality AlN on sapphire". *Phys. Status Solidi* **206,** 1176–1182. ISSN: 18626300 (June 2009).
5. Sandhu, A. "The future of ultraviolet LEDs". *Nat. Photonics* **1,** 38. ISSN: 1749-4885 (Jan. 2007).
6. Schlotter, P. *et al.* "Fabrication and characterization of GaN/InGaN/AlGaN double heterostructure LEDs and their application in luminescence conversion LEDs". *Mater. Sci. Eng. B* **59,** 390–394. ISSN: 09215107 (May 1999).
7. Laubsch, A., Sabathil, M., Baur, J., Peter, M. & Hahn, B. "High-Power and High-Efficiency InGaN-Based Light Emitters". *IEEE Trans. Electron Devices* **57,** 79–87. ISSN: 0018-9383 (Jan. 2010).
8. Breschi, L. *et al.* "Polymerization kinetics of dental adhesives cured with LED: correlation between extent of conversion and permeability." *Dent. Mater.* **23,** 1066–1072. ISSN: 0109-5641 (Sept. 2007).
9. Geffroy, B., le Roy, P. & Prat, C. "Organic light-emitting diode (OLED) technology: materials, devices and display technologies". *Polym. Int.* **55,** 572–582. ISSN: 0959-8103 (June 2006).

10. Forrest, S. R. "The path to ubiquitous and low-cost organic electronic appliances on plastic." *Nature* **428,** 911–918. ISSN: 1476-4687 (Apr. 2004).

11. Berntsen, A. *et al.* "Stability of polymer LEDs". *Opt. Mater. (Amst).* **9,** 125–133. ISSN: 09253467 (Jan. 1998).

12. Zhang, D.-D. *et al.* "Realizing both improved luminance and stability in organic light-emitting devices based on a solution-processed inter-layer composed of MoOX and Au nanoparticles mixture". *Org. Electron.* **15,** 961–967. ISSN: 15661199 (Apr. 2014).

13. Yu, S.-Y., Chang, J.-H., Wang, P.-S., Wu, C.-I. & Tao, Y.-T. "Effect of ITO surface modification on the OLED device lifetime." *Langmuir* **30,** 7369–7376. ISSN: 1520-5827 (July 2014).

14. Caruge, J. M., Halpert, J. E., Wood, V., Bulović, V. & Bawendi, M. G. "Colloidal quantum-dot light-emitting diodes with metal-oxide charge transport layers". *Nat. Photonics* **2,** 247–250. ISSN: 1749-4885 (Mar. 2008).

15. Kim, T.-H. *et al.* "Full-colour quantum dot displays fabricated by transfer printing". *Nat. Photonics* **5,** 176–182. ISSN: 1749-4885 (Feb. 2011).

16. Wood, V. *et al.* "Air-stable operation of transparent, colloidal quantum dot based LEDs with a unipolar device architecture." *Nano Lett.* **10,** 24–29. ISSN: 1530-6992 (Jan. 2010).

17. Wood, V. *et al.* "Electroluminescence from nanoscale materials via field-driven ionization." *Nano Lett.* **11,** 2927–2932. ISSN: 1530-6992 (July 2011).

18. Mashford, B. S. *et al.* "High-efficiency quantum-dot light-emitting devices with enhanced charge injection". *Nat. Photonics* **7,** 407–412. ISSN: 1749-4885 (Apr. 2013).

19. Wood, V. *et al.* "Selection of metal oxide charge transport layers for colloidal quantum dot LEDs". *ACS Nano* **3,** 3581–3586. ISSN: 1936-086X (Nov. 2009).

20. Cassette, E. *et al.* "Synthesis and Characterization of Near-Infrared Cu-In-Se/ZnS Core/Shell Quantum Dots for In vivo Imaging". *Chem. Mater.* **22,** 6117–6124. ISSN: 0897-4756 (Nov. 2010).

21. Aoki, T., Hatanaka, Y. & Look, D. C. "ZnO diode fabricated by excimer-laser doping". *Appl. Phys. Lett.* **76,** 3257–3258. ISSN: 00036951 (2000).

22. Ou, Q., Matsuda, T., Mesko, M., Ogino, A. & Nagatsu, M. "Cathodoluminescence Property of ZnO Nanophosphors Prepared by Laser Ablation". *Jpn. J. Appl. Phys.* **47,** 389–393. ISSN: 0021-4922 (Jan. 2008).

23. Matsuyama, K., Mishima, K., Kato, T., Irie, K. & Mishima, K. "Transparent polymeric hybrid film of ZnO nanoparticle quantum dots and PMMA with high luminescence and tunable emission color." *J. Colloid Interface Sci.* **367,** 171–177. ISSN: 1095-7103 (Feb. 2012).

24. Tang, X., Choo, E. S. G., Li, L., Ding, J. & Xue, J. "Synthesis of ZnO Nanoparticles with Tunable Emission Colors and Their Cell Labeling Applications". *Chem. Mater.* **22,** 3383–3388. ISSN: 0897-4756 (June 2010).

25. Alivov, Y. I. *et al.* "Fabrication and characterization of n-ZnO/p-AlGaN heterojunction light-emitting diodes on 6H-SiC substrates". *Appl. Phys. Lett.* **83,** 4719–4721. ISSN: 00036951 (2003).

26. Ling, B. *et al.* "Color tunable light-emitting diodes based on p-Si/p-CuAlO/n-ZnO nanorod array heterojunctions". *Appl. Phys. Lett.* **97,** 013101. ISSN: 00036951 (2010).

27. Zhang, L. *et al.* "Improvement of UV electroluminescence of n- ZnO / p-GaN heterojunction LED by ZnS interlayer". *Opt. Express* **21,** 1613–1617 (2013).

28. Guo, R. *et al.* "Electroluminescence from ZnO nanowire-based p-GaN/n-ZnO heterojunction light-emitting diodes". *Appl. Phys. B* **94,** 33–38. ISSN: 0946-2171 (Nov. 2008).

29. Ke, M.-Y. *et al.* "UV light emission from GZO/ZnO/GaN heterojunction diodes with carrier confinement layers." *Opt. Express* **17,** 22912–22917. ISSN: 1094-4087 (Dec. 2009).

30. Rogers, D. J. *et al.* "Electroluminescence at 375 nm from a ZnO/GaN:Mg/c-Al2O3 heterojunction light emitting diode". *Appl. Phys. Lett.* **88,** 141918. ISSN: 00036951 (2006).

31. Hassan, J. *et al.* "Fabrication of ZnO nanorod/p-GaN high-brightness UV LED by microwave-assisted chemical bath deposition with Zn(OH)2-PVA nanocomposites as seed layer". *Opt. Mater. (Amst).* **35,** 1035–1041. ISSN: 09253467 (Mar. 2013).

32. Sun, J. W. *et al.* "Excitonic electroluminescence from ZnO-based heterojunction light emitting diodes". *J. Phys. D. Appl. Phys.* **41,** 155103. ISSN: 0022-3727 (Aug. 2008).

33. Jha, S. K. *et al.* "ZnO-nanorod-array/p-GaN high-performance ultra-violet light emitting devices prepared by simple solution synthesis". *Appl. Phys. Lett.* **101,** 211116. ISSN: 00036951 (2012).

34. Alivov, Y. I., Van Nostrand, J. E., Look, D. C., Chukichev, M. V. & Ataev, B. M. "Observation of 430 nm electroluminescence from ZnO/GaN heterojunction light-emitting diodes". *Appl. Phys. Lett.* **83,** 2943–2945. ISSN: 00036951 (2003).

35. Bie, Y.-Q. *et al.* "Single ZnO nanowire/p-type GaN heterojunctions for photovoltaic devices and UV light-emitting diodes." *Adv. Mater.* **22,** 4284–4287. ISSN: 1521-4095 (Oct. 2010).

36. Hwang, D.-K. *et al.* "p-ZnO/n-GaN heterostructure ZnO light-emitting diodes". *Appl. Phys. Lett.* **86,** 222101. ISSN: 00036951 (2005).

37. Chen, C. W. *et al.* "Nonpolar light emitting diode made by m-plane n-ZnO/p-GaN heterostructure". *Opt. Mater. Express* **1,** 1555–1560. ISSN: 2159-3930 (Nov. 2011).

38. Chen, C.-H. *et al.* "Electroluminescence from n-ZnO nanowires/p-GaN heterostructure light-emitting diodes". *Appl. Phys. Lett.* **95,** 223101. ISSN: 00036951 (2009).

39. Chen, H.-C. *et al.* "UV Electroluminescence and Structure of n-ZnO/p-GaN Heterojunction LEDs Grown by Atomic Layer Deposition". *IEEE J. Quantum Electron.* **46,** 265–271. ISSN: 0018-9197 (Feb. 2010).

40. Chen, M.-J. *et al.* "Structure and Ultraviolet Electroluminescence of ZnO/SiO2-ZnO Nanocomposite/p-GaN Heterostructure". *IEEE Trans. Electron Devices* **57,** 2195–2202. ISSN: 0018-9383 (Sept. 2010).

41. Chen, X. *et al.* "ZnO nanorod/GaN light-emitting diodes: The origin of yellow and violet emission bands under reverse and forward bias". *J. Appl. Phys.* **110,** 094513. ISSN: 00218979 (2011).

42. Ding, M., Zhao, D., Yao, B., Zhao, B. & Xu, X. "High brightness light emitting diode based on single ZnO microwire". *Chem. Phys. Lett.* **577,** 88–91. ISSN: 00092614 (July 2013).

43. Fang, F., Zhao, D., Li, B., Zhang, Z. & Shen, D. "Hydrogen effects on the electroluminescence of n-ZnO nanorod/p-GaN film heterojunction light-emitting diodes." *Phys. Chem. Chem. Phys.* **12,** 6759–6762. ISSN: 1463-9084 (July 2010).

44. Fu, H.-K., Cheng, C.-L., Wang, C.-H., Lin, T.-Y. & Chen, Y.-F. "Selective Angle Electroluminescence of Light-Emitting Diodes based on Nanostructured ZnO/GaN Heterojunctions". *Adv. Funct. Mater.* **19,** 3471–3475. ISSN: 1616301X (Nov. 2009).

45. Han, W. S., Kim, Y. Y., Kong, B. H. & Cho, H. K. "Ultraviolet light emitting diode with n-ZnO:Ga/i-ZnO/p-GaN:Mg heterojunction". *Thin Solid Films* **517,** 5106–5109. ISSN: 00406090 (July 2009).

46. Herng, T. S. *et al.* "Ferromagnetic Cu doped ZnO as an electron injector in heterojunction light emitting diodes". *J. Appl. Phys.* **104,** 103104. ISSN: 00218979 (2008).

47. Hwang, S.-H., Chung, T.-H. & Lee, B.-T. "Study on the interfacial layer in ZnO/GaN heterostructure light-emitting diode". *Mater. Sci. Eng. B* **157,** 32–35. ISSN: 09215107 (Feb. 2009).

48. Jeong, M.-C., Oh, B.-Y., Ham, M.-H., Lee, S.-W. & Myoung, J.-M. "ZnO-nanowire-inserted GaN/ZnO heterojunction light-emitting diodes." *Small* **3,** 568–572. ISSN: 1613-6829 (Apr. 2007).

49. Jha, S., Kutsay, O., Bello, I. & Lee, S. "ZnO nanorod based low turn-on voltage LEDs with wide electroluminescence spectra". *J. Lumin.* **133,** 222–225. ISSN: 00222313 (Jan. 2013).

50. Jha, S. *et al.* "Violet-blue LEDs based on p-GaN/n-ZnO nanorods and their stability." *Nanotechnology* **22,** 245202. ISSN: 1361-6528 (June 2011).

51. Lee, J. Y. *et al.* "A study on the origin of emission of the annealed n-ZnO/p-GaN heterostructure LED". *Thin Solid Films* **517,** 5157–5160. ISSN: 00406090 (July 2009).

52. Lee, S.-D., Kim, Y.-S., Yi, M.-S., Choi, J.-Y. & Kim, S.-W. "Morphology Control and Electroluminescence of ZnO Nanorod/GaN Heterojunctions Prepared Using Aqueous Solution". *J. Phys. Chem. C* **113,** 8954–8958. ISSN: 1932-7447 (May 2009).

53. Lee, S. & Kim, D. Y. "Characteristics of ZnO/GaN heterostructure formed on GaN substrate by sputtering deposition of ZnO". *Mater. Sci. Eng. B* **137,** 80–84. ISSN: 09215107 (Feb. 2007).

54. Li, S. *et al.* "Ultraviolet/violet dual-color electroluminescence based on n-ZnO single crystal/p-GaN direct-contact light-emitting diode". *J. Lumin.* **140,** 110–113. ISSN: 00222313 (Aug. 2013).

55. Li, X. *et al.* "Saturated blue-violet electroluminescence from single ZnO micro/nanowire and p-GaN film hybrid light-emitting diodes". *Appl. Phys. Lett.* **102,** 221103. ISSN: 00036951 (2013).

56. Liu, W. Z. *et al.* "Localized surface plasmon-enhanced ultraviolet electroluminescence from n-ZnO/i-ZnO/p-GaN heterojunction light-emitting diodes via optimizing the thickness of MgO spacer layer". *Appl. Phys. Lett.* **101,** 142101. ISSN: 00036951 (2012).

57. Lupan, O. *et al.* "Comparative study of the ZnO and Zn1-xCdxO nanorod emitters hydrothermally synthesized and electrodeposited on p-GaN". *Appl. Surf. Sci.* **259,** 399–405. ISSN: 01694332 (Oct. 2012).

58. Lupan, O., Pauporté, T. & Viana, B. "Low-voltage UV-electroluminescence from ZnO-nanowire Array/p-GaN light-emitting diodes." *Adv. Mater.* **22,** 3298–3302. ISSN: 1521-4095 (Aug. 2010).

59. Mo, X. *et al.* "Near-ultraviolet light-emitting diodes realized from n-ZnO nanorod/p-GaN direct-bonding heterostructures". *J. Lumin.* **137,** 116–120. ISSN: 00222313 (May 2013).

60. Murai, A. *et al.* "Light-Emitting Diode Based on ZnO and GaN Direct Wafer Bonding". *Jpn. J. Appl. Phys.* **45,** L1045–L1047. ISSN: 0021-4922 (Sept. 2006).

61. Ng, A. M. *et al.* "GaN/ZnO nanorod light emitting diodes with different emission spectra." *Nanotechnology* **20,** 445201. ISSN: 1361-6528 (Nov. 2009).

62. Ng, A. M. C. *et al.* "Solution-based growth of ZnO nanorods for light-emitting devices: hydrothermal vs. electrodeposition". *Appl. Phys. B* **100,** 851–858. ISSN: 0946-2171 (Aug. 2010).

63. Qi, Q. *et al.* "Electroluminescence of an n-ZnO/p-GaN Heterojunction under Forward and Reverse Biases". *Chinese Phys. Lett.* **22,** 2298–2301. ISSN: 0256-307X (Sept. 2005).

64. Qiao, Q. *et al.* "Surface plasmon enhanced ultraviolet light-emitting devices". *J. Lumin.* **134,** 754–757. ISSN: 00222313 (Feb. 2013).

65. Shi, Z. *et al.* "High-performance ultraviolet-blue light-emitting diodes based on an n-ZnO nanowall networks/p-GaN heterojunction". *Appl. Phys. Lett.* **103,** 021109. ISSN: 00036951 (2013).

66. Wu, J.-H. *et al.* "The influence of ZnO seed layers on n-ZnO nanostructure/p-GaN LEDs". *Appl. Phys. A* **109,** 489–495. ISSN: 0947-8396 (July 2012).

67. Xu, S. *et al.* "Ordered nanowire array blue/near-UV light emitting diodes." *Adv. Mater.* **22,** 4749–4753. ISSN: 1521-4095 (Nov. 2010).

68. Yang, H. S. *et al.* "Fabrication of Hybrid n-ZnMgO/ n-ZnO/ p-AlGaN/ p-GaN Light-Emitting Diodes". *Jpn. J. Appl. Phys.* **44,** 7296–7300. ISSN: 0021-4922 (Oct. 2005).

69. Yang, T. *et al.* "Room temperature electroluminescence from the n-ZnO/p-GaN heterojunction device grown by MOCVD". *Mater. Res. Bull.* **43,** 3614–3620. ISSN: 00255408 (Dec. 2008).

70. You, J. B. *et al.* "Improved electroluminescence from n-ZnO/AlN/p-GaN heterojunction light-emitting diodes". *Appl. Phys. Lett.* **96,** 201102. ISSN: 00036951 (2010).

71. Zhang, S. G. *et al.* "Localized surface plasmon-enhanced electroluminescence from ZnO-based heterojunction light-emitting diodes". *Appl. Phys. Lett.* **99,** 181116. ISSN: 00036951 (2011).

72. Zhang, X.-M., Lu, M.-Y., Zhang, Y., Chen, L.-J. & Wang, Z. L. "Fabrication of a High-Brightness Blue-Light-Emitting Diode Using a ZnO-Nanowire Array Grown on p-GaN Thin Film". *Adv. Mater.* **21,** 2767–2770. ISSN: 09359648 (July 2009).

73. Alivov, Y. *et al.* "Forward-current electroluminescence from GaN/ZnO double heterostructure diode". *Solid. State. Electron.* **49,** 1693–1696. ISSN: 00381101 (Oct. 2005).

74. Alvi, N. H., Riaz, M., Tzamalis, G., Nur, O. & Willander, M. "Fabrication and characterization of high-brightness light emitting diodes based on n-ZnO nanorods grown by a low-temperature chemical method on p-4H-SiC and p-GaN". *Semicond. Sci. Technol.* **25,** 065004. ISSN: 0268-1242 (June 2010).

75. Alvi, N., Riaz, M., Tzamalis, G., Nur, O. & Willander, M. "Junction temperature in n-ZnO nanorods/(p-4H–SiC, p-GaN, and p-Si) heterojunction light emitting diodes". *Solid. State. Electron.* **54,** 536–540. ISSN: 00381101 (May 2010).

76. Alvi, N., Willander, M. & Nur, O. "The effect of the post-growth annealing on the electroluminescence properties of n-ZnO nanorods/p-GaN light emitting diodes". *Superlattices Microstruct.* **47,** 754–761. ISSN: 07496036 (June 2010).

77. Alvi, N. U. H., Hussain, S., Jensen, J., Nur, O. & Willander, M. "Influence of helium-ion bombardment on the optical properties of ZnO nanorods/p-GaN light-emitting diodes." *Nanoscale Res. Lett.* **6,** 628. ISSN: 1556-276X (Jan. 2011).

78. Chang, S., Chuang, R., Chang, S., Chiou, Y. & Lu, C. "MBE n-ZnO/MOCVD p-GaN heterojunction light-emitting diode". *Thin Solid Films* **517,** 5054–5056. ISSN: 00406090 (July 2009).

79. Chen, Y. *et al.* "Ultraviolet electroluminescence from hybrid inorganic/organic ZnO/GaN/poly(3-hexylthiophene) dual heterojunctions." *Opt. Express* **19 Suppl 3,** A319–325. ISSN: 1094-4087 (May 2011).

80. Hong, Y. J. *et al.* "Structural and optical characteristics of GaN/ZnO coaxial nanotube heterostructure arrays for light-emitting device applications". *New J. Phys.* **11,** 125021. ISSN: 1367-2630 (Dec. 2009).

81. Kong, B. H., Han, W. S., Kim, Y. Y., Cho, H. K. & Kim, J. H. "Heterojunction light emitting diodes fabricated with different n-layer oxide structures on p-GaN layers by magnetron sputtering". *Appl. Surf. Sci.* **256,** 4972–4976. ISSN: 01694332 (June 2010).

82. Lee, C.-H. *et al.* "GaN/ZnO Nanotube Heterostructure Light-Emitting Diodes Fabricated on Si". *IEEE J. Sel. Top. Quantum Electron.* **17,** 966–970. ISSN: 1077-260X (July 2011).

83. Sadaf, J. R., Israr, M. Q., Kishwar, S., Nur, O. & Willander, M. "Forward- and reverse-biased electroluminescence behavior of chemically fabricated ZnO nanotubes/GaN interface". *Semicond. Sci. Technol.* **26,** 075003. ISSN: 0268-1242 (July 2011).

84. Titkov, I. *et al.* "ZnO/GaN heterostructure for LED applications". *J. Mod. Opt.* **56,** 653–660. ISSN: 0950-0340 (Mar. 2009).

85. Willander, M. *et al.* "Luminescence from Zinc Oxide Nanostructures and Polymers and their Hybrid Devices". *Materials (Basel).* **3,** 2643–2667. ISSN: 1996-1944 (Apr. 2010).

86. Huang, H. *et al.* "Improved and orange emission from an n-ZnO/p-Si heterojunction light emitting device with NiO as the intermediate layer". *Appl. Phys. Lett.* **101,** 223504. ISSN: 00036951 (2012).

87. Deng, R. *et al.* "Ultraviolet electroluminescence from n-ZnO/p-NiO heterojunction light-emitting diode". *J. Lumin.* **134,** 240–243. ISSN: 00222313 (Feb. 2013).

88. Wang, J.-Y. *et al.* "Double side electroluminescence from p-NiO/n-ZnO nanowire heterojunctions". *Appl. Phys. Lett.* **95,** 131117. ISSN: 00036951 (2009).

89. Jung, B. O., Kwon, Y. H., Seo, D. J., Lee, D. S. & Cho, H. K. "Ultraviolet light emitting diode based on p-NiO/n-ZnO nanowire heterojunction". *J. Cryst. Growth* **370,** 314–318. ISSN: 00220248 (May 2013).

90. Long, H. *et al.* "Ultraviolet electroluminescence from ZnO/NiO-based heterojunction light-emitting diodes". *Appl. Phys. Lett.* **95,** 013509. ISSN: 00036951 (2009).

91. Ye, J. D. *et al.* "Electroluminescent and transport mechanisms of n-ZnO/p-Si heterojunctions". *Appl. Phys. Lett.* **88,** 182112. ISSN: 00036951 (2006).

92. Hsieh, Y.-P. *et al.* "Electroluminescence from ZnO/Si-nanotips light-emitting diodes." *Nano Lett.* **9,** 1839–1843. ISSN: 1530-6992 (May 2009).

93. Nannen, E., Kümmell, T., Ebbers, A. & Bacher, G. "p-Si/n-ZnO Nanocrystal Heterojunction Light Emitting Device". *Appl. Phys. Express* **5,** 035001. ISSN: 1882-0778 (Feb. 2012).

94. Ohta, H., Orita, M., Hirano, M. & Hosono, H. "Fabrication and characterization of ultraviolet-emitting diodes composed of transparent p-n heterojunction, p-SrCu2O2 and n-ZnO". *J. Appl. Phys.* **89,** 5720–5725. ISSN: 00218979 (2001).

95. Riedel, B. *Effizienzsteigerung in organischen Leuchtdioden.* PhD thesis (KIT, 2011).

96. Yang, Q., Wang, W., Xu, S. & Wang, Z. L. "Enhancing light emission of ZnO microwire-based diodes by piezo-phototronic effect." *Nano Lett.* **11,** 4012–4017. ISSN: 1530-6992 (Sept. 2011).

97. Nannen, E. *All-Inorganic White Light Emitting Devices Based on ZnO Nanocrystals.* PhD thesis (Duisburg, 2012).

98. Boix, P. P., Ajuria, J., Pacios, R. & Garcia-Belmonte, G. "Carrier recombination losses in inverted polymer: Fullerene solar cells with ZnO hole-blocking layer from transient photovoltage and impedance spectroscopy techniques". *J. Appl. Phys.* **109,** 074514. ISSN: 00218979 (2011).

99. Manor, A., Katz, E. A., Tromholt, T. & Krebs, F. C. "Enhancing functionality of ZnO hole blocking layer in organic photovoltaics". *Sol. Energy Mater. Sol. Cells* **98,** 491–493. ISSN: 09270248 (Mar. 2012).

100. Lim, D. C. *et al.* "Spontaneous formation of nanoripples on the surface of ZnO thin films as hole-blocking layer of inverted organic solar cells". *Sol. Energy Mater. Sol. Cells* **95,** 3036–3040. ISSN: 09270248 (July 2011).

101. Robertson, J. & Clark, S. J. "Limits to doping in oxides". *Phys. Rev. B* **83,** 075205. ISSN: 1098-0121 (Feb. 2011).

102. Fu, Y.-S. *et al.* "Stable aqueous dispersion of ZnO quantum dots with strong blue emission via simple solution route." *J. Am. Chem. Soc.* **129,** 16029–16033. ISSN: 1520-5126 (Dec. 2007).

103. Stipan, K. *et al.* US Patent 7,718,261 B2 (2010).

104. Kleinwechter, H., Janzen, C., Knipping, J., Wiggers, H. & Roth, P. "Formation and properties of ZnO nano-particles from gas phase synthesis processes". *J. Mater. Sci.* **37,** 4349–4360 (2002).

105. Polarz, S. *et al.* "Chemical vapor synthesis of size-selected zinc oxide nanoparticles." *Small* **1,** 540–552. ISSN: 1613-6829 (May 2005).

106. Ali, M., Friedenberger, N., Spasova, M. & Winterer, M. "A Novel Approach for Chemical Vapor Synthesis of ZnO Nanocrystals: Optimization of Yield, Crystallinity". *Chem. Vap. Depos.* **15,** 192–198. ISSN: 09481907 (Sept. 2009).

107. Sze, S. M. & Ng, K. K. *Physics of Semiconductor Devices* Third Edit. ISBN: 978-0-471-14323-9 (John Wiley & Sons, Inc., New jersey, 2007).

108. Anderson, R. "Experiments on Ge-GaAs heterojunctions". *Solid. State. Electron.* **5,** 341–351. ISSN: 00381101 (Sept. 1962).

109. Yan, D., Wang, H. & Du, B. *Introduction to organic semiconductor heterojunctions.* ISBN: 9780470825952 (John Wiley & Sons (Asia) Pte Ltd., 2010).

110. Winston, D. W. *Physical simulation of optoelectronic semiconductor devices.* PhD thesis (University of Colorado, 1996).

111. Horio, K. & Yanai, H. "Numerical modeling of heterojunctions including the thermionic emission mechanism at the heterojunction interface". *IEEE Trans. Electron Devices* **37,** 1093–1098. ISSN: 00189383 (Apr. 1990).

112. Berz, F. "The Bethe condition for thermionic emission near an absorbing boundary". *Solid. State. Electron.* **28,** 1007–1013. ISSN: 00381101 (Oct. 1985).

113. Thornber, K. K. "Relation of drift velocity to low-field mobility and high-field saturation velocity". *J. Appl. Phys.* **51,** 2127–2136. ISSN: 00218979 (1980).

114. Shah, J. M., Li, Y., Gessmann, T. & Fred Schubert, E. "Experimental Analysis and a New Theoretical Model for Anomalously High Ideality Factors (n » 2.0) in GaN-based p-n Junction Diodes". *MRS Proc.* **798,** Y7.11. ISSN: 1946-4274 (Feb. 2011).

115. Schubert, E. *Light-emitting Diodes* Second edi. ISBN: 978-0-521-86538-8 (Cambridge University Press, New York, 2006).

116. Serevicius, T., Miasojedovas, S., Gavryushin, V. & Jursenas, S. "Luminescence of ZnO crystals under surface and bulk excitation regimes". *Phys. status solidi* **6,** 2671–2673. ISSN: 18626351 (Dec. 2009).

117. DenBaars, S. P. *et al.* "Development of gallium-nitride-based light-emitting diodes (LEDs) and laser diodes for energy-efficient lighting and displays". *Acta Mater.* **61,** 945–951. ISSN: 13596454 (Feb. 2013).

118. Chen, P., Ma, X. & Yang, D. "Fairly pure ultraviolet electroluminescence from ZnO-based light-emitting devices". *Appl. Phys. Lett.* **89,** 111112. ISSN: 00036951 (2006).

119. Goldenberg, B., Zook, J. D. & Ulmer, R. J. "Ultraviolet and violet light-emitting GaN diodes grown by low-pressure metalorganic chemical vapor deposition". *Appl. Phys. Lett.* **62,** 381–383. ISSN: 00036951 (1993).

120. Hwang, D.-K., Oh, M.-S., Lim, J.-H., Choi, Y.-S. & Park, S.-J. "ZnO-based light-emitting metal-insulator-semiconductor diodes". *Appl. Phys. Lett.* **91,** 121113. ISSN: 00036951 (2007).

121. Maruska, H. & Stevenson, D. "Mechanism of light production in metal-insulator-semiconductor diodes; GaN:Mg violet light-emitting diodes". *Solid. State. Electron.* **17,** 1171–1179. ISSN: 00381101 (Nov. 1974).

122. Wang, H.-T. *et al.* "Band-edge electroluminescence from N+ implanted bulk ZnO". *Appl. Phys. Lett.* **88,** 102107. ISSN: 00036951 (2006).

123. Artemyev, M. V., Sperling, V. & Woggon, U. "Electroluminescence in thin solid films of closely packed CdS nanocrystals". *J. Appl. Phys.* **81,** 6975–6977. ISSN: 00218979 (1997).

124. Adachi, D., Hama, T., Toyama, T. & Okamoto, H. "Electroluminescent properties of chemically synthesized zinc sulfide nanocrystals doped with manganese". *J. Mater. Sci. Mater. Electron.* **20,** 130–133. ISSN: 0957-4522 (Nov. 2007).

125. Aleshin, A. N., Shcherbakov, I. P., Petrov, V. N. & Titkov, A. N. "Solution-processed polyfluorene–ZnO nanoparticles ambipolar light-emitting field-effect transistor". *Org. Electron.* **12,** 1285–1292. ISSN: 15661199 (Aug. 2011).

126. Aleshin, A. N. & Shcherbakov, I. P. "A light-emitting field-effect transistor based on a polyfluorene–ZnO nanoparticles film". *J. Phys. D. Appl. Phys.* **43,** 315104. ISSN: 0022-3727 (Aug. 2010).

127. Cicoira, F. & Santato, C. "Organic Light Emitting Field Effect Transistors: Advances and Perspectives". *Adv. Funct. Mater.* **17,** 3421–3434. ISSN: 1616301X (Nov. 2007).

128. Hepp, A. *et al.* "Light-Emitting Field-Effect Transistor Based on a Tetracene Thin Film". *Phys. Rev. Lett.* **91,** 157406. ISSN: 0031-9007 (Oct. 2003).

129. Walters, R. J., Bourianoff, G. I. & Atwater, H. A. "Field-effect electroluminescence in silicon nanocrystals." *Nat. Mater.* **4,** 143–146. ISSN: 1476-1122 (Feb. 2005).

130. Hines, M. A. & Guyot-Sionnest, P. "Synthesis and Characterization of Strongly Luminescing ZnS-Capped CdSe Nanocrystals". *J. Phys. Chem.* **100,** 468–471. ISSN: 0022-3654 (Jan. 1996).

131. Peng, X., Schlamp, M. C., Kadavanich, A. V. & Alivisatos, A. P. "Epitaxial Growth of Highly Luminescent CdSe/CdS Core/Shell Nanocrystals with Photostability and Electronic Accessibility". *J. Am. Chem. Soc.* **119,** 7019–7029. ISSN: 0002-7863 (July 1997).

132. Dabbousi, B. O. *et al.* "(CdSe)ZnS Core - Shell Quantum Dots: Synthesis and Characterization of a Size Series of Highly Luminescent Nanocrystallites". *J. Phys. Chem. B* **101,** 9463–9475. ISSN: 1520-6106 (Nov. 1997).

133. Williams, E. L., Haavisto, K., Li, J. & Jabbour, G. E. "Excimer-Based White Phosphorescent Organic Light-Emitting Diodes with Nearly 100 % Internal Quantum Efficiency". *Adv. Mater.* **19,** 197–202. ISSN: 09359648 (Jan. 2007).

134. Chen, L.-C. *et al.* "Oxidized Ni/Pt and Ni/Au ohmic contacts to p-type GaN". *Appl. Phys. Lett.* **76,** 3703–3705. ISSN: 00036951 (2000).

135. Ho, J.-K. *et al.* "Low-resistance ohmic contacts to p-type GaN". *Appl. Phys. Lett.* **74,** 1275–1277. ISSN: 00036951 (1999).

136. Jang, H. W., Kim, S. Y. & Lee, J.-L. "Mechanism for Ohmic contact formation of oxidized Ni/Au on p-type GaN". *J. Appl. Phys.* **94,** 1748–1752. ISSN: 00218979 (2003).

137. Qiao, D. *et al.* "A study of the Au/Ni ohmic contact on p-GaN". *J. Appl. Phys.* **88,** 4196–4200. ISSN: 00218979 (2000).

138. Wang, P., Cao, B., Gan, Z. & Liu, S. "Analysis of light extraction efficiency of GaN-based light-emitting diodes". *J. Phys. Conf. Ser.* **276,** 012083. ISSN: 1742-6596 (Feb. 2011).

139. Madelung, O., Rössler, U. & Schulz, M. *Non-Tetrahedrally Bonded Binary Compounds II*. ISBN: 3-540-64966-2 (Springer-Verlag, Berlin/Heidelberg, 2000).

140. Shiang, J. J. "Application of radiative transport theory to light extraction from organic light emitting diodes". *J. Appl. Phys.* **95,** 2880–2888. ISSN: 00218979 (2004).

141. Yamasaki, T., Sumioka, K. & Tsutsui, T. "Organic light-emitting device with an ordered monolayer of silica microspheres as a scattering medium". *Appl. Phys. Lett.* **76,** 1243–1245. ISSN: 00036951 (2000).

142. An, S. J., Chae, J. H., Yi, G.-C. & Park, G. H. "Enhanced light output of GaN-based light-emitting diodes with ZnO nanorod arrays". *Appl. Phys. Lett.* **92,** 121108. ISSN: 00036951 (2008).

143. Kim, K.-K. *et al.* "Enhanced light extraction efficiency of GaN-based light-emitting diodes with ZnO nanorod arrays grown using aqueous solution". *Appl. Phys. Lett.* **94,** 071118. ISSN: 00036951 (2009).

144. Deul Ryu, B. *et al.* "Enhanced light output power of GaN-based light-emitting diodes by nano-rough indium tin oxide film using ZnO nanoparticles". *J. Appl. Phys.* **109,** 093116. ISSN: 00218979 (2011).

145. Gessmann, T., Schubert, E., Graff, J., Streubel, K. & Karnutsch, C. "Omnidirectional reflective contacts for light-emitting diodes". *IEEE Electron Device Lett.* **24,** 683–685. ISSN: 0741-3106 (Nov. 2003).

146. Lim, J.-H. *et al.* "UV Electroluminescence Emission from ZnO Light-Emitting Diodes Grown by High-Temperature Radiofrequency Sputtering". *Adv. Mater.* **18,** 2720–2724. ISSN: 09359648 (Oct. 2006).

147. Özgür, Ü. *et al.* "A comprehensive review of ZnO materials and devices". *J. Appl. Phys.* **98,** 041301. ISSN: 00218979 (2005).

148. Wang, Z. L. "Zinc oxide nanostructures: growth, properties and applications". *J. Phys. Condens. Matter* **16,** R829–R858. ISSN: 0953-8984 (June 2004).

149. Wang, N., Yang, Y. & Yang, G. "Great blue-shift of luminescence of ZnO nanoparticle array constructed from ZnO quantum dots." *Nanoscale Res. Lett.* **6,** 338. ISSN: 1556-276X (Jan. 2011).

150. Reeber, R. R. "Lattice parameters of ZnO from 4.2° to 296°K". *J. Appl. Phys.* **41,** 5063–5066. ISSN: 00218979 (1970).

151. Meyer, B. K. *et al.* "Bound exciton and donor–acceptor pair recombinations in ZnO". *Phys. Status Solidi* **241,** 231–260. ISSN: 0370-1972 (Feb. 2004).

152. Hümmer, K. "Interband Magnetoreflection of ZnO". *Phys. Status Solidi* **56,** 249–260. ISSN: 03701972 (Mar. 1973).

153. Look, D. *et al.* "Electrical properties of bulk ZnO". *Solid State Commun.* **105,** 399–401. ISSN: 00381098 (Feb. 1998).

154. Hammer, M. S., Rauh, D., Lorrmann, V., Deibel, C. & Dyakonov, V. "Effect of doping and field-induced charge carrier density on the electron transport in nanocrystalline ZnO". *Nanotechnology* **19,** 485701. ISSN: 0957-4484 (Dec. 2008).

155. Qian, L., Zheng, Y., Xue, J. & Holloway, P. H. "Stable and efficient quantum-dot light-emitting diodes based on solution-processed multilayer structures". *Nat. Photonics* **5,** 543–548. ISSN: 1749-4885 (Aug. 2011).

156. Roest, A., Kelly, J., Vanmaekelbergh, D. & Meulenkamp, E. "Staircase in the Electron Mobility of a ZnO Quantum Dot Assembly due to Shell Filling". *Phys. Rev. Lett.* **89,** 036801. ISSN: 0031-9007 (June 2002).

157. Eom, S.-H. *et al.* "Effect of electron injection and transport materials on efficiency of deep-blue phosphorescent organic light-emitting devices". *Org. Electron.* **10,** 686–691. ISSN: 15661199 (July 2009).

158. Sessolo, M., Bolink, H. J., Brine, H., Prima-Garcia, H. & Tena-Zaera, R. "Zinc oxide nanocrystals as electron injecting building blocks for plastic light sources". *J. Mater. Chem.* **22,** 4916–4920. ISSN: 0959-9428 (2012).

159. Kim, Y.-S. & Park, C. "Rich Variety of Defects in ZnO via an Attractive Interaction between O Vacancies and Zn Interstitials: Origin of n-Type Doping". *Phys. Rev. Lett.* **102,** 086403. ISSN: 0031-9007 (Feb. 2009).

160. Look, D., Hemsky, J. & Sizelove, J. "Residual Native Shallow Donor in ZnO". *Phys. Rev. Lett.* **82,** 2552–2555. ISSN: 0031-9007 (Mar. 1999).

161. Look, D. *et al.* "Evidence for Native-Defect Donors in n-Type ZnO". *Phys. Rev. Lett.* **95,** 225502. ISSN: 0031-9007 (Nov. 2005).

162. Halliburton, L. E. *et al.* "Production of native donors in ZnO by annealing at high temperature in Zn vapor". *Appl. Phys. Lett.* **87,** 172108. ISSN: 00036951 (2005).

163. Van de Walle, C. G. "Hydrogen as a Cause of Doping in Zinc Oxide". *Phys. Rev. Lett.* **85,** 1012–1015. ISSN: 0031-9007 (July 2000).

164. Chen, Z. Q. *et al.* "Postgrowth annealing of defects in ZnO studied by positron annihilation, x-ray diffraction, Rutherford backscattering, cathodoluminescence, and Hall measurements". *J. Appl. Phys.* **94,** 4807–4812. ISSN: 00218979 (2003).

165. Yan, J.-T., Chen, C.-H., Yen, S.-F. & Lee, C.-T. "Ultraviolet ZnO Nanorod/P-GaN-Heterostructured Light-Emitting Diodes". *IEEE Photonics Technol. Lett.* **22,** 146–148. ISSN: 1041-1135 (Feb. 2010).

166. Zhang, S., Wei, S.-H. & Zunger, A. "Intrinsic n-type versus p-type doping asymmetry and the defect physics of ZnO". *Phys. Rev. B* **63,** 075205. ISSN: 0163-1829 (Jan. 2001).

167. Lyons, J. L., Janotti, A. & Van de Walle, C. G. "Why nitrogen cannot lead to p-type conductivity in ZnO". *Appl. Phys. Lett.* **95,** 252105. ISSN: 00036951 (2009).

168. Lin, S. *et al.* "p-type behavior in Na-doped ZnO films and ZnO homojunction light-emitting diodes". *Solid State Commun.* **148,** 25–28. ISSN: 00381098 (Oct. 2008).

169. Park, T.-Y. *et al.* "Electroluminescence emission from light-emitting diode of p-ZnO/(InGaN/GaN) multiquantum well/n-GaN". *Appl. Phys. Lett.* **98,** 251111. ISSN: 00036951 (2011).

170. Du, G.-T. *et al.* "Electrically pumped lasing from p-ZnO/n-GaN heterojunction diodes". *Appl. Phys. Lett.* **101,** 053503. ISSN: 00036951 (2012).

171. Sun, J. C. *et al.* "Realization of ultraviolet electroluminescence from ZnO homojunction with n-ZnO/p-ZnO:As/GaAs structure". *Appl. Phys. Lett.* **90,** 121128. ISSN: 00036951 (2007).

172. Xu, W. Z. *et al.* "ZnO light-emitting diode grown by plasma-assisted metal organic chemical vapor deposition". *Appl. Phys. Lett.* **88,** 173506. ISSN: 00036951 (2006).

173. Djurisić, A. B. & Leung, Y. H. "Optical properties of ZnO nanostructures." *Small* **2,** 944–961. ISSN: 1613-6829 (Aug. 2006).

174. Schneider, L., Zaitsev, S. V., Bacher, G., Jin, W. & Winterer, M. "Recombination dynamics in ZnO nanoparticles produced by chemical vapor synthesis". *J. Appl. Phys.* **102,** 023524. ISSN: 00218979 (2007).

175. Fonoberov, V., Alim, K., Balandin, A., Xiu, F. & Liu, J. "Photoluminescence investigation of the carrier recombination processes in ZnO quantum dots and nanocrystals". *Phys. Rev. B* **73,** 1–9. ISSN: 1098-0121 (Apr. 2006).

176. Fallert, J. *et al.* "Surface-state related luminescence in ZnO nanocrystals". *J. Appl. Phys.* **101,** 073506. ISSN: 00218979 (2007).

177. Bekeny, C. *et al.* "Influence of ZnO seed crystals and annealing on the optical quality of low-temperature grown ZnO nanorods". *J. Appl. Phys.* **102,** 044908. ISSN: 00218979 (2007).

178. Djurišić, A. B. *et al.* "Defect emissions in ZnO nanostructures". *Nanotechnology* **18,** 095702. ISSN: 0957-4484 (Mar. 2007).

179. Wischmeier, L., Voss, T., Rückmann, I. & Gutowski, J. "Correlations between surface-excitonic emission bands in ZnO nanowires." *Nanotechnology* **19,** 135705. ISSN: 1361-6528 (Apr. 2008).

180. Djurišić, A., Ng, A. & Chen, X. "ZnO nanostructures for optoelectronics: Material properties and device applications". *Prog. Quantum Electron.* **34,** 191–259. ISSN: 00796727 (July 2010).

181. Wagner, M. R. *et al.* "Bound excitons in ZnO: Structural defect complexes versus shallow impurity centers". *Phys. Rev. B* **84,** 035313. ISSN: 1098-0121 (July 2011).

182. Yin, M. *et al.* "Zinc oxide quantum rods." *J. Am. Chem. Soc.* **126,** 6206–6207. ISSN: 0002-7863 (May 2004).

183. Haranath, D., Sahai, S., Joshi, A. G., Gupta, B. K. & Shanker, V. "Investigation of confinement effects in ZnO quantum dots." *Nanotechnology* **20,** 425701. ISSN: 1361-6528 (Oct. 2009).

184. Sharma, A., Singh, B., Dhar, S., Gondorf, A. & Spasova, M. "Effect of surface groups on the luminescence property of ZnO nanoparticles synthesized by sol–gel route". *Surf. Sci.* **606,** L13–L17. ISSN: 00396028 (Feb. 2012).

185. Xie, R., Battaglia, D. & Peng, X. "Colloidal InP nanocrystals as efficient emitters covering blue to near-infrared." *J. Am. Chem. Soc.* **129,** 15432–15433. ISSN: 1520-5126 (Dec. 2007).

186. Mangolini, L., Jurbergs, D., Rogojina, E. & Kortshagen, U. "High efficiency photoluminescence from silicon nanocrystals prepared by plasma synthesis and organic surface passivation". *Phys. status solidi* **3,** 3975–3978. ISSN: 16101634 (Dec. 2006).

187. Mastronardi, M. L. *et al.* "Size-dependent absolute quantum yields for size-separated colloidally-stable silicon nanocrystals." *Nano Lett.* **12,** 337–342. ISSN: 1530-6992 (Jan. 2012).

188. Stroyuk, O. L., Dzhagan, V. M., Shvalagin, V. V. & Kuchmiy, S. Y. "Size-Dependent Optical Properties of Colloidal ZnO Nanoparticles Charged by Photoexcitation". *J. Phys. Chem. C* **114,** 220–225. ISSN: 1932-7447 (Jan. 2010).

189. Zhang, L. *et al.* "Origin of Visible Photoluminescence of ZnO Quantum Dots: Defect-Dependent and Size-Dependent". *J. Phys. Chem. C* **114,** 9651–9658. ISSN: 1932-7447 (June 2010).

190. Jacobsson, T. J. & Edvinsson, T. "Absorption and fluorescence spectroscopy of growing ZnO quantum dots: size and band gap correlation and evidence of mobile trap states." *Inorg. Chem.* **50,** 9578–9586. ISSN: 1520-510X (Oct. 2011).

191. Yamamoto, S. "Photoenhanced Band-Edge Luminescence in ZnO Nanocrystals Dispersed in Ethanol". *J. Phys. Chem. C* **115,** 21635–21640. ISSN: 1932-7447 (Nov. 2011).

192. Lin, K.-F., Cheng, H.-M., Hsu, H.-C., Lin, L.-J. & Hsieh, W.-F. "Band gap variation of size-controlled ZnO quantum dots synthesized by sol–gel method". *Chem. Phys. Lett.* **409,** 208–211. ISSN: 00092614 (June 2005).

193. Sakai, Y., Lee, C.-G., Uehara, M., Nakamura, H. & Maeda, H. "The preparation and property control of Zinc Oxide NPs". *IOP Conf. Ser. Mater. Sci. Eng.* **18,** 082026. ISSN: 1757-899X (Oct. 2011).

194. Norberg, N. S. & Gamelin, D. R. "Influence of surface modification on the luminescence of colloidal ZnO nanocrystals." *J. Phys. Chem. B* **109,** 20810–20816. ISSN: 1520-6106 (Nov. 2005).

195. Zhou, H. *et al.* "Behind the weak excitonic emission of ZnO quantum dots: ZnO/Zn(OH)2 core-shell structure". *Appl. Phys. Lett.* **80,** 210–212. ISSN: 00036951 (2002).

196. Janotti, A. & Van de Walle, C. G. "Native point defects in ZnO". *Phys. Rev. B* **76,** 165202. ISSN: 1098-0121 (Oct. 2007).

197. Kurbanov, S., Panin, G., Kim, T. W. & Kang, T. W. "Thermo- and Photoannealing of ZnO Nanocrystals". *Jpn. J. Appl. Phys.* **46,** 4172–4174. ISSN: 0021-4922 (July 2007).

198. Irimpan, L., Nampoori, V. P. N., Radhakrishnan, P., Deepthy, A. & Krishnan, B. "Size dependent fluorescence spectroscopy of nanocolloids of ZnO". *J. Appl. Phys.* **102,** 063524. ISSN: 00218979 (2007).

199. Zeng, H. *et al.* "Blue Luminescence of ZnO Nanoparticles Based on Non-Equilibrium Processes: Defect Origins and Emission Controls". *Adv. Funct. Mater.* **20,** 561–572. ISSN: 1616301X (Feb. 2010).

200. Cao, B., Cai, W. & Zeng, H. "Temperature-dependent shifts of three emission bands for ZnO nanoneedle arrays". *Appl. Phys. Lett.* **88,** 161101. ISSN: 00036951 (2006).

201. Kumar, B., Gong, H., Vicknesh, S., Chua, S. J. & Tripathy, S. "Luminescence properties of ZnO layers grown on Si-on-insulator substrates". *Appl. Phys. Lett.* **89,** 141901. ISSN: 00036951 (2006).

202. Zhang, D. H., Xue, Z. Y. & Wang, Q. P. "The mechanisms of blue emission from ZnO films deposited on glass substrate by r.f. magnetron sputtering". *J. Phys. D. Appl. Phys.* **35,** 2837–2840. ISSN: 0022-3727 (Nov. 2002).

203. Ahn, C. H., Kim, Y. Y., Kim, D. C., Mohanta, S. K. & Cho, H. K. "A comparative analysis of deep level emission in ZnO layers deposited by various methods". *J. Appl. Phys.* **105,** 013502. ISSN: 00218979 (2009).

204. Vlasenko, L. & Watkins, G. "Optical detection of electron paramagnetic resonance for intrinsic defects produced in ZnO by 2.5-MeV electron irradiation in situ at 4.2 K". *Phys. Rev. B* **72,** 035203. ISSN: 1098-0121 (July 2005).

205. Hagura, N., Ogi, T., Shirahama, T., Iskandar, F. & Okuyama, K. "Highly luminescent silica-coated ZnO nanoparticles dispersed in an aqueous medium". *J. Lumin.* **131,** 921–925. ISSN: 00222313 (May 2011).

206. Matsuyama, K. *et al.* "Bioimaging application of highly luminescent silica-coated ZnO-nanoparticle quantum dots with biotin." *J. Colloid Interface Sci.* **399,** 19–25. ISSN: 1095-7103 (June 2013).

207. Sarkar, A., Chakrabarti, M., Ray, S. K., Bhowmick, D. & Sanyal, D. "Positron annihilation lifetime and photoluminescence studies on single crystalline ZnO." *J. Phys. Condens. Matter* **23,** 155801. ISSN: 1361-648X (Apr. 2011).

208. Van Dijken, A., Makkinje, J. & Meijerink, A. "The influence of particle size on the luminescence quantum efficiency of nanocrystalline ZnO particles". *J. Lumin.* **92,** 323–328. ISSN: 00222313 (Apr. 2001).

209. Ghosh, M. & Raychaudhuri, A. K. "Shape transition in ZnO nanostructures and its effect on blue-green photoluminescence." *Nanotechnology* **19,** 445704. ISSN: 0957-4484 (Nov. 2008).

210. Gruzintsev, A. N. & Yakimov, E. E. "Annealing Effect on the Luminescent Properties and Native Defects of ZnO". *Inorg. Mater.* **41,** 725–729. ISSN: 0020-1685 (July 2005).

211. Van Dijken, A., Meulenkamp, E. A., Vanmaekelbergh, D. & Meijerink, A. "Identification of the transition responsible for the visible emission in ZnO using quantum size effects". *J. Lumin.* **90,** 123–128 (2000).

212. Van Dijken, A., Meulenkamp, E. A., Vanmaekelbergh, D. & Meijerink, A. "The Kinetics of the Radiative and Nonradiative Processes in Nanocrystalline ZnO Particles upon Photoexcitation". *J. Phys. Chem. B* **104,** 1715–1723. ISSN: 1520-6106 (Mar. 2000).

213. Van Dijken, A., Meulenkamp, E. A., Vanmaekelbergh, D. & Meijerink, A. "Influence of Adsorbed Oxygen on the Emission Properties of Nanocrystalline ZnO Particles". *J. Phys. Chem. B* **104,** 4355–4360. ISSN: 1520-6106 (May 2000).

214. Bohle, D. S. & Spina, C. J. "Cationic and anionic surface binding sites on nanocrystalline zinc oxide: surface influence on photoluminescence and photocatalysis." *J. Am. Chem. Soc.* **131,** 4397–4404. ISSN: 1520-5126 (Apr. 2009).

215. Jana, N. R., Yu, H.-H., Ali, E. M., Zheng, Y. & Ying, J. Y. "Controlled photostability of luminescent nanocrystalline ZnO solution for selective detection of aldehydes". *Chem. Commun.* 1406–1408. ISSN: 1359-7345 (2007).

216. Moussodia, R.-O., Balan, L., Merlin, C., Mustin, C. & Schneider, R. "Biocompatible and stable ZnO quantum dots generated by functionalization with siloxane-core PAMAM dendrons". *J. Mater. Chem.* **20,** 1147–1155. ISSN: 0959-9428 (2010).

217. Cohn, A. W., Janßen, N., Mayer, J. M. & Gamelin, D. R. "Photocharging ZnO Nanocrystals: Picosecond Hole Capture, Electron Accumulation, and Auger Recombination". *J. Phys. Chem. C* **116,** 20633–20642. ISSN: 1932-7447 (Sept. 2012).

218. Guo, B., Qiu, Z. R. & Wong, K. S. "Intensity dependence and transient dynamics of donor–acceptor pair recombination in ZnO thin films grown on (001) silicon". *Appl. Phys. Lett.* **82,** 2290–2292. ISSN: 00036951 (2003).

219. Studenikin, S. A. & Cocivera, M. "Time-resolved luminescence and photoconductivity of polycrystalline ZnO films". *J. Appl. Phys.* **91,** 5060–5065. ISSN: 00218979 (2002).

220. Lin, B., Fu, Z. & Jia, Y. "Green luminescent center in undoped zinc oxide films deposited on silicon substrates". *Appl. Phys. Lett.* **79,** 943–945. ISSN: 00036951 (2001).

221. Wu, X. L., Siu, G. G., Fu, C. L. & Ong, H. C. "Photoluminescence and cathodoluminescence studies of stoichiometric and oxygen-deficient ZnO films". *Appl. Phys. Lett.* **78,** 2285–2287. ISSN: 00036951 (2001).

222. Liu, M., Kitai, A. H. & Mascher, P. "Point defects and luminescence centres in zinc oxide and zinc oxide doped with manganese". *J. Lumin.* **54,** 35–42. ISSN: 00222313 (Aug. 1992).

223. Tam, K. H. *et al.* "Defects in ZnO nanorods prepared by a hydrothermal method." *J. Phys. Chem. B* **110,** 20865–20871. ISSN: 1520-6106 (Oct. 2006).

224. Xi, Y. Y. *et al.* "NiO/ZnO light emitting diodes by solution-based growth". *Appl. Phys. Lett.* **92,** 113505. ISSN: 00036951 (2008).

225. Liu, X. "Growth mechanism and properties of ZnO nanorods synthesized by plasma-enhanced chemical vapor deposition". *J. Appl. Phys.* **95,** 3141–3147. ISSN: 00218979 (2004).

226. Ling, B. *et al.* "Electroluminescence From Ferromagnetic Fe-Doped ZnO Nanorod Arrays on p-Si". *IEEE Trans. Electron Devices* **57,** 1948–1952. ISSN: 0018-9383 (Aug. 2010).

227. Greene, L. E. *et al.* "Low-temperature wafer-scale production of ZnO nanowire arrays." *Angew. Chem. Int. Ed. Engl.* **42,** 3031–3034. ISSN: 1433-7851 (July 2003).

228. Xu, P., Sun, Y., Shi, C., Xu, F. & Pan, H. "The electronic structure and spectral properties of ZnO and its defects". *Nucl. Instruments Methods Phys. Res. Sect. B Beam Interact. with Mater. Atoms* **199,** 286–290. ISSN: 0168583X (Jan. 2003).

229. Gomi, M., Oohira, N., Ozaki, K. & Koyano, M. "Photoluminescent and Structural Properties of Precipitated ZnO Fine Particles". *Jpn. J. Appl. Phys.* **42,** 481–485. ISSN: 0021-4922 (Feb. 2003).

230. Ohring, M. *Materials Science of Thin Films* Second Edi. ISBN: 978-0-12-524975-1 (Academic Press, San Diego, London, 2001).

231. Asha, A. S. *RF magnetron sputtered perovskite oxide electrodes for Ferroelectric RAM*. PhD thesis (Cochin University of Technology and Science, 2007).

232. Treharne, R. E. *RF Magnetron Sputtering of Transparent Conducting Oxides and CdTe / CdS Solar Cells*. PhD thesis (Durham University, 2011).

233. Köster, R. *Croissance auto-assemblée de fils de GaN sans catalyseur par épitaxie en phase vapeur d'organo-métalliques*. PhD thesis (Université de Grenoble, 2010).

234. Neshataeva, E., Kümmell, T., Bacher, G. & Ebbers, A. "All-inorganic light emitting device based on ZnO nanoparticles". *Appl. Phys. Lett.* **94,** 091115. ISSN: 00036951 (2009).

235. Neshataeva, E., Kuemmell, T., Ebbers, A. & Bacher, G. *Zinc Oxide Materials and Devices IV*. in *Proc. SPIE* (eds Teherani, F. H., Litton, C. W. & Rogers, D. J.) **7217** (Feb. 2009), 721707.

236. Baik, D. G. & Cho, S. M. "Application of sol-gel derived films for ZnO / n-Si junction solar cells". **354,** 227–231 (1999).

237. Pethuraja, G. G. "Current-Voltage Characteristics of ITO/p-Si and ITO/n-Si Contact Interfaces". *Adv. Mater. Phys. Chem.* **02,** 59–62. ISSN: 2162-531X (2012).

238. Neshataeva, E., Kümmell, T., Ebbers, A. & Bacher, G. "Electrically driven ZnO nanoparticle light emitting device". *Electron. Lett.* **44,** 1485–1487. ISSN: 00135194 (2008).

239. Liang, S. *et al.* "ZnO Schottky ultraviolet photodetectors". *J. Cryst. Growth* **225,** 110–113. ISSN: 00220248 (May 2001).

240. Kim, H.-K. & Lee, J.-M. "Low resistance nonalloyed Al-based ohmic contacts on n-ZnO:Al". *Superlattices Microstruct.* **42,** 255–258. ISSN: 07496036 (July 2007).

241. Sheng, H., Emanetoglu, N. W., Muthukumar, S., Feng, S. & Lu, Y. "Nonalloyed Al ohmic contacts to Mg(x)Zn(1-x)O". *J. Electron. Mater.* **31,** 811–814. ISSN: 0361-5235 (July 2002).

242. Meyer, J. *et al.* "Charge generation layers comprising transition metal-oxide/organic interfaces: Electronic structure and charge generation mechanism". *Appl. Phys. Lett.* **96,** 193302. ISSN: 00036951 (2010).

243. Greiner, M. T. *et al.* "Universal energy-level alignment of molecules on metal oxides." *Nat. Mater.* **11,** 76–81. ISSN: 1476-1122 (Jan. 2012).

244. Vida, G., Josepovits, V. K., Gyor, M. & Deák, P. "Characterization of tungsten surfaces by simultaneous work function and secondary electron emission measurements." *Microsc. Microanal.* **9,** 337–342. ISSN: 1431-9276 (Aug. 2003).

245. Höfle, S. *et al.* "Tungsten oxide buffer layers fabricated in an inert sol-gel process at room-temperature for blue organic light-emitting diodes." *Adv. Mater.* **25,** 4113–4116. ISSN: 1521-4095 (Aug. 2013).

246. Rout, C. S., Govindaraj, A. & Rao, C. N. R. "High-sensitivity hydrocarbon sensors based on tungsten oxide nanowires". *J. Mater. Chem.* **16,** 3936–3941. ISSN: 0959-9428 (2006).

247. Meyer, J. *et al.* "Highly efficient simplified organic light emitting diodes". *Appl. Phys. Lett.* **91,** 113506. ISSN: 00036951 (2007).

248. Li, J., Yahiro, M., Ishida, K., Yamada, H. & Matsushige, K. "Enhanced performance of organic light emitting device by insertion of conducting/insulating WO3 anodic buffer layer". *Synth. Met.* **151,** 141–146. ISSN: 03796779 (June 2005).

249. Hamwi, S. *et al.* "The Role of Transition Metal Oxides in Charge-Generation Layers for Stacked Organic Light-Emitting Diodes". *Adv. Funct. Mater.* **20,** 1762–1766. ISSN: 1616301X (June 2010).

250. Meyer, J. *et al.* "Transparent Inverted Organic Light-Emitting Diodes with a Tungsten Oxide Buffer Layer". *Adv. Mater.* **20,** 3839–3843. ISSN: 09359648 (Oct. 2008).

251. Meyer, J. *et al.* "Transition metal oxides for organic electronics: energetics, device physics and applications." *Adv. Mater.* **24,** 5408–5427. ISSN: 1521-4095 (Oct. 2012).

252. Neghabi, M., Behjat, A., Fatemeh Mirjalili, B. B. & Zamani, L. "Improvement of performance of tetraphenylporphyrin-based red organic light emitting diodes using WO3 and C60 buffer layers". *Curr. Appl. Phys.* **13,** 302–306. ISSN: 15671739 (Jan. 2013).

253. Mansingh, A., Sayer, M. & Webb, J. "Electrical conduction in amorphous WO3 films". *J. Non. Cryst. Solids* **28,** 123–137. ISSN: 00223093 (Apr. 1978).

254. Li, Y., Zhang, S., Sritharan, T., Liu, Y. & Chen, T. "Influence of oxygen partial pressure on magnetron sputtered Sr0.8Nd0.3Bi2.5Ta2O9+x ferroelectric thin films". *J. Alloys Compd.* **457,** 549–554. ISSN: 09258388 (June 2008).

255. Leja, E., Kołodziej, A., Pisarkiewicz, T. & Stapiński, T. "The dynamics of reactive ion sputtering of Sn-Sb and In-Sn alloys in an Ar-O2 atmosphere". *Thin Solid Films* **76,** 283–287. ISSN: 00406090 (Feb. 1981).

256. *Inorganic Crystal Structure Database.* FIZ Karlsruhe. <`http://fiz-karlsruhe.de/icsd.html?&L=1`> (2011).

257. Lassner, E. & Schubert, W.-D. *Tungsten.* ISBN: 978-1-4613-7225-7 (Springer US, Boston, MA, 1999).

258. Patterson, A. "The Scherrer Formula for X-Ray Particle Size Determination". *Phys. Rev.* **56,** 978–982. ISSN: 0031-899X (Nov. 1939).

259. Sayerst, D. E., Sterntf, E. A. & Lytle, F. "New Technique for Investigating Noncrystalline Structures: Fourier Analysis of the Extended X-Ray - Absorption Fine Structure". *Phys. Rev. Lett.* **2,** 1204–1207 (1971).

260. Mortimer, R. J. "Electrochromic Materials". *Annu. Rev. Mater. Res.* **41,** 241–268. ISSN: 1531-7331 (Aug. 2011).

261. Demiryont, H. & Nietering, K. E. "Tungsten oxide films by reactive and conventional evaporation techniques." *Appl. Opt.* **28,** 1494–1500. ISSN: 0003-6935 (Apr. 1989).

262. Bamwenda, G. R. & Arakawa, H. "The visible light induced photocatalytic activity of tungsten trioxide powders". *Appl. Catal. A Gen.* **210,** 181–191. ISSN: 0926860X (Mar. 2001).

263. Sun, Q. *et al.* "Appearance of bulk properties in small tungsten oxide clusters." *J. Chem. Phys.* **121,** 9417–9422. ISSN: 0021-9606 (Dec. 2004).

264. Patel, K., Panchal, C., Kheraj, V. & Desai, M. "Growth, structural, electrical and optical properties of the thermally evaporated tungsten trioxide (WO3) thin films". *Mater. Chem. Phys.* **114,** 475–478. ISSN: 02540584 (Mar. 2009).

265. Hutchins, M., Abu-Alkhair, O., El-Nahass, M. & El-Hady, K. A. "Structural and optical characterisation of thermally evaporated tungsten trioxide (WO3) thin films". *Mater. Chem. Phys.* **98,** 401–405. ISSN: 02540584 (Aug. 2006).

266. Gullapalli, S. K., Vemuri, R. S. & Ramana, C. V. "Structural transformation induced changes in the optical properties of nanocrystalline tungsten oxide thin films". *Appl. Phys. Lett.* **96,** 171903. ISSN: 00036951 (2010).

267. Kumar, V. B. & Mohanta, D. "Formation of nanoscale tungsten oxide structures and colouration characteristics". *Bull. Mater. Sci.* **34,** 435–442. ISSN: 0250-4707 (Sept. 2011).

268. Tauc, J. *Amorphous and Liquid Semiconductors,* 159–220. ISBN: 978-1-4615-8707-1 (Springer US, Boston, MA, 1974).

269. Cole, B. *et al.* "Evaluation of Nitrogen Doping of Tungsten Oxide for Photoelectrochemical Water Splitting". *J. Phys. Chem. C* **112,** 5213–5220. ISSN: 1932-7447 (Apr. 2008).

270. Paluselli, D., Marsen, B., Miller, E. L. & Rocheleau, R. E. "Nitrogen Doping of Reactively Sputtered Tungsten Oxide Films". *Electrochem. Solid-State Lett.* **8,** G301–G303. ISSN: 10990062 (2005).

271. Sun, X. L. & Cao, H. T. "Effects of Nitrogen Doping on Optical Properties of Tungsten Oxide Thin Films". *Adv. Mater. Res.* **616-618,** 1773–1777. ISSN: 1662-8985 (Dec. 2012).

272. Mashford, B. S., Nguyen, T.-L., Wilson, G. J. & Mulvaney, P. "All-inorganic quantum-dot light-emitting devices formed via low-cost, wet-chemical processing". *J. Mater. Chem.* **20,** 167–172. ISSN: 0959-9428 (2010).

273. Deng, R. *et al.* "X-ray photoelectron spectroscopy measurement of n-ZnO/p-NiO heterostructure valence-band offset". *Appl. Phys. Lett.* **94,** 022108. ISSN: 00036951 (2009).

274. Yang, Z.-G. *et al.* "Valence-band offset of p-NiO/n-ZnO heterojunction measured by X-ray photoelectron spectroscopy". *Phys. Lett. A* **375,** 1760–1763. ISSN: 03759601 (Apr. 2011).

275. Zhang, L. *et al.* "Electroluminescence from n-ZnO : Ga/p-GaN heterojunction light-emitting diodes with different interfacial layers". *J. Phys. D. Appl. Phys.* **45,** 485103. ISSN: 0022-3727 (Dec. 2012).

276. Wang, T. *et al.* "Nonpolar light emitting diodes of m-plane ZnO on c-plane GaN with the Al2O3 interlayer". *Appl. Phys. Lett.* **102,** 141912. ISSN: 00036951 (2013).

277. Liu, Y. *et al.* "Introducing Ga2O3 thin films as novel electron blocking layer to ZnO/p-GaN heterojunction LED". *Appl. Phys. B* **109,** 605–609. ISSN: 0946-2171 (Sept. 2012).

278. Chen, X. *et al.* "GaN/MgO/ZnO heterojunction light-emitting diodes". *Thin Solid Films* **527,** 303–307. ISSN: 00406090 (Jan. 2013).

279. Zhu, G. Y. *et al.* "Ultraviolet electroluminescence from n-ZnO/i-MgO/p+-GaN heterojunction light-emitting diodes fabricated by RF-magnetron sputtering". *Appl. Phys. B* **109,** 195–199. ISSN: 0946-2171 (Sept. 2012).

280. Zhu, H. *et al.* "Ultralow-Threshold Laser Realized in Zinc Oxide". *Adv. Mater.* **21,** 1613–1617. ISSN: 09359648 (Apr. 2009).

281. Qiao, Q. *et al.* "Localized surface plasmon enhanced light-emitting devices". *J. Mater. Chem.* **22,** 9481–9484. ISSN: 0959-9428 (2012).

282. Guo, Z. *et al.* "The ultralow driven current ultraviolet-blue light-emitting diode based on n-ZnO nanowires/i-polymer/p-GaN heterojunction". *Appl. Phys. Lett.* **97,** 173508. ISSN: 00036951 (2010).

283. Wu, M. *et al.* "Ultraviolet Electroluminescence From n-ZnO-SiO2-ZnO Nanocomposite/p-GaN Heterojunction Light-Emitting Diodes at Forward and Reverse Bias". *IEEE Photonics Technol. Lett.* **20,** 1772–1774. ISSN: 1041-1135 (Nov. 2008).

284. Chen, C. P. *et al.* "Observation of 394 nm electroluminescence from low-temperature sputtered n-ZnO/SiO2 thin films on top of the p-GaN heterostructure". *Appl. Phys. Lett.* **91,** 091107. ISSN: 00036951 (2007).

285. Dong, J. J. *et al.* "Ultraviolet electroluminescence from ordered ZnO nanorod array/p-GaN light emitting diodes". *Appl. Phys. Lett.* **100,** 171109. ISSN: 00036951 (2012).

286. Demtröder, W. *Experimentalphysik 3* Third Edit. ISBN: 978-3-642-03910-2 (Springer Berlin Heidelberg, Berlin, Heidelberg, 2005).

287. Bass, M. *Handbook of Optics Volume IV* Third Edit. ISBN: 978-0071498890 (McGraw Hill Book Co., 2009).

288. Dai, J., Xu, C. X. & Sun, X. W. "ZnO-microrod/p-GaN heterostructured whispering-gallery-mode microlaser diodes." *Adv. Mater.* **23,** 4115–4119. ISSN: 1521-4095 (Oct. 2011).

289. Monticone, S. & Tufeu, R. "Complex Nature of the UV and Visible Fluorescence of Colloidal ZnO Nanoparticles". *J. Phys. Chem. B* **102,** 2854–2862. ISSN: 1520-6106 (Apr. 1998).

290. Felbier, P. *et al.* "Highly Luminescent ZnO Quantum Dots Made in a Nonthermal Plasma". *Adv. Funct. Mater.* **24,** 1988–1993. ISSN: 1616301X (Apr. 2014).

291. Kruis, F., Fissan, H. & Peled, A. "Synthesis of nanoparticles in the gas phase for electronic, optical and magnetic applications—a review". *J. Aerosol Sci.* **29,** 511–535. ISSN: 00218502 (June 1998).

292. Mangolini, L., Thimsen, E. & Kortshagen, U. "High-yield plasma synthesis of luminescent silicon nanocrystals." *Nano Lett.* **5,** 655–659. ISSN: 1530-6984 (Apr. 2005).

293. Anthony, R. J., Cheng, K.-Y., Holman, Z. C., Holmes, R. J. & Kortshagen, U. R. "An all-gas-phase approach for the fabrication of silicon nanocrystal light-emitting devices." *Nano Lett.* **12,** 2822–2825. ISSN: 1530-6992 (June 2012).

294. Bapat, A. *et al.* "Plasma synthesis of single-crystal silicon nanoparticles for novel electronic device applications". *Plasma Phys. Control. Fusion* **46,** B97–B109. ISSN: 0741-3335 (Dec. 2004).

295. Jurbergs, D., Rogojina, E., Mangolini, L. & Kortshagen, U. "Silicon nanocrystals with ensemble quantum yields exceeding 60%". *Appl. Phys. Lett.* **88,** 233116. ISSN: 00036951 (2006).

296. Anthony, R. & Kortshagen, U. "Photoluminescence quantum yields of amorphous and crystalline silicon nanoparticles". *Phys. Rev. B* **80,** 115407. ISSN: 1098-0121 (Sept. 2009).

297. Anthony, R. J., Rowe, D. J., Stein, M., Yang, J. & Kortshagen, U. "Routes to Achieving High Quantum Yield Luminescence from Gas-Phase-Produced Silicon Nanocrystals". *Adv. Funct. Mater.* **21,** 4042–4046. ISSN: 1616301X (Nov. 2011).

298. Wheeler, L. M., Levij, L. M. & Kortshagen, U. R. "Tunable Band Gap Emission and Surface Passivation of Germanium Nanocrystals Synthesized in the Gas Phase". *J. Phys. Chem. Lett.* **4,** 3392–3396. ISSN: 1948-7185 (Oct. 2013).

299. Gresback, R., Hue, R., Gladfelter, W. L. & Kortshagen, U. R. "Combined plasma gas-phase synthesis and colloidal processing of InP/ZnS core/shell nanocrystals." *Nanoscale Res. Lett.* **6,** 68. ISSN: 1556-276X (Jan. 2011).

300. Senger, R. & Bajaj, K. "Optical properties of confined polaronic excitons in spherical ionic quantum dots". *Phys. Rev. B* **68,** 045313. ISSN: 0163-1829 (July 2003).

301. Wong, E. M. & Searson, P. C. "ZnO quantum particle thin films fabricated by electrophoretic deposition". *Appl. Phys. Lett.* **74,** 2939–2941. ISSN: 00036951 (1999).

302. Porras-Montenegro, N., Pérez-Merchancano, S. T. & Latgé, A. "Binding energies and density of impurity states in spherical GaAs-(Ga,Al)As quantum dots". *J. Appl. Phys.* **74,** 7624–7626. ISSN: 00218979 (1993).

303. Zhu, J.-L. & Chen, X. "Spectrum and binding of an off-center donor in a spherical quantum dot". *Phys. Rev. B* **50,** 4497–4502. ISSN: 0163-1829 (Aug. 1994).

304. Omata, T. *et al.* "UV luminescent organic-capped ZnO quantum dots synthesized by alkoxide hydrolysis with dilute water." *J. Colloid Interface Sci.* **355,** 274–281. ISSN: 1095-7103 (Mar. 2011).

305. Kiliani, G. *et al.* "Ultraviolet photoluminescence of ZnO quantum dots sputtered at room-temperature." *Opt. Express* **19,** 1641–1647. ISSN: 1094-4087 (Jan. 2011).

306. Djurišić, A. B. *et al.* "Green, yellow, and orange defect emission from ZnO nanostructures: Influence of excitation wavelength". *Appl. Phys. Lett.* **88,** 103107. ISSN: 00036951 (2006).

307. Djurišić, A. B. *et al.* "Photoluminescence and Electron Paramagnetic Resonance of ZnO Tetrapod Structures". *Adv. Funct. Mater.* **14,** 856–864. ISSN: 1616-301X (Sept. 2004).

308. Liu, J. *et al.* "Quantifying oxygen diffusion in ZnO nanobelt". *Appl. Phys. Lett.* **89,** 063125. ISSN: 00036951 (2006).

309. Subramanian, V., Wolf, E. E. & Kamat, P. V. "Green Emission to Probe Photoinduced Charging Events in ZnO-Au Nanoparticles. Charge Distribution and Fermi-Level Equilibration". *J. Phys. Chem. B* **107,** 7479–7485. ISSN: 1520-6106 (July 2003).

310. Wood, A., Giersig, M. & Mulvaney, P. "Fermi Level Equilibration in Quantum Dot-Metal Nanojunctions". *J. Phys. Chem. B* **105,** 8810–8815. ISSN: 1520-6106 (Sept. 2001).

311. Williams, A. T. R., Winfield, S. A. & Miller, J. N. "Relative fluorescence quantum yields using a computer-controlled luminescence spectrometer". *Analyst* **108,** 1067–1071. ISSN: 0003-2654 (1983).

312. Eaton, D. F. "Reference materials for fluorescence measurement". *Pure Appl. Chem.* **60,** 1107–1114. ISSN: 0033-4545 (1988).

313. Aralaguppi, M. I., Jadar, C. V. & Aminabhavi, T. M. "Density, Viscosity, Refractive Index, and Speed of Sound in Binary Mixtures of Acrylonitrile with Methanol, Ethanol, Propan-1-ol, Butan-1-ol, Pentan-1-ol, Hexan-1-ol, Heptan-1-ol, and Butan-2-ol". *J. Chem. Eng. Data* **44,** 216–221. ISSN: 0021-9568 (Mar. 1999).

314. Aminabhavi, T. M., Patil, V. B., Aralaguppi, M. I. & Phayde, H. T. S. "Density, Viscosity, and Refractive Index of the Binary Mixtures of Cyclohexane with Hexane, Heptane, Octane, Nonane, and Decane at (298.15, 303.15, and 308.15) K". *J. Chem. Eng. Data* **41,** 521–525. ISSN: 0021-9568 (Jan. 1996).

315. Vivien, L. & Pavesi, L. *Handbook of Silicon Photonics.* ISBN: 9781439836101 (Taylor & Francis, Boca Raton, FL, 2013).

List of publications

Peer-reviewed journal, associated with this thesis

- **P. Felbier**, J. Yang, J. Theis, R. W. Liptak, A. Wagner, A. Lorke, G. Bacher, and U. Kortshagen, "Highly luminescent ZnO quantum dots made in a non-thermal plasma". *Adv. Funct. Mater.*, **24**, 1988-1993. (Apr. 2014).

Peer-reviewed journal, not associated with this thesis

- J. Brandt, **P. Felbier**, D. Fröhlich, C. Sandfort, M. Bayer, and H. Stolz, "Temperature dependence of homogeneous broadening of the 1S paraexciton in Cu_2O". *Phys. Rev. B*, **81**, 155214. (Apr. 2010).

Selected conference contributions

- **P. Felbier**, J. Yang, J. Theis, A. Lorke, G. Bacher, and U. Kortshagen, "ZnO quantum dots for LED applications". *Gordon Research Conference on Nanomaterials for Applications in Energy Technology*, Ventura, USA (03.-08.02.13).

- **P. Felbier**, M. Schmitz, E. Nannen, T. Kümmell and G. Bacher, "Light emitting devices based on ZnO nanoparticles: hole injection". *Evonik Summerschool*, Marl (20.-22.07.2011).

- **P. Felbier**, S. Wolff, E. Neshataeva, T. Kümmell, and G. Bacher, "ZnO Nanoparticle LED on TCO substrates". *Chemtogether*, Essen (17.-19.11.2010).

- **P. Felbier**, E. Neshataeva, T. Kümmell, A. Ebbers and G. Bacher, "All-inorganic light emitting devices based on ZnO nanoparticles". *MRS Spring Meeting*, San Francisco (05.-09.04.2010).